McKelvey School of Engineering Theses & Dissertations

McKelvey School of Engineering

Summer 8-15-2017

Fundamental Studies Of Flame Structure Through Laser Plasma Diagnostics

Wendong Wu
Washington University in St. Louis

WASHINGTON UNIVERSITY IN ST. LOUIS

Department of Energy, Environmental & Chemical Engineering

Dissertation Examination Committee:

Richard Axelbaum (Chair)

Pratim Biswas

Benjamin Kumfer

Jay Turner

Alian Wang

Brent Williams

Gregory Yablonsky

FUNDAMENTAL STUDIES OF FLAME STRUCTURE

THROUGH LASER PLASMA DIAGNOSTICS

by

Wendong Wu

A dissertation presented to
The Graduate School
of Washington University in
partial fulfillment of the
requirements for the degree
of Doctor of Philosophy

August 2017
St. Louis, Missouri

<u>Table of Contents</u>

List of Figures

List of Tables

List of Symbols

E Energy, J

gi Degeneracy of the state I

H Enthalpy, J

k_B Boltzmann constant

p Pressure, $N/m2$

T Temperature, K

γ Ratio of the specific heats

ρ Density, $kg/m3$

a_g Strain rate, s^{-1} the derivative of the velocity

$\emptyset$ Equivalence ratio (normalized air to fuel ratio)

Z Mixture fraction

M^2 Beam quality factor

λ Wavelength, nm

A Transition probability

g_i Degeneracy of level i

N Number density of the particular atomic species.

<u>Acknowledgments</u>

Dedicated to my parents.

Your love in the past 28 years is the greatest thing one could ever expect.
Whenever I have a setback, your support will comfort me and get me back to track.
I will not able to achieve this much without you.

ABSTRACT OF THE DISSERTATION

FUNDAMENTAL STUDIES OF FLAME STRUCTURE

THROUGH LASER PLASMA DIAGNOSTICS

by

Wendong Wu

Doctor of Philosophy in Energy, Environmental & Chemical Engineering

Washington University in St. Louis, 2017

Professor Richard Axelbaum, Chair

Increasing concerns about air pollution and global climate change are drawing attention to the

need for efficiency improvements and emission reductions for combustion processes, which

account for more than 85% of energy production in United States. Combustion efficiency and

emissions are affected by the mixing and reacting of fuel and oxidizer. Understanding such

behavior plays a critical role in flame structure studies and combustion optimization. However,

experimentally obtaining mixture fraction, which is a widely used quantity to describe the

mixing behavior, has proven to be a challenge, especially for heavier hydrocarbon fuels or fuel

rich flames. Moreover, measuring flame temperature simultaneously with mixture fraction adds

complexity into the experimental setup. In this dissertation, laser plasma diagnostics techniques

were developed to provide a straightforward method to simultaneously obtain composition and

temperature measurements. The capability of these novel techniques is applicable to more

complex fuels and a broader range of equivalence ratios than has heretofore been possible, and

facilitates a better understanding of flame structure.

Laser-induced breakdown spectroscopy (LIBS) is proposed as an alternative method of measuring mixture fraction. A back-scattering setup is utilized to mitigate the beam steering effects in non-uniform and unsteady flames. The calibration for the LIBS system was completed in an ethylene-air premixed flame under a broad range of equivalence ratios. The elemental species distributions for H, C, N, O were measured in a counter-flow diffusion flame. The measured mixture fraction compared favorably with the numerical results from OPPDIF flame code. On the basis of LIBS measured elemental species profile, the preferential diffusion effect was analyzed.

Utilizing the sound emission from laser-induced plasmas, acoustic-based laser induced breakdown thermometry (LIBT) was developed as a novel method for flame temperature measurement. The established correlation between the optical emission and acoustic emission in a premixed flame demonstrated that the acoustic signal can serve as an internal standard in the gas phase LIBS measurement. The influences of flame temperature and composition on the acoustic signal were investigated independently. The composition effect was found to be second order comparing to the temperature effect. The statistics of the LIBT measurement were also analyzed to better understand the distribution of samples. Furthermore, the temperature and gas density distributions in a counter-flow diffusion flame were measured using LIBT and were found to compare favorably with numerical results. To evaluate the possibility of simultaneous composition and temperature measurement using laser plasma diagnostics, the spatial and temporal resolutions of LIBS and LIBT were carefully examined. The accuracy of LIBT technique was analyzed as a function of sample size from a statistical perspective. The results demonstrated that LIBT has spatial and temporal resolutions comparable to that of LIBS. Finally,

a preliminary study using a Burke- Schumann flame and a Hencken burner was performed to understand the influence of turbulent flow.

Measuring composition and temperature simultaneously using laser plasma diagnostics provides substantial benefits over traditional measurement technique. However, in exchange for such benefits, information on major species concentrations can no longer be directly measured. To infer the molecular species profile from the elemental species profile, the underlying partial-equilibrium assumption was examined. Among partially-equilibrated reactions, the water-gas shift (WGS) reaction is most often assumed to be in equilibrium because of its important role in the high temperature zone. Thus, the equilibrium domain of WGS reaction was systematically studied in different hydrocarbon flames under varying strain rates to evaluate the validity of partial equilibrium assumption. The underlying mechanism for WGS-equilibrium was also examined. The results suggested that even though the WGS reaction has a broad partial-equilibrium domain in syngas, methane, ethylene and propane flames, the mechanisms responsible for partial equilibrium were very different. In hydrocarbon flames, the water-gas-shift reaction can achieve partial equilibrium even though the two elementary reactions behind it are not equilibrated.

Chapter 1: Introduction

1.1. Background

The sources of primary energy production in United States can be divided into 3 sectors, namely, fossil fuel energy, which includes coal petroleum and natural gas; nuclear energy; and renewable energy, which contains biomass, hydroelectric power, geothermal, solar/PV and wind. Among them, only nuclear energy and part of renewable energy (hydroelectric, geothermal, solar/PV and wind) can be considered as non-combustion energy. The total energy production from combustion sources (in quadrillion BTU) and the percentage of that amount among all energy sources from 1949 to 2015 [1] in U.S are shown in Figure 1.1. The data indicates that the percentage of combustion sourced energy slowly decreased from 95.5% in 1949 to 87.6 % in 2015, while featuring a near triple increase in the absolute amount produced. The increase on combustion sourced energy is even more dramatic for energy impoverished developing countries like India and China in the past years. It is also worth noticing that the percentage of combustion sourced energy in the total primary energy production reached its minimum at around 85% from year 1995 to 2010, then climbed back to 87.6% in recent years with an expanding total production. Part of the reason behind this trend is that after the Fukushima Daiichi nuclear disaster in 2011, the public confidence in the safety of nuclear power has been greatly damaged globally. All but two nuclear power stations in Japan were shut down a year after the disaster. The loss of 30% of Japan's generating capacity led to a much greater reliance on LNG and coal.
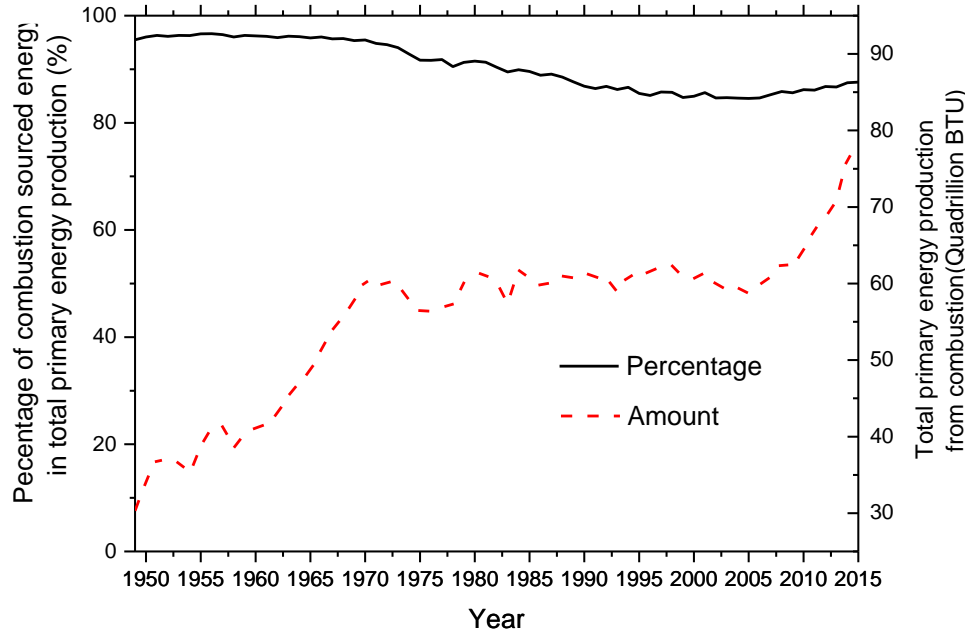
Figure 1.1 Percentage of total energy production and total combustion energy production coming from combustion in U. S from 1949 to 2015 (U.S.E.I [1]).

The well-perceived difficulty in integrating the renewable energy sources (RES) into existing grid is a contributing factor of such trend. Large-scale deployment of RES leads to significant reduction in the grid inertia because they do not provide rotational mass as conventional synchronized generators. Our studies (Appendix A) suggested that the reduced inertia have a significantly negative impact on the system dynamics. Such impacts should be carefully taken into consideration when integrating more RES into the grid and should be compensated by employing faster primary control. Moreover, RES has much higher land use requirement (characterized by land area used per unit capacity) compared to combustion sourced energy, especially considering its low capacity value and power factor. Our studies (Appendix B) suggests that 5 times more land is required to power an average U. S urban area by RES. Thus,

2

the insights provided by these studies and the trend in energy production for recent years suggest the irreplaceable role of combustion in human society today and in the near future. Combustion, which has powered human society since ancient times, still serves as the dominant source of energy conversion in modern society. However, there has been increasing concern about the pollution caused by products of combustion, which including unburned and partially burned hydrocarbons, nitrogen oxides, carbon monoxides, sulfur oxides, and particular matter in various forms. Carbon dioxide emission is also of great concern due to its impact on global climate change. Hence, improving the efficiency and reducing the emission from combustion are of great importance, which places higher demand on understanding and optimizing the combustion process.

1.2. Scalars in interpreting flame structures

Because the combustion efficiency and emission are determined by the mixing and reacting of fuel and oxidizer; understanding the mixing and reacting behavior plays a central role in fundamental flame studies and combustion optimization. In a premixed flame, the composition of the pre-mixture is generally described by the global equivalence ratio which is defined as $\emptyset = \frac{\frac{F}{A}}{(\frac{F}{A})_{st}}$ [2], where $\frac{F}{A}$ is the fuel-air ratio and the subscript "st" stands for stoichiometric. In contrast to premixed systems, in non-premixed systems, the fuel and oxidizer are supplied in separate streams; hence, the global equivalence ratio is no longer sufficient. Instead, the fuel to air ratio can be described by the local equivalence ratio whose expression is given by $\emptyset local = \frac{(\frac{F}{A})_{local}}{(\frac{F}{A})_{st}}$ [2]. The local equivalence ratio provides information on how the local region deviates from the stoichiometric condition. However, the local equivalence ratio is of only limited benefit in

decoupling the complexity of the reacting flow, where the reaction term is not only nonlinear but also couples the energy and species equations. Another variable, which has demonstrated greater value in non-premixed systems, is the mixture fraction. The mixture fraction can eliminate the reaction term in all but one of the n+1 species and energy equations and thus simplifies the solution of reacting flow problems (i.e., the determination of species concentration and temperature based on this variable), as will be illustrated in the following part.

In combustion processes, the conservation equation for molecular species i in the Shvab-Zeldovich form can be written as

$$L(Y_i) = \rho \frac{\partial Y_i}{\partial t} + \rho V \cdot \nabla Y_i - \nabla \cdot (\rho D_i \nabla Y_i) = w_i \qquad (1.1)$$

where Y_i is the mass fraction for a species i, ρ is the density, V is the velocity, D_i is the diffusivity of species i and w_i is the net generation rate of species i. The four terms in this equation stand for the unsteady term, the convection term, the diffusion term, and the chemical reaction term, respectively [3]. By taking a reference species B, denoted by "b", we can define a stoichiometrically-weighted mass fraction $Y_i^S = \sigma_{i,n} Y_{n,b}$, where $\sigma_{i,n} = \frac{W_i(v_i'' - v_i')}{W_n(v_n'' - v_n')}$. Here W_i stands for the molecular weight for species i; v_i'' and v_i' stands for the stoichiometric number after and before reaction of species i and subscript B is a boundary location. Through this conversion, Equation (1.1) can be transformed into the following form:

$$L(Y_i^S) = w \quad i = 1,2,3,\ldots N \qquad (1.2)$$

where $w = \frac{W_n(v_n'' - v_n')}{Y_{n,b}}$

Taking the equal diffusivity assumption, one can further couple Equation (1.2) for two different molecular species, yielding

4

$$L\left(Y_i^s - Y_j^s\right) = 0 \qquad\qquad (1.3) \ .$$

The reaction source term is eliminated for the new variable $Y_i^s - Y_j^s$ through this approach. Any

scalar S that satisfies the equation $L(S) = 0$, for example $Y_i^s - Y_j^s$, is called a conserved scalar.

A similar approach can be utilized to couple Equation (1.2) and the energy conservation

equation, Equation (1.4).

$$L(h^s) = \frac{\partial p}{\partial t} - \sum_{i=1}^{N} h_i^o w_i \qquad\qquad (1.4)$$

For this equation, instead of assuming equal diffusivity assumption, as was done for the species

equations, unity Lewis number must be assumed. It is worth noticing that, in a mixture

consisting of N species of Y_i consisting of L elements, we can define an element mass fraction Z_k

of element k as $Z_k = \sum_{i=1}^{N} \mu_{i,k} Y_i$, where $k = 1,2,3,4$ .... and $\mu_{i,k}$ is the mass fraction of the kth

element in the ith species. Since the elements are neither generated nor destroyed during

chemical reactions, Z_k is a natural conserved scalar as long as the equal diffusivity assumption

for different molecular species is valid.

The mixture fraction can be obtained by normalizing any conserved scalars

$$Z = \frac{S - S_2}{S_1 - S_2} \qquad\qquad (1.5)$$

where S is a conserved scalar, 1 represents the fuel boundary and 2 represents the oxidizer

boundary. The mixture fraction should be seen as more a matter of form, than substance;

physically, it represents the local mass fraction of the mass originated from the fuel stream. It

equals 1 in the fuel boundary, and 0 in the oxidizer boundary. When $S = Z_k$, where Z_k is the

elemental mass fraction of atomic species k or the total number of k atoms, then $\xi_k = \frac{Z_k - Z_{k2}}{Z_{k1} - Z_{k2}}$,

where ξ_k is the elemental mixture fraction from element k. The elemental mixture fractions should all equal each other when the equal diffusivity assumption is valid.

The greatest advantage of using mixture fraction is that any conserved scalars are linearly related to the mixture fraction; which greatly simplifies the solutions in a reacting flow. The equal diffusivity assumption and unity Lewis number assumption are required when the estimation of the elemental mass fraction and the temperature profile is desired, respectively. However, in real systems, deviations from these assumptions limit the accuracy of flame analysis based on the mixture fraction. The deviation from the equal diffusivity assumption has been extensively reported by previous literature. For example, Bilger *et al.* [4] have reported that there is considerable divergence between different elemental mixture fractions due to preferential diffusion; especially at the flame front in a methane-air diffusion flame. Barlow *et al.* [5] illustrated the limitation of mixture fraction as a variable by comparing two simulation results that assume equal diffusivity and full transport respectively. To address the discrepancy caused by preferential diffusion, a widely used modified expression for the mixture fraction was proposed by Bilger *et al.* [6]

$$Z = \frac{\frac{2(Y_C - Y_{C,2})}{W_C} + \frac{2(Y_H - Y_{H,2})}{2W_H} + \frac{(Y_O - Y_{O,2})}{W_O}}{\frac{2(Y_{C,1} - Y_{C,2})}{W_C} + \frac{2(Y_{H,1} - Y_{H,2})}{2W_H} + \frac{(Y_{O,1} - Y_{O,2})}{W_O}} \quad (1.6)$$

where Y_k and W_k represent the mass fraction and atomic weight of element k. Another expression was proposed by Barlow *et al.* [5] in which dropping the oxygen term from Equation (1.6) demonstrates its consistency with the mixture fraction obtained from Equation (1.6). These formulations preserve the stoichiometric value of the mixture fraction, while remaining independent of the effects of differential molecular diffusion. However, they are essentially

6

averaged elemental mixture fractions. Forcing the diverged elemental mixture fractions to an averaged value actually makes the interpretation of the elemental mass fraction become inaccurate. Moreover, as long as a formulation does not include all elements existing within the flow, the resulting variable deviates from the physical meaning of mixture fraction, which is the mass fraction of the mixture coming from the fuel side. Thus, such approaches cannot address inherent discrepancies resulting from preferential diffusion, which is not trivial. In this study, the preferential diffusion will be discussed in more detail with experimental and numerical obtained elemental species distribution.

1.3. Partial equilibrium assumption in combustion and Water-Gas-Shift(WGS) reaction

An important advantage of using the mixture fraction is that if we assume the chemistry is infinitely fast (i.e., the system is in equilibrium); the molecular species concentrations can be directly determined from Z. Bilger *et al.* [4] suggested that since the atomic composition and enthalpy at any point is determined by the mixture fraction, there is only one possible molecular composition, Y_i, which is determined by fully reacted or chemical equilibrium conditions. The chemical equilibrium situation is more likely to happen in real systems than the fully reacted case, especially in the vicinity of the flame front. Thus, studying the chemical equilibrium behavior in the flame is necessary to take advantage of estimating the species profile from the mixture fraction. Instead of the infinite fast chemistry, the finite rate chemistry in real systems is more likely to result in partial-equilibrium, which is defined as one or several reactions being at equilibrium while the whole system is not. Partial equilibrium has been extensively reported in both premixed [7-11] and diffusion hydrocarbon flame systems [12-16].

Among partially-equilibrated reactions, the water-gas shift (WGS) reaction is most often assumed to be in equilibrium because of its important role in the high temperature zone within the flame [1-6]. The water-gas shift reaction, $CO + H_2O \rightleftharpoons CO_2 + H_2$, is slightly exothermic at 41.1 kJ (10 kcal) per mole. As shown in Table 1.1, the water-gas shift reaction is unique when compared with other important overall reactions within the H_2, H_2O, CO, CO_2 system because of its relatively small enthalpy change, which suggests a reversible nature. As a result, this reaction may achieve equilibrium more rapidly than other important overall reactions.

Table 1.1 Enthalpy change for overall reactions

Reaction	Formula	ΔH (kJ/mol)
Water-gas shift	$CO + H_2O \rightleftharpoons CO_2 + H_2$	-41.1 kJ/mol
Hydrogen combustion	$2H_2 + O_2 = 2H_2O$	-290 kJ/mol
CO combustion	$2CO + O_2 = 2\,CO_2$	-283 kJ/mol
Ethylene pyrolysis	$C_2H_4 = C_2H_2 + H_2$	174 kJ/mol

The water-gas shift reaction can be represented as the sum of elementary reactions from the detailed mechanism. In the simplest case it can be written as:

$$H + H_2O \leftrightharpoons OH + H_2 \qquad \text{R1}$$
$$CO + OH \leftrightharpoons CO_2 + H \qquad \text{R2}$$

with the overall reaction -the WGS reaction- being the sum of these two reactions:

$$CO + H_2O \leftrightharpoons CO_2 + H_2 \qquad \text{R3}$$
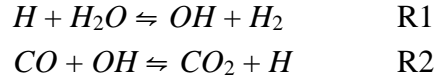
The quotient of the overall reaction is $Q_3 = [CO_2][H_2]/[CO][H_2O]$. For reactions R1 and R2 the quotients are $Q_1 = [OH][H_2]/[H][H_2O]$ and $Q_2 = [CO_2][H]/[CO][OH]$, respectively. Equilibrium can be assumed for the WGS reaction when Q_3 approaches the equilibrium constant for R3 ($K_{eq,3}$).

In addition to the practical benefit of making this assumption, efforts to distinguish the domain of WGS equilibrium are widespread in the literature. Warnatz $et\ al.$[17] evaluated experimental and asymptotic results for the premixed H_2-CO system and suggested that at low H_2 or H_2O concentrations equilibrium of R1 is retarded, and at lower temperatures (T<1800 K) equilibrium of R2 fails. In either case, equilibrium is not achieved for the WGS reaction.

In a diffusion flame, the WGS reaction on the oxidizer side is difficult to analyze experimentally because the concentrations of H_2 and CO are too low to measure accurately. Thus, experimental investigations of equilibrium for the WGS reaction have been mainly conducted on the fuel side. Drake $et\ al.$ [18] found that in a syngas counterflow diffusion flame, R2 is slower than R1, and the WGS reaction achieves partial equilibrium only at low strain rates and for temperatures above 1900 K. In a methane-air diffusion flame, Bilger $et\ al.$ [4] found that the WGS reaction is equilibrated for a range of mixture fractions from 0.033 to 0.047, while the H_2-O_2 system is far

9

from equilibrium. They concluded that since R2 dominates CO consumption, the consumption of hydrogen is the factor controlling the oxidation of CO in the oxidizer side of the flame; thus, R1 and R2 are coupled. Mitchell *et al*. [13] compared the quotient with the equilibrium constant of the WGS reaction calculated from the measured major species profiles in a methane-air diffusion flame. Their results suggested that the WGS‑ reaction is approximately equilibrated in a zone encompassing the flame front, where the local equivalence ratio is about unity. On the fuel-rich side, the partial-equilibrium condition breaks down at a local equivalence ratio of approximately 2.5, corresponding to a temperature of 1500 K. Barlow *et al*. concluded, through numerical studies, that WGS equilibrium is easier to achieve under the equal diffusivity assumption than with full molecular transport. They found that the relative importance of molecular diffusion and turbulent transport can be revealed by the behavior of WGS equilibrium [5].

Additional results concerning the role of the WGS-reaction in flame processes are summarized in Table 2. Though the WGS reaction has been studied extensively both experimentally and numerically, most analyses have been conducted for simple fuels like syngas and methane, not for higher hydrocarbons. The equilibrium domain for the WGS-subsystem will be significantly influenced by the composition of the chemical mixture, and thus, it is important to identify these domains for a range of hydrocarbons and to study the underlying chemistry in detail. Moreover, the mechanisms responsible for the WGS-equilibrium may differ among fuels. Thus, in this study, the equilibrium domain and equilibrium mechanism of WGS reaction will be studied numerically for syngas and a number of hydrocarbon diffusion flames. The equilibrium domains will also be systematically analyzed under varying strain rate.

Table 1.2 Previous studies of the WGS-reaction in flame processes

Author	Year	System	Approach and/or key findings
Warnatz [17]	1979	Syngas-air premixed flame	The low temperature and low H_2/H_2O concentrations determine the equilibrium break-down for R1 and R2, respectively.
Mitchell [13]	1980	Methane-air diffusion flame	The WGS equilibrium was used to determine whether R1 and R2 are co-equilibrated.
Drake & Blint [18]	1988	Syngas-air counterflow diffusion flame	R2 is slower than R1. The WGS reaction achieves partial equilibrium only under low strain rates and for temperatures above 1900 K.
Smyth [19, 20]	1990	Methane-air diffusion flame	Partial equilibrium for R1 and R2 was examined by measuring the OH concentration experimentally.
Chung & Williams [21]	1990	Syngas-air diffusion flame	The region of WGS equilibrium is broad, bounded on the oxidizer side by a thin zone of hydrogen oxidation and on the fuel side by a thin zone of sudden WGS freezing.
Barlow [22]	2000	Syngas-air turbulent diffusion	Unlike for laminar flames, partial equilibrium for the WGS reaction is not a good approximation for turbulent jet flames.
Barlow [5]	2005	Methane-air turbulent diffusion flame	The relative importance of molecular diffusion and turbulent transport can be revealed by the behavior of WGS equilibrium.
Hsu [23]	2011	Syngas-air counterflow flame (numerical)	The decrease in the CO to H_2 ratio of the syngas composition shifts the dominating reaction from R2 to R1.

1.4. Composition measurement in combustion and LIBS

One of the challenges with the mixture fraction approach is that experimentally measuring mixture fraction in a broad range of combustion system is difficult, especially when higher spatial and temporal resolution is desired. Generally speaking, gas sampling methods are intrusive to the flame with low spatial and temporal resolution. Laser diagnostic methods, being non-intrusive and offering good spatial and temporal resolution, have been preferred in recent years. Raman spectroscopy is perhaps the most popular method among the laser based diagnostics. Using Raman spectroscopy, the mixture fraction is obtained through the measurement of major molecular species [5, 22, 24-27]. With the addition of Rayleigh or Raman scattering technique, the molecular concentrations can be simultaneously measured with high temporal and spatial resolution. However, due to the weak signal strength, minor species cannot be effectively measured with Raman spectroscopy. While the mixture fraction can, in principle, be estimated from a measurement of major species, inaccuracies occur when a significant amount of minor species or combustion intermediates exist. Moreover, for fuels containing C-C bonds, the C-C Raman spectra is difficult to differentiate from the Raman spectra for CO and O_2. In fuel-rich hydrocarbon flames and diffusion flames, not only are the concentrations of combustion intermediates not negligible, but broadband fluorescence from species like PAH can overlap important Raman channels. Such background interferences severely restrict the possible fuels where Raman can be applied. Moreover, the extent to which the weak Raman signal can be enhanced by utilizing higher laser energy is limited by optical breakdown, and this is particularly challenging in a combustion system where particles are presented. For these reasons, the use of Raman spectroscopy to obtain molecular species profile has been limited to clean, dilute

laboratory flames of hydrogen, carbon monoxide, syngas, methane and DME [28, 29]. Laser

induced fluorescence (LIF) is another molecular species measurement that is often employed as a

supplement to Raman spectroscopy to measure minor species [25]. Unlike Raman, LIF requires a

specific wavelength to excite each species, which increases the complexity of the experiment.

Another approach is by adding trace elements like krypton to perform PLIF measurements [30,

31]. While this can be applied to a much broader range of systems, the accuracy of this approach

is affected by the preferential diffusion of the heavier tracing elements [32].

The complexity and intrinsic limitations of Raman spectroscopy and LIF can be warranted when

concentrations of molecular species are required. However, when mixture fraction or atomic

ratios are the primary goal, measurements of major species to deduce these quantities is overly

complicated and the measurements severely limit the types of flames that can be studied,

Needless to say, the restriction on fuel type and experimental conditions (e.g. the inability to

study heavier hydrocarbons, or systems containing condensed phases) is a severe limitation of

existing approaches to measuring mixture fraction or atom ratios. Thus, instead of deriving these

quantities from molecular species profiles, in this study, we introduced a new approach that

utilizes laser induced breakdown spectroscopy (LIBS) as a direct measurement of atomic ratios,

from which mixture fraction can be derived.

Laser-induced breakdown of a gas occurs when the beam from a pulsed laser is focused to a spot

and the local intensity of the electric field is high enough to atomize and ionize the gas to form a

plasma. The atomic emission spectra from the cooling plasma can be utilized to derive

information about the elemental composition of the sample. The quantitative nature of LIBS in

flames has been demonstrated in previous studies [33-41]. The emitted line intensity ratio of two

atomic species a and b can be expressed as

$$\frac{I_a}{I_b} = \frac{\lambda_b}{\lambda_a} \frac{(A_{mn}g_m)_a}{(A_{mn}g_m)_b} \frac{U_b(T)}{U_a(T)} \frac{N_a}{N_b} e^{-(E_{am}-E_{bm})/kT} = D(T)\frac{N_a}{N_b} \quad (1.7)$$

where λ is the transition wavelength, A_{mn} is the transition probability, g_m is the degeneracy of the upper level, $E_{am} - E_{bm}$ is the energy difference between the two upper levels, $U(T)$ is the partition function, and N is the number density of the particular atomic species. Once the plasma temperature is determined and if the plasma is optically thin within the spectral area of interest, the atomic number density ratio $\frac{N_a}{N_b}$ is linearly related to the measured emission intensity ratio $\frac{I_a}{I_b}$ by a spectroscopic constant $D(T)$. $D(T)$ can be determined by calibration of the LIBS system using mixtures of known elemental composition and temperature.

LIBS has been successfully employed to measure the ratio of atomic species utilizing distinct atomic emission lines from hydrogen, oxygen, nitrogen and carbon in combustion systems [33, 38, 39, 42-48]. However, most of work above mentioned are concerned about lean pre-mixtures and methane-air flames which is also a limitation for other existing methods like Raman spectroscopy. The potential of LIBS on a broader range of fuels and compositions has not been fully appreciated and exploited. Secondly, the intensity ratio between atomic emission lines was more often correlated to the equivalence ratio rather than the mixture fraction in these studies. A recent study by Mansour *et al* [49] reported mixture fraction measurement based on elemental mass fractions in a methane-air flame. The mixture fractions based on the elemental mass were compared to the mixture fractions(equivalence) based on a pair of atomic emission line ratio. However, the preferential diffusion [24, 50] which is the largest restriction in the mixture fraction concept has not been fully recognized and analyzed on LIBS measurement basis. Finally, when LIBS measurement is further expanded to non-uniform or unsteady combustion systems, the beam steering effect that caused by the changing flame front have not yet been

addressed. Such effects will produce significant deviation between the focusing volume and the probe volume, thus reducing the reliability of the measurement. In this study, a back-scattering optical setup was introduced instead of angled- scattering to mitigate the beam steering effect in non-uniform flames. LIBS will be applied in an ethylene-air counter-flow flame to obtain a direct measurement of atomic ratios, from which mixture fraction can be deduced. The potential of LIBS as a combustion diagnostic technique will be demonstrated in a counter-flow diffusion flame fueled by ethylene in a broad range of compositions ranging from lean to rich. A spatial resolution of 125 µm can be achieved and the preferential diffusion effect will be analyzed based on LIBS measurement.

1.5. Temperature measurement in combustion and LIBT

In addition to composition measurements, accurate temperature measurements are also crucial for fundamental flame studies. It is especially desirable if the flame temperature can be measured simultaneously with the composition. A variety of methods have been employed for making gas temperature measurements in flames. Broadly speaking, these methods can be classified into thermocouple-based or laser-based measurements. Thermocouple-based techniques have gained preeminence because they are inexpensive, robust, and easy to use. Unfortunately, these measurements are intrusive and require corrections due to radiative and conductive heat loss. New approaches like the rotating thermocouple technique (Appendix C, [51]) have been developed to correct for heat loss and with better spatial resolution than past techniques such as suction pyrometer. Nonetheless, laser-based methods are sometimes preferred as they are non-intrusive, and they offer the possibility of simultaneously obtaining information about composition. However, each method has its own merits and drawbacks. For example, absorption

spectroscopy only offers line-of-sight measurement, laser-induced fluorescence (LIF) requires a tunable laser and suffers from quenching effects. Under the assumption of the ideal gas law and constant pressure, temperature can be obtain from Rayleigh scattering and Raman scattering by measuring the density of non-reactive species and inferring temperature [52]. However, due to their low scattering cross sections, the collected signal is small, making it challenging to extract accurate data without long integration times. Coherent anti-Stokes Raman (CARS) has advantages in terms of signal strength, but is even more complicated experimentally compared with previously mentioned techniques. Thus, even with the enormous amount of efforts that have been devoted to flame temperature measurement, a simple and economical laser-based method to measure local temperature is still of great interest, especially when higher spatial and temporal resolution is preferred.

Among the various laser-based temperature measurement techniques, studies on laser-induced breakdown are very limited. Laser-induced breakdown of a gas occurs when the beam from a pulsed laser is focused to a spot and the local intensity of the electric field is high enough to atomize and ionize the gas to form a plasma. In recent years, the atomic emission spectra from the cooling plasma has been applied in combustion studies to obtain measurements of elemental composition via a process known as laser-induced breakdown spectroscopy (LIBS) [33-41].

The laser irradiance at the breakdown threshold has been reported to be related to the gas pressure by I $\propto P^{-\alpha}$[53], which agrees well with the inverse Bremsstrahlung absorption model. Utilizing the temperature dependency of the threshold laser pulse energy to initiate breakdown, Kiefer *et al* introduced laser-induced breakdown flame thermometry [54]. In this approach the laser energy is varied until breakdown occurs, and this energy is utilized to infer temperature via calibration measurements carried out in heated gas flows and post-combustion gases. A series of

proof-of-concept measurements were performed in a laminar methane/air flame and compared to reference data obtained from coherent anti-Stokes Raman scattering (CARS). The corrected LIBS temperatures show excellent agreement with those obtained by CARS. However, determining the breakdown threshold by statistics requires a number of laser shots at different energy levels, which significantly reduces the temporal resolution and complicates the measurement. This limitation is more pronounced when the temperature and elemental composition need to be measured simultaneously because the temporal resolution of the temperature measurement is much lower than that of composition measurement.

The acoustic signal from the laser-induced plasma offers an alternative to gas temperature measurement in flames. The acoustic signal has already been applied in solid-state LIBS measurement as an internal standard to normalize the pulse-to-pulse variation resulted from the matrix effect [55-57]. However, to the best of the authors' knowledge, such an application has not been adapted to LIBS in gas phase. While not directly related, the laser-induced plasma has been employed as a sound source to simulate a blast wave or a sonic boom in the laboratory [58-60] and in a recent study, Hosaya *et al*[61] performed non-contact, nondestructive vibration test of a structure based on a shock wave generated by laser-induced plasma. In these studies, the relationship between the density of the local gas and the acoustic signal from the laser-induced plasma has been explored both theoretically and experimentally. Based on the N-wave form assumption, the peak pressure, P, of the positive phase of the shock can be estimated from calculations presented by Brode [62]. Given a fixed energy and distance, the peak pressure can be expressed as $P = \alpha * \frac{\rho_0 c_0}{\gamma}$, where c_0 is the sound speed, γ is the specific heat, ρ_0 is the density. The c_0, γ and ρ_0 are all functions of local gas temperature. The change in the pulse amplitude and the evolution of the peak-to-peak time as a function of distance can be readily estimated by

using the theory of spherically spreading shock N-waves as described by Pierce[62, 63]. Thus, the amplitude of the shock wave can be correlated to the gas temperature of the focal region when the laser energy and detection distance remain constant. In this study, the relationship between the acoustic signal from the laser-induced plasma and the gas temperature will be explored. The concept of acoustic-based laser-induced breakdown thermometry will be introduced as a flame temperature measurement technique. The temporal resolution of the LIBT technique will also be analyzed.

Chapter 2: Objectives

In order to improve the efficiency and reduce the emission, this research is motivated to improve the fundamental understanding of the combustion process through laser plasma diagnosis. The laser-induced breakdown spectroscopy (LIBS) will be proposed to measure the atomic ratios and mixture fractions in the flame. From the elemental species perspective rather than the molecular species perspective, the application of LIBS technique will not only expand the mixture fraction measurement method into a broader range of fuels and equivalence ratios, but will also help better understand the preferential diffusion effect which is intrinsically bounded to the mixture fraction concept. The correlation between acoustic signal and optical signal from laser-induced breakdown will be investigated. The acoustic aided laser induced breakdown thermometry (LIBT) will be proposed as a novel method to measure the flame temperature. The statistics of LIBT measurement will be examined to evaluate the potential of simultaneous composition and temperature measurement. The application in turbulent systems will be studied preliminary. Finally, to infer the molecular species profile from the LIBS measured elemental species profile, the underlying partial-equilibrium assumption will also be examined.

The specific goal of this study can be laid out as following.

1. The laser-induced breakdown spectroscopy (LIBS) technique will be developed to measure the mixture fraction. The calibration will be performed on the McKenna burner in a range of equivalence ratios. The LIBS technique will be further evaluated in the counter-flow flame with numerically obtained mixture fraction profiles.

2. The preferential diffusion effect will be investigated both experimentally and numerically, on the basis of the numerically obtained and LIBS measured elemental species profiles.

3. The acoustic based laser-induced breakdown thermometry (LIBT)will be developed to measure the flame temperature. The concept will be validated on a McKenna burner with thermocouple measured temperature. The temperature and compositional effect will both be evaluated. The measurement will be further performed on the counter-flow flame and compared to the numerically obtained temperature profile.

4. The temporal resolution for LIBT and LIBS will be investigated on the statistics basis. The potential of simultaneous composition and temperature measurement will also be demonstrated.

5. The correlation between the acoustic signal and the atomic emission from laser induced plasmas will be studied in the air and in the flame to evaluate the potential of utilizing the acoustic signal as an internal standard to normalize the LIBS spectra.

6. The application of laser-induced plasma diagnostic technique in turbulent flames will be evaluated preliminary using the Hecken burner and Burke Schumann flames.

7. The partial-equilibrium of WGS reaction in the flame will be investigated numerically to help understand the combustion chemistry and utilize the elemental composition to infer the molecular composition.

.

Chapter 3: Elemental composition measurement using LIBS

Measuring mixture fraction in a broad range of combustion system has proven to be a challenge, especially when higher spatial and temporal resolution is desired. There are several major limitations on existing measurement methods. For molecular species based measurement, namely the Raman Spectroscopy, the fuel types are limited to simple fuels like methane and syngas. The measurement in the fuel rich region is restricted by the interference from PAH. Moreover, in a flame zone where the minor species concentrations are not negligible, tracking only major species could result in systematic errors. Alternatively, a trace element based technique like PLIF will inherently suffer from the difference in diffusivity between the trace element and the scalar of interest. To address these shortcomings, in this chapter, LIBS will be proposed as a mixture fraction measurement method from the elemental species perspective. A back-scattering setup will be introduced to mitigate the beam-steering effect in the non-uniform flames; and a Schott filter will be added to improve the dynamic range of the measurement. The LIBS measurement will be first performed on an ethylene-fueled McKenna burner to demonstrate its capability in fuels containing a C-C bond. Moreover, the equivalence ratios will be varied from lean to rich not only to valid its capability in fuel rich flames but also to establish the calibration profile for future measurements on other systems. The LIBS technique will be further evaluated in the counter-flow flame, and the results will be compared with numerically obtained mixture fraction profiles. Finally, the preferential diffusion effect will be investigated both experimentally and numerically on the basis of the numerically obtained and LIBS measured elemental species profiles,

3.1. Methods

3.1.1. Laser setup

The laser used in the LIBS system is a pulsed Nd:YAG laser (Continuum Surelite SL I-10) with a repetition rate of 10 Hz. The laser has a beam diameter of 6 cm; pulse width is 4-6 ns and the beam divergence is 0.5 mrad. The second harmonic 532 nm laser beam is focused by a convex lens with 100 mm focal length to the centerline of the counter-flow flame. The laser power output was measured by a thermal laser power sensor (10A-P-V3, OPHIR Photonics), which connects to a Bluetooth wireless interface (Quasar wireless interface, OPHIR Photonics). The measured power output was recorded on the PC end by StarLab 2.40 software interface (OPHIR Photonics). The relationship between laser output power and Q-switch delay under different voltage loads (1.29kV and 1.41kV) is shown in Fig.3.1. Under a voltage load of 1.29kV, the power output is negatively correlated with Q-switch delay if the Q-switch delay is larger than the critical Q-switch value at 183μs. The output range under this voltage is between 322 and 1580mW. Under a voltage load of 1.41kV, the critical Q-switch value is 168μs. The output range is between 391 and 2140mW. The Q-switch delay can be easily varied to control laser pulse energy during experiments. However, if not otherwise specified, in the following part of this study, the Continuum laser will be configured under a voltage load of 1.41kV with a Q-switch delay of 220μs, yielding a pulse energy of 180 mJ.
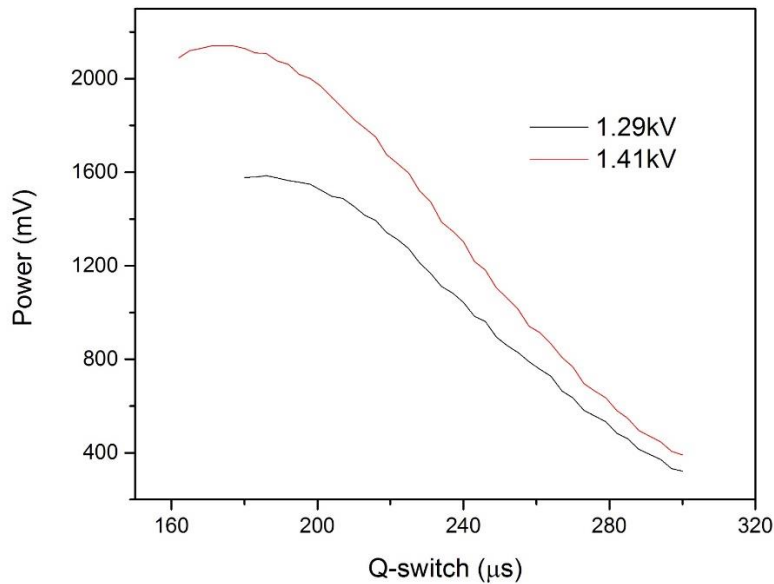
Figure 3.1 Power output of Continuum Surelite SL I-10 under different voltage loads.

3.1.2. Beam steering effect and back-scattering setup

LIBS has been successfully employed to measure the ratio of atomic species utilizing distinct atomic emission lines from hydrogen, oxygen, nitrogen and carbon in combustion systems [33, 38, 39, 42-48]. The collecting optics are generally positioned at 90 degrees relative to the direction of incident laser beams. However, most of work above mentioned are concerned about uniform laminar flames. When the LIBS measurement is further expanded to non-uniform or unsteady combustion systems, the incident laser beams and the optical signals emitted from the laser induced plasmas will travel through dramatically different light paths shot-to-shot caused by the changing flame front. This effect will produce significant deviation between the focusing volume and the probe volume, and reducing the reliability of the measurement. While the beam steering is generally not an issue in uniform laminar flames, it is much pronounced as we

observed in the non-uniform and turbulent flames. In this study, a back-scattering optical setup

similar to the ChemCam system [64, 65] on the Mars rover was introduced instead of angled-

scattering to mitigate the beam steering effect in non-uniform flames. As shown in Fig.3.2, the

plasma emission is collected by the same 100 mm focal length lens and focused onto an optical

fiber that is coupled to an ungated spectrometer (Ocean Optics USB2000+, 600lines/mm grating,

2048-element linear silicon CCD array.). A 600 nm long-pass filter is used to reduce the signal

from scattered laser light. By using the same convex lens to focus the laser beam and collect the

emission signal, the probe volume and collection volume converge regardless of the density

gradients arising from the flame. Thus, the plasma image can be consistently focused on the fiber

end for every shot.
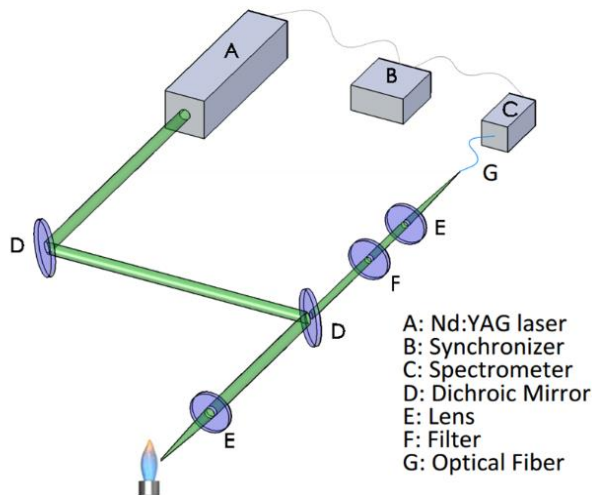
Figure 3.2. Schematic diagram of LIBS setup.

3.1.3. Dynamic range and Schott filter

A typical LIBS spectra obtained on the oxidizer side of a counter-flow diffusion flame is shown in Fig. 3.3 to identify the atomic emission lines that are utilized in this study. The lines observed in the spectra were indexed using the NIST Atomic Spectra Database. The nitrogen lines are clearly distinguishable at 742.3, 744.2 and 746.8 nm and the oxygen triplet lines are centered around 777 nm. The nitrogen and oxygen emission intensities were integrated over a region of 6.5 nm and 4 nm, respectively. The carbon emission peak, which consists of several overlapped lines, is positioned around 711 nm, and it is integrated over a region of 1.6 nm. The signal strength from carbon is particularly weak compared with the other three elements. Even in a fuel-lean flame (Fig. 3.3), the Hα line is still much more intense than the O emission line. Because the signal is a couple of magnitudes stronger than that from the C, N and O emission lines, it could greatly affect the dynamic range of the system. To address this, the Hα line was attenuated using an RG-665 filter (CVI Melles Griot); the transmissivity profile of which is shown in Fig. 3.4. The measured LIBS spectra was converted back to the original intensity using this profile. The intensity of Hα was integrated over a region of 4 nm centered at 656.28 nm. Recognizing the significant difference in signal strength for the different elements, measurements could be made using separate spectrometers. However, for the purpose of demonstrating that the proposed scalar measurements can be made simply and economically, a single, low cost spectrometer was employed. The ungated spectrometer was synchronized to the laser and an integration time of 1ms were used throughout this study. In order to accurately quantify the atomic intensity ratios, the spectral efficiency of the experimental setup was obtained using a calibrated halogen light source (Ocean Optics HL-2000-CAL).
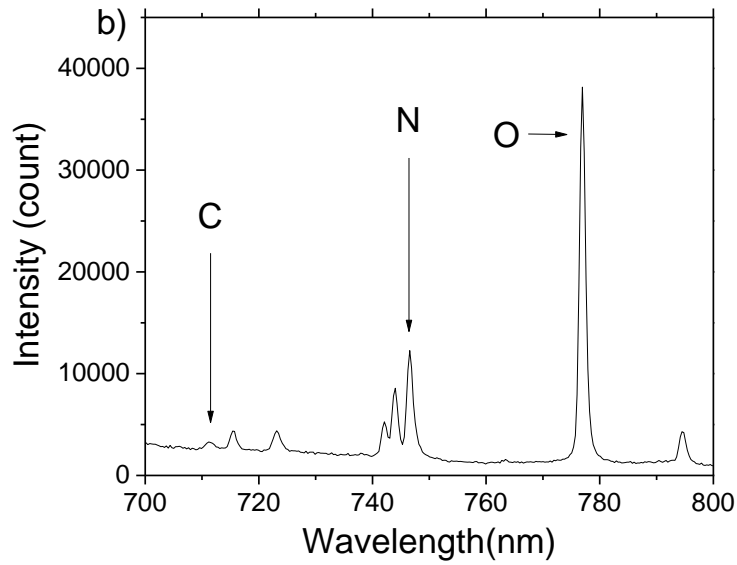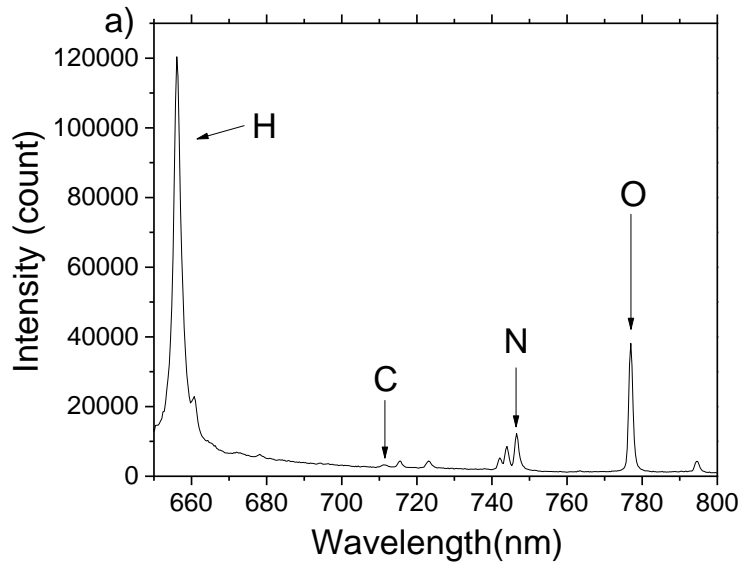
Figure 3.3. LIBS spectra for an ethylene-air flame with an equivalence ratio of 0.85: a) from 650 nm to 800nm and b) expanded view in the range of 700 nm to 800 nm.
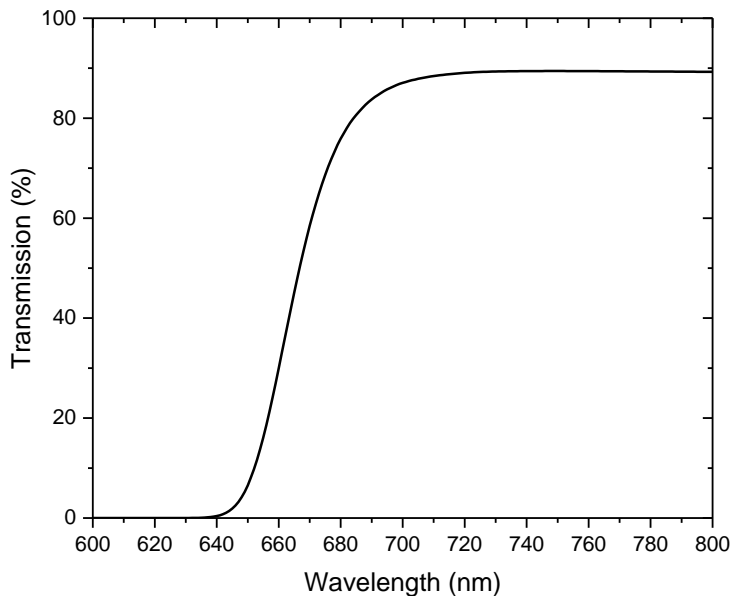
Figure 3.4. The transmission profile for the RG-665 filter

3.1.4. Burner setup

The calibration was performed in a premixed flame using a McKenna flat-flame burner (Fig.3.5).

The 60 mm-diameter burner head is composed of sintered stainless steel and is water-cooled.

The burner was fed with an ethylene-air mixture, and was shielded with a nitrogen shroud. Flows

were regulated by calibrated flow meters. In the counter-flow burner, an ethylene-air flame was

established between two 11-mm inner-diameter opposed jets spaced 10 mm apart. The schematic

of the counter-flow diffusion flame is shown in Fig. 3.6. An annular co-flow of argon was added

to both sides to eliminate oxidizer entrainment and to extinguish the wake flame that would exist

outside the region of interest. To ensure uniform laminar flow, a honeycomb core is placed 70

mm upstream of the exit of each tube and another core is placed 70 mm upstream of the first.

The counter-flow burner is mounted on a computer-controlled translational stage to provide a

27

resolution of 125 µm along the centerline of the flame. The flow rates are controlled by calibrated sonic nozzles. The flow speeds at the center-line of the counter-flow flame were measured by PDPA and matched by simulation at a strain rate of 140/s. Dry air was used to ensure that any hydrogen in the system originated from the fuel.
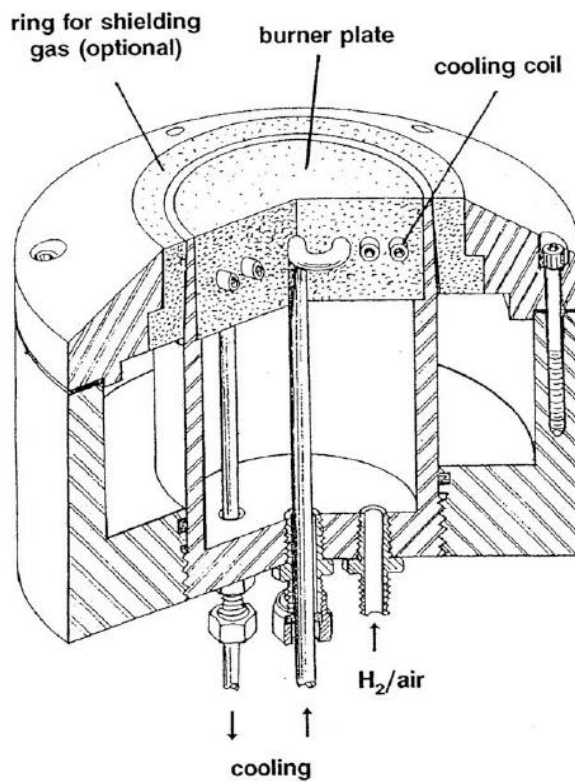
Figure 3.5. Sectional view of the flat flame burner (courtesy of www.flatflame.com)
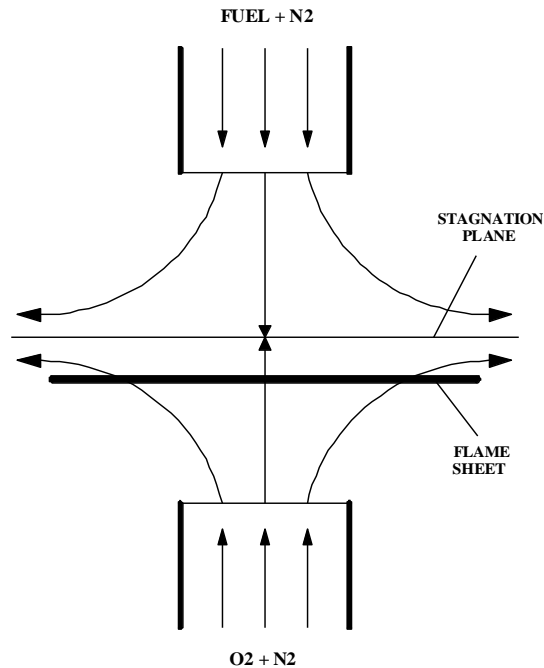
Figure 3.6. The schematic of the counter-flow diffusion flame.

3.1.5. PDPA measurement

The PDPA system used is a two-component TSI system operating in forward-scatter mode at a 30° off-axis angle. The transmitting optics have a focal length of 363 mm, generating a measurement volume with a 90 µm beam waist and 24 fringes with a 3.7 µm separation. The receiving optics have a focal length of 300 mm. At each location, 10^5 samples were acquired. Based on the optical setup employed, the velocity measurements have a ~2% margin of error.

The PDPA system can perform 2-d velocity and spherical particle size measurements simultaneously at a point at acquisition rates up to the 10^5 Hz range. Diameter measurements of translucent and opaque particles in the range of 0.5 µm up to a few mm can be obtained depending on the optical configuration, as well as velocity measurements up to about 1000 m/s. Measurements can be performed in both dilute and dense cold and combusting sprays.

3.1.6. OPPDIF simulation

For the comparison with experimental results, the counter-flow diffusion flame was modeled

using the OPPDIF flame code corresponding to PDPA measured flow rate. A total of 143 species

and 938 reactions were included in the mechanism, which combines the Appel, et al. [66] and

USC Mech Version II mechanisms, with chemistry up to pyrene from Wang and Frenklach [67].

3.2. Calibration in a premixed flat flame

The correlations between emitted line intensity ratios and actual atomic ratios were established by conducting LIBS experiments over a McKenna flat flame burner. The flow rates of ethylene and air were both regulated by calibrated flow meters, thus the elemental composition in the premixture was known. To reduce the influence of atmosphere air, the laser was focused on a spot right above the burner head along the centerline of the burner. The calibration was performed at equivalence ratios ranging from fuel-lean to fuel-rich conditions. The correlations between the line intensity ratios and the atomic ratios for C/O and H/O were established as shown in Fig. 3.7, where each data point is an average of 100 shots in the same location. The C/O atomic ratio ranges from 0.21 to 0.51, corresponding to an equivalence ratio from 0.63 to 1.53. Within this region, a linear correlation can be found between line intensity ratios and atomic ratios for both C/O and H/O with excellent accuracy ($R^2= 0.999$). This correlation serves as a calibration for the LIBS measurement. For the ethylene-air premixed flat flame, the C/H and N/O atomic ratios are expected to be constant if the influence from the ambient air is negligible. The distributions of C/H and N/O intensity ratios in Fig. 3.8 demonstrate that when the equivalence ratio is varied, the intensity ratios of C/H and N/O essentially remain unchanged.
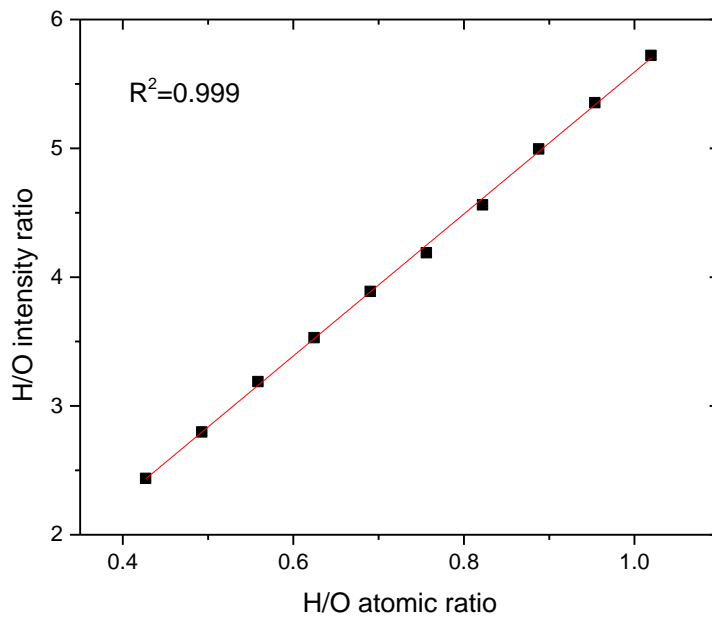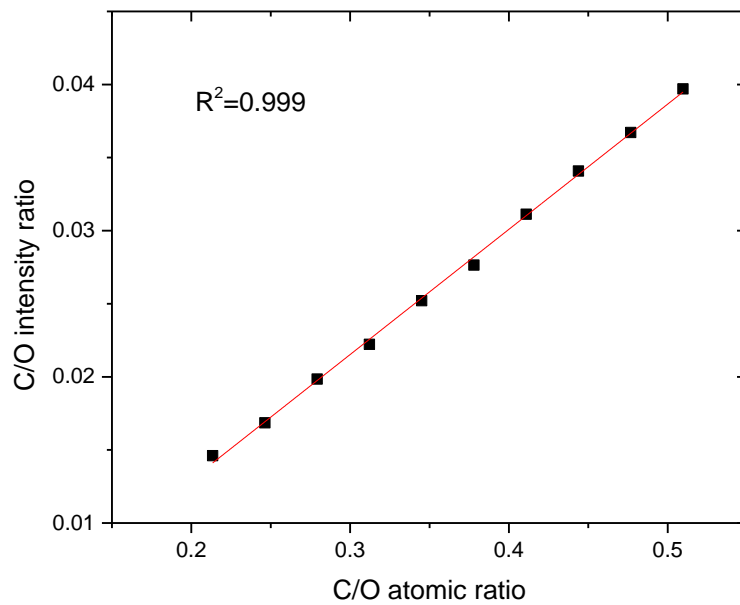
Figure 3.7. Correlation of C/O, H/O emission line intensity ratios versus C/O atomic ratios in ethylene-air premixed flames.
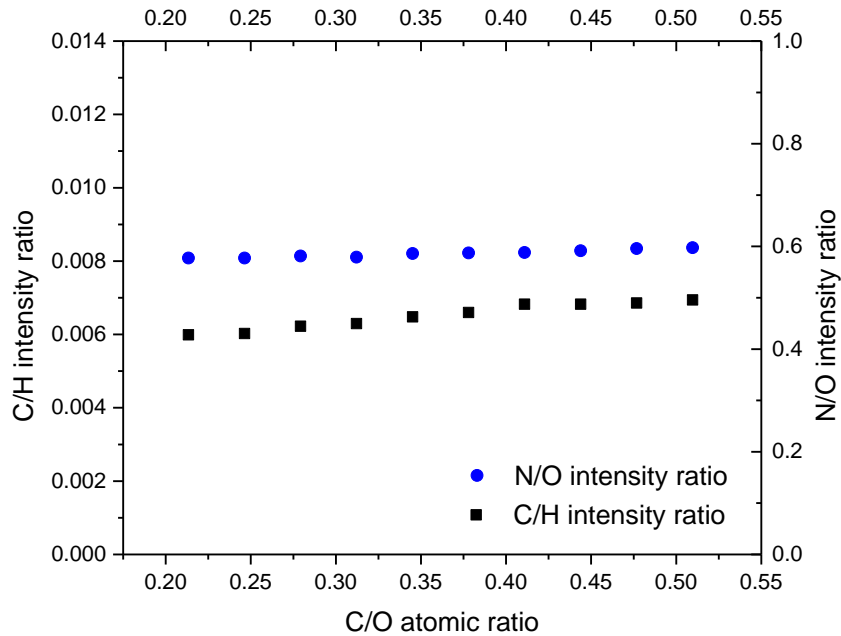
Figure 3.8. The distribution of C/H and N/O emission line intensity ratios in ethylene-air premixed flames.

Shot-to-shot variation in laser energy and signal detection could affect the accuracy and precision of the LIBS measurements. To evaluate such variations, the RSD (relative standard deviation) was obtained for the flat flame measurements. As shown in Fig. 3.9, the RSD in the flat flame generally is from 5% to 8% for the C/O intensity ratio while that of H/O ratio is around 1%. The higher uncertainty in C/O is attributed to the relatively weak carbon signal and as seen in Fig. 5, this effect is more pronounced in fuel-lean mixtures where less carbon is present.
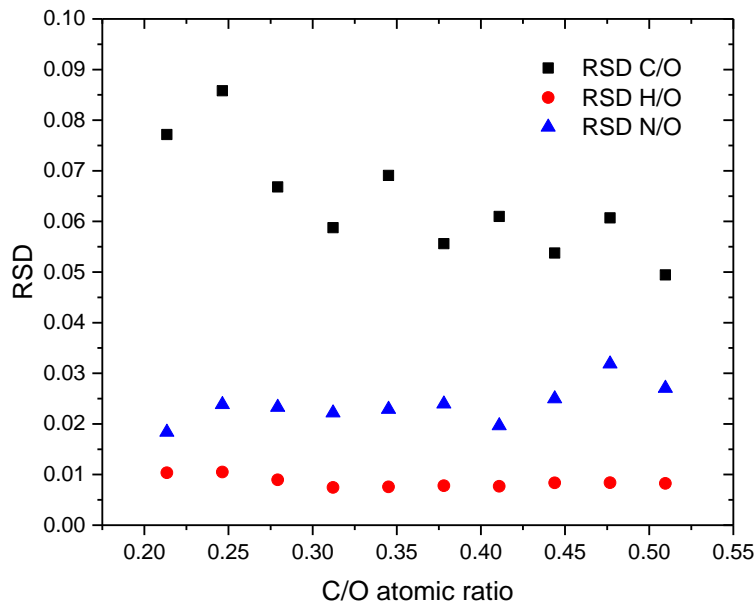
Figure 3.9. Relative standard deviation (RSD) for C/O, H/O and N/O intensity ratios in a flat flame.

3.3. Atomic ratio distributions and mixture fractions in counter-flow diffusion flames

Utilizing a computer-controlled translational stage with a spatial resolution of 125 µm, the measurement of atomic ratios was performed along the centerline of a counter-flow flame. When the measurement was made near the oxidizer supply tube, the signal from carbon emission line was barely distinguishable from the background due to the lack of fuel. This is also the case for the oxygen emission line near the fuel supply tube, which adds uncertainty to extremely large or small C/O ratio.

Fortunately, such extremes in C/O ratio are outside of the region of interest, as suggested by the following numerical studies. Figure 3.10 demonstrates typical atomic ratio distributions in the counter-flow flame. Using C/O ratio as an example, on the fuel boundary the C/O ratio has an

infinite value while the C/O ratio equals zero on the oxidizer boundary. Correspondingly, in

physical space, the C/O ratio is infinite at 0 cm, and zero at 1 cm, which is the separation

distance between the nozzles in the experiment. Under a strain rate of 140/s, a peak temperature

of 2035 K is reached at 0.538 cm. The stoichiometric C/O ratio for ethylene-air is 0.33, which is

found at 0.55 cm from the fuel side in this case. The C/O ratio at 0.595 cm is 0.1 ($\Phi = 0.3$) and

quickly rises to C/O = 5.0 ($\Phi = 15$) at 0.44 cm. In other words, a C/O ratio ranging from 0.1 and

5, which corresponding to a width of around 1.5 mm, can capture much of the high temperature

region of the flame. The RSD for different intensity ratios are investigated to validate the

precision of LIBS measurement in the counter-flow flame. The RSD is between 1% to 6% in a 3

mm wide region within the flame as shown in Fig. 3.11. Since both the reactions and

measurements were occurring in a relatively small region compared to the scale of the burner;

for the following part of this study, the boundary for the fuel stream side (i.e., the location shown

as X=0) was defined as the location where oxygen was first detectable from the fuel boundary,

instead of actual physical boundary of the burner.
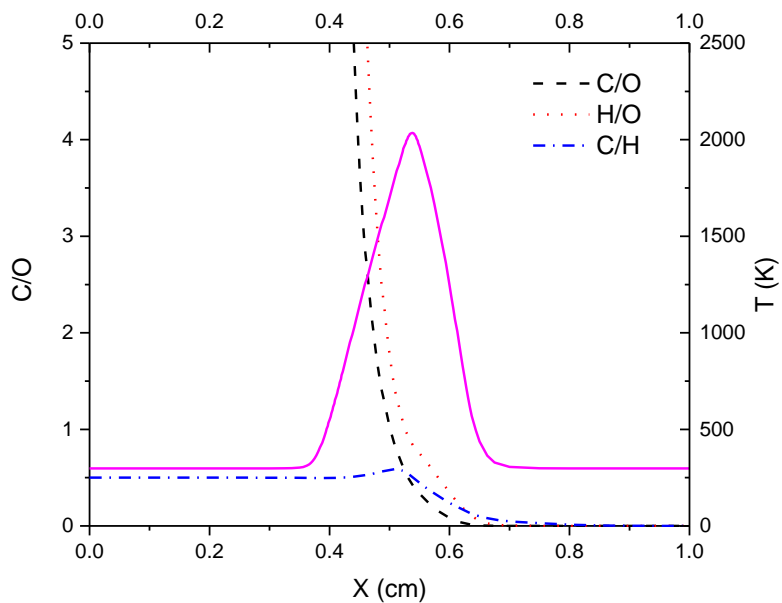
Figure 3.10. Simulation results for typical C/O, H/O and C/H atomic ratios and the temperature distribution in physical space. The simulation was performed under a strain rate of 140/s.
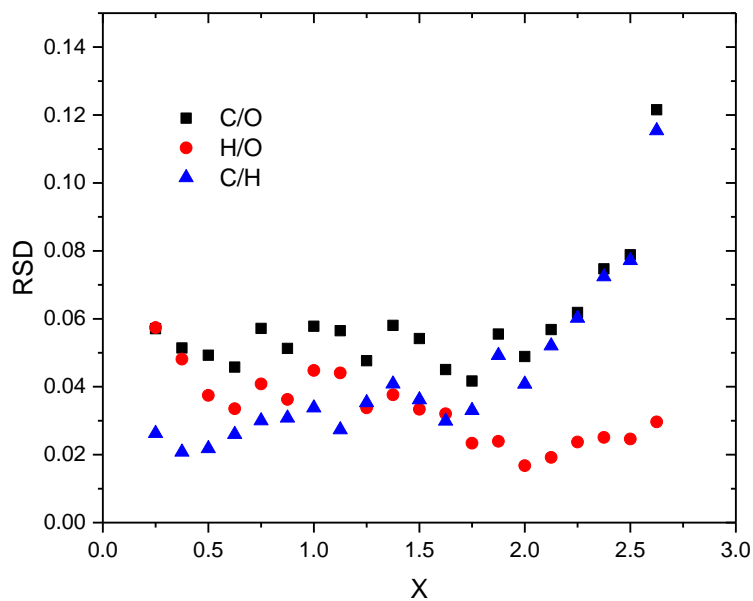
Figure 3.11. RSD for C/O, H/O and C/H intensity ratios in a counter-flow ethylene flame.

Considering the possibility of subtle differences in exact flame location between the experiments and simulations due to fluid mechanical differences, the location of the temperature peak was used as a physical point of reference for which to compare the simulations with the experiments. To experimentally obtain the location of the peak temperature the breakdown threshold was employed. It was demonstrated in previous literature that the breakdown threshold is strongly a function of temperature and only a weak function of composition[54]. For example, a temperature increase of 1500 K increases the breakdown threshold 30 mJ while a change in equivalence ratio from 0 to 2 varies the breakdown threshold by less than 2 mJ. An experiment to validate the negative correlation between the breakdown threshold energy and the flame temperature was also performed under 2 different strain rates in the counter-flow diffusion flame as shown in Fig. 3.12. Even using bare eye as the criteria of breakdown events and measuring the laser output power, the peak temperature region can be easily distinguished under both strain rates. Since measuring laser output power introduces more error into distinguishing the location of peak temperature and the pulse energy can be considered to be negatively correlated to the Q-switch delay under the same voltage load as previously discussed, the location of peak temperature within the flame can be determined by identifying where the lowest Q switch delay value is required for achieving steady breakdown. After determining this, the locations of peak temperature were matched for the experiments and simulations and in this way a direct comparison of small differences in C/O ratio between the experiment and simulations could be ascertained.

In Fig. 3.13, a 3.25 mm wide region near the stoichiometric location was selected to illustrate the C/O ratio distribution under a strain rates of 140/s. Good agreement is found between the numerically and the experimentally obtained C/O ratio distribution curves when using the peak

temperature location as the common physical reference point. The numerically and

experimentally obtained H/O atomic ratio distributions are presented in Fig. 3.14 and are shown

to be in good agreement as well.
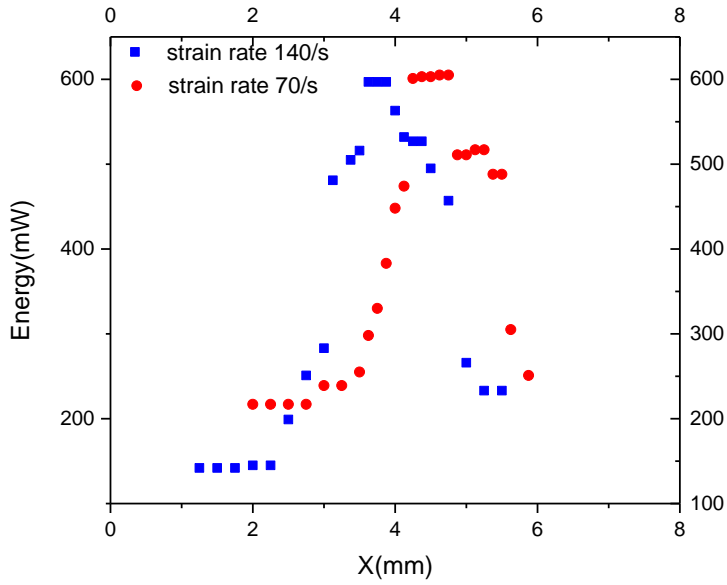
Figure 3.12. The breakdown threshold laser output energy in the counter-flow diffusion under a strain rate of 70/s and 140/s, respectively.
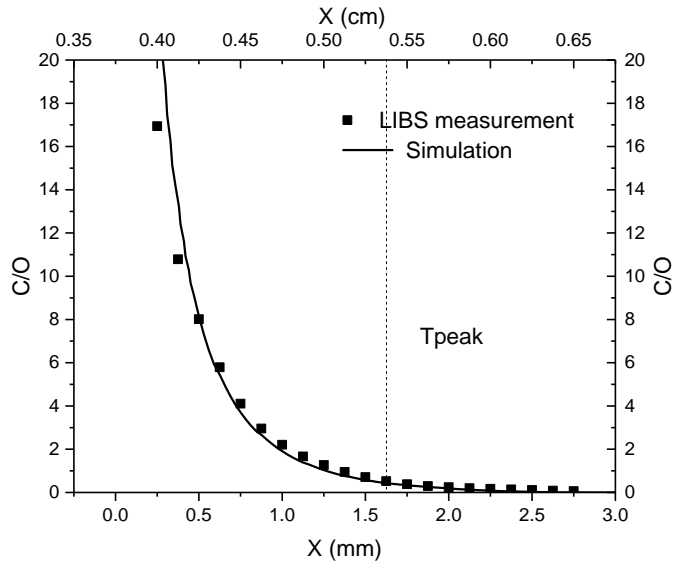
Figure 3.13. A comparison between the C/O ratio obtained from the LIBS measurement to that obtained by simulation.
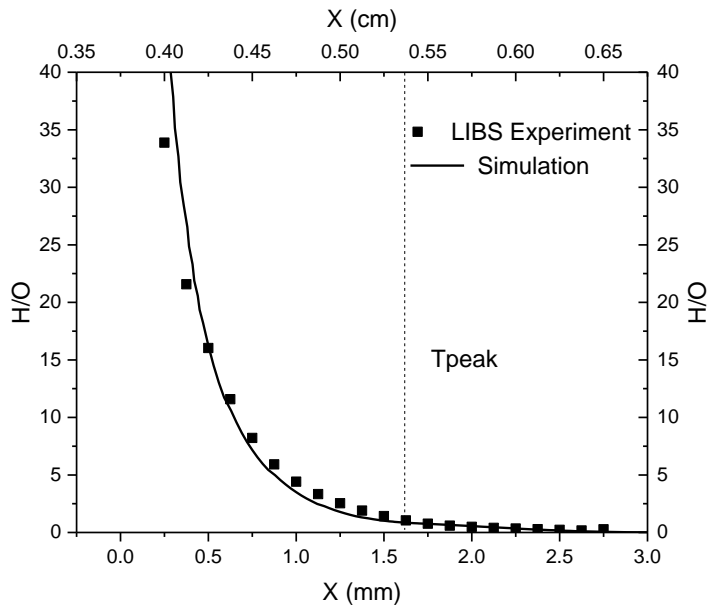
Figure 3.14. A comparison between the H/O ratio obtained from the LIBS measurement to that obtained by simulation.

Since the N/O atomic ratio for air is known, N/O can be calibrated by normalizing the local emitted line intensity ratios to that of air. The atomic ratio distribution of C/H is worth noting because the mobility of H-containing molecular species is much higher than that of the C-containing species in the flame [50]. In other words, there is preferential diffusion of H in this flame. Since LIBS measures atomic ratios directly it can be used to observe preferential diffusion of H relative to C. In Fig. 3.15 the C/H ratio is plotting across the flame and it can be seen that the numerical and experimental results both indicate that the C/H ratio is 0.5 and constant near the fuel boundary. This is true because ethylene has not yet begun to decompose and thus the hydrogen and carbon atoms are bonded in ethylene. As the flame is approached, a near 10% rise is observed in the C/H ratio and this can be explained by the preferential diffusion of the light hydrogen containing species (e.g., H_2) towards the flame, thus depleting H relative to C. The light hydrogen containing species are more mobile and are transported towards the oxidizer zone faster than the carbon containing species, resulting in a moderate increase in C/H ratio. After this peak, the C/H ratio drops significantly due to the fact that the light hydrogen containing species have diffused rapidly into the oxidizer side while the less-mobile carbon containing species have diffused to a lesser degree. The ability for LIBS to readily produce this characteristic curve for C/H atomic ratio in diffusion flames is a testament to the value of the LIBS measurement in diffusion flames.
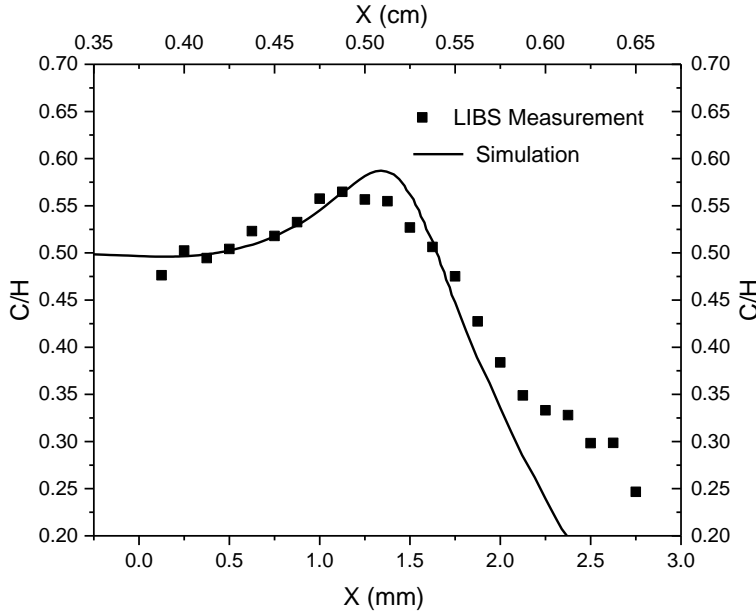
Figure 3.15. A comparison between the C/H ratio obtained from the LIBS measurement to that obtained by simulation.

With the relative ratios between C, H, N and O being measured by LIBS, the elemental mass fractions can be calculated from the experimental measured atomic ratios C/O, H/O and N/O using the following procedure.

Using C as an example, the local atomic fraction for carbon atoms X_c can be derived by

$$X_c = \frac{C/O}{C/O + H/O + N/O + 1} \qquad (3.1)$$

Thus, the elemental mass fraction for C can be expressed as

$$Y_c = \frac{w_c * X_c}{w_c * X_c + w_H * X_H + w_N * X_N + w_O * X_O} \qquad (3.2)$$

where Y is the elemental mass fraction, X is the atomic fraction and w is the atomic weight for annotated element, respectively. The distributions of the elemental mass fractions obtained from

41

the LIBS measurements are shown in Fig. 3.16. The mixture fraction can be calculated from the elemental mass fractions and a comparison between the LIBS-measured mixture fractions and that from the numerical study is shown in Fig. 3.17. Good agreement is obtained, demonstrating the capability of the LIBS technique in diffusion flames, not only as a tool for measuring atomic ratios, but also as a measurement method for mixture fraction.
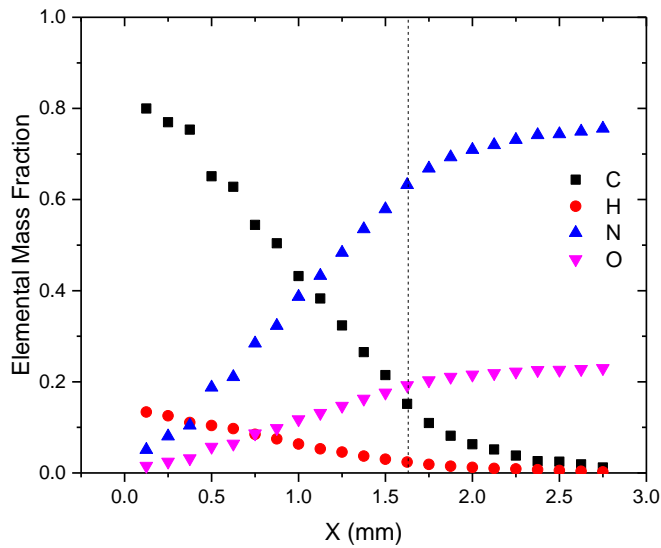
Figure 3.16. The distributions of elemental mass fraction for C, H, N and O calculated from atomic ratios.
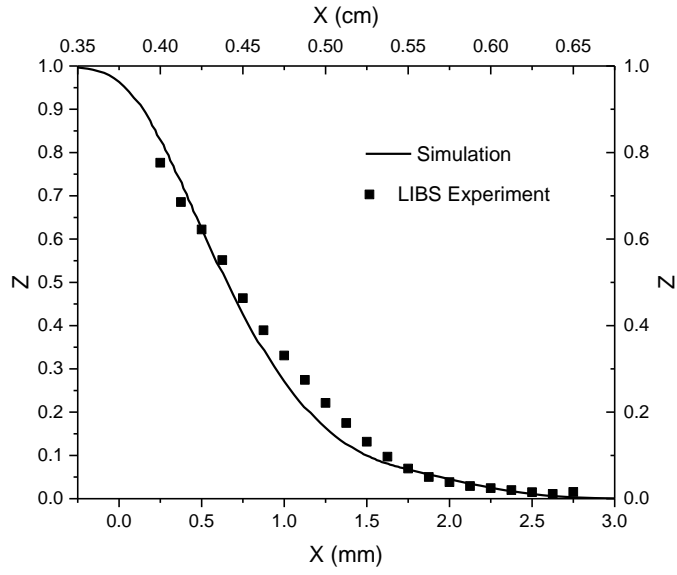
Figure 3.17. A comparison between mixture fraction obtained from the LIBS measurement to that obtained by simulation.

3.4. Summary

In this chapter, an approach to measuring atomic ratios and mixture fraction by utilizing laser induced breakdown spectroscopy (LIBS) was introduced. A back-scattering setup was proposed to mitigate the effect of beam steering and a RG-665 Schott filter was used to increase the dynamic range of the LIBS measurement. The atomic ratios for C, N. H and O (e.g., C/O, H/O and C/H) for the LIBS system were first calibrated in an ethylene-air premixed flat flame. Along the centerline of a counter-flow diffusion flame, the atomic ratio distributions were measured with a spatial resolution of 125 µm to demonstrate the capability of LIBS to measure atomic ratios between different elements from the fuel side to the oxidizer side of a hydrocarbon diffusion flame. Good signal strength was observed from 0.03 < C/O <15 and excellent agreement was found between experimental and numerical results. Moreover, measurements of the C/H atomic ratio distribution were used to provide insights into preferential diffusion of H relative to C, further illustrating the utility of LIBS. Finally, the mixture fraction distribution was calculated from measured atomic ratios. The results of this work demonstrate that the LIBS technique holds promise as a simple tool for measuring atomic ratios and mixture fraction in diffusion flames. LIBS can also operate for a wide range of fuels and compositions because the signal is strong and does not suffer from the interferences that plague Raman measurements in hydrocarbon flames.

Chapter 4: <u>Acoustic aided laser-induced breakdown thermometry</u>

As introduced in previous chapter, LIBS provides a convenient and economical way to measure elemental composition in a broader range of combustion systems compared to other techniques. In addition to composition measurement, temperature measurement is another essential task in fundamental flame studies. It is always of great interest that the temperature could be measured simultaneously with the composition without adding much complexity to the diagnostic system. Several existing optical methods provide such benefits over LIBS in this regard; however, not without their own limitations. For example, absorption spectroscopy only offers line-of-sight measurement, laser-induced fluorescence (LIF) requires a tunable laser and suffers from quenching effects. Rayleigh scattering and Raman scattering measures the density of non-reactive species and inferring temperature under the assumption of the ideal gas law and constant pressure. However, due to their low scattering cross sections, the collected signal is small, making it challenging to extract accurate data without long integration times. Coherent anti-Stokes Raman（CARS）has advantages in terms of signal strength, but is even more complicated experimentally. Thus, even with the enormous amount of efforts that have been devoted to simultaneous flame temperature and composition measurement, a simple laser-based method that can be applied on a broad range of systems is still desirable, especially when high spatial and temporal resolution is preferred.

In this chapter, the acoustic emission from the laser induced breakdown will be explored. Previously employed as an internal standard to normalize the shot-to-shot variation in the solid state LIBS research, the acoustic emission from the in-flame laser induced breakdown will be

first studied with varying laser energy output in a premixed flame with fixed equivalence ratio. The correlation between the optical emission and acoustic emission will be confirmed to demonstrate the acoustic signal can still serve an internal standard in the gas phase LIBS measurement. Then the influence from the flame temperature and the composition to the acoustic signal will be separated from each other and investigated systematically to explore the potential of utilizing the acoustic signal for future flame temperature measurement. The acoustic aided laser-induced breakdown thermometry (LIBT) will be proposed in this chapter. The calibration profile for LIBT will be established on a McKenna flat flame burner with thermocouple measured temperature. The statistics of the LIBT measurement will be analyzed to better understand this technique. Finally, the temperature distribution in a counter-flow diffusion flame will be measured and compared with the temperature profile obtained in the simulation.

4.1. Experimental Setup

4.1.1. Acoustic system setup

The LIBT system as shown in Fig. 4.1 is constructed based on the existing LIBS system in LACER lab. The system includes a pulsed Nd:YAG laser (Continuum Surelite SL I-10) with a repetition rate of 10 Hz. The laser has a beam diameter of 6 mm, a pulse width of 4-6 ns and a beam divergence of 0.5 mrad. In order to minimize shot-to-shot variations, the pulse energy was also fixed at 180 mJ to achieve saturation. The second harmonic, 532 nm, is focused with a convex lens with a 100 mm focal length.

To collect the acoustic signal from the laser induced breakdown, a Shure Beta 87A microphone was placed 30cm from the focus spot. A 24V phantom power (Phantom II pro) drives the microphone and also feeds the signal recorded by the microphone to an oscilloscope (Tektronix

2225). The oscilloscope (Tektronix 2225) was synchronized with the flash lamp of the Nd:YAG

laser along with the spectrometer used in the optical signal collection. The waveform collected in

the oscilloscope was recorded on the PC end with NI-VISA interface.
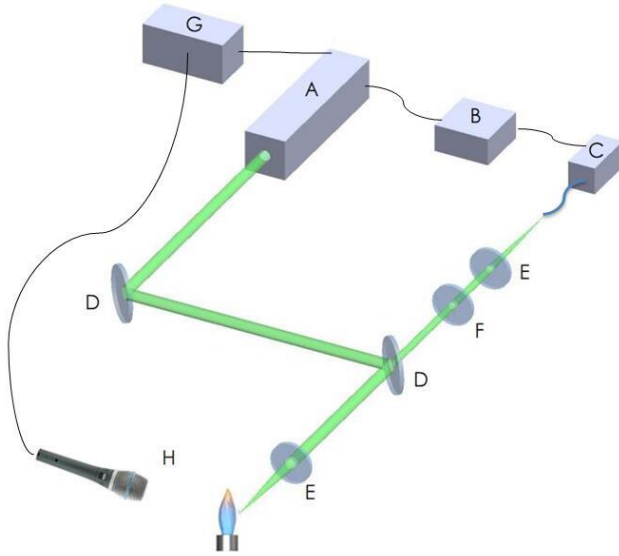
Figure 4.1 Schematic of LIBT setup. A: Laser B: Synchronizer C: Spectrometer D: Dichroic
mirror E: Lens F: Filter G: Oscilloscope H: Microphone.

4.1.2. Thermocouple and burner setup

The reference temperature was measured a type-B fine wire thermocouple. The McKenna flat-

flame burner and the counter-flow diffusion flame burner used in the following studies are the

same as described in the previous chapter. The counter-flow diffusion flame was also modeled

using OPPDIF flame code as the previous chapter.

4.2. The correlation between acoustic and optical signal.

The acoustic signal has already been applied in solid-state LIBS measurement as an internal standard to normalize the pulse-to-pulse variation resulted from the matrix effect and the laser power fluctuation [55-57]. However, to the best of the authors' knowledge, such applications have not yet been adapted to LIBS measurement in the gas phase. To find out whether the acoustic signal can still serve an internal standard in the gas phase, the LIBS measurement with simultaneous acoustic recording was first performed in air. As described previously, for the elemental composition measurement, the nitrogen and oxygen peak emission were integrated over a region of 6.5 nm and 4 nm centered at 744.5nm and 777.7nm, respectively; in correspondence to their atomic emission lines. The carbon peak emission is integrated over a region of 1.6 nm centered at 711 nm. The intensity of Hα peak was integrated over a region of 4 nm centered at 656.28 nm. A total of 100 samples were collected with varying laser energy. The relationship between the atomic peak emissions and the acoustic signals in air are shown Fig. 4.2 and Fig. 4.3. An excellent correlation coefficient of 0.99 can be established between the H atomic peak emission and the acoustic. For O atomic peak emission, similar results can also be concluded with a correlation coefficient of 0.98. Thus, in the non-reacting gas phase like the atmosphere, the acoustic signal is still a good indicator of plasma strength and can be utilized to normalize the shot-to-shot fluctuations in the LIBS signal. Furthermore, to find out if such correlation is still applicable in the flame, a total of 500 of samples were collected in an ethylene-air flame (Φ=0.85) with varying laser energy. In Fig. 4.4-4.6, a reasonable correlation coefficient of 0.94, 0.95, and 0.95 is achieved with C, O, H atomic emission peaks. The atomic emission and the acoustic signal are still correlated, though to a lesser degree compared with the case in air. The residuals of the regression line (defined as actual value minus predicted value) in the air are

within $\pm 5\%$ of the predicted value. There are much more deviations from the regression line in the flame measurement. The residuals can be up to ± 10 % of the predicted value. Such differences in residual value suggests that other than the fluctuation of laser power which shared by the air and flame experiment, other factors in the flame measurement contributes significantly to the randomness of acoustic signals. Similar to the solid state LIBS experiment, many factors, namely defocusing caused by the flame front, gas flow, reaction, presence of particles, can all contribute to this uncertainty. Unfortunately, it is almost an impossible task to separate these factors and quantify the influence of each by its own. Thus, when utilizing the acoustic signal to normalize the shot-to-shot fluctuations in the flame, the intrinsic uncertainty associated with this approach should be well recognized by the experimenter. The atomic ratios based mixture fraction measurement described in the previous chapter has a RSD of 3% in the premixed flame and a RSD of 6% in the counter-flow diffusion flame due to the robustness resulted from the relative amount measurement. The acoustic aided measurement can yield very limited benefits in this perspective. In contrast, the absolute amount measurements for elemental species have large shot-to-shot fluctuations up to $\pm 30\%$ in the flame, thus can be benefited from this approach significantly in future studies.

$R^2=0.99$
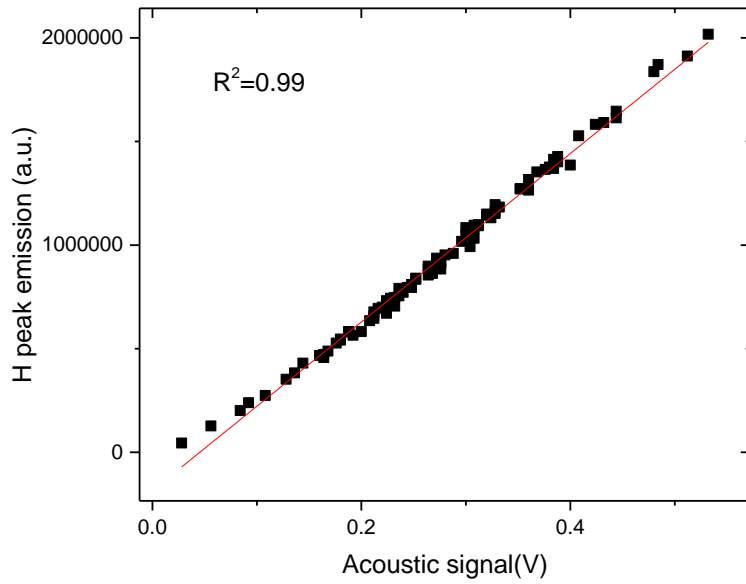
Figure 4.2 The correlation between H atomic peak emission and the acoustic signal from laser induced plasma in the air.

$R^2=0.98$
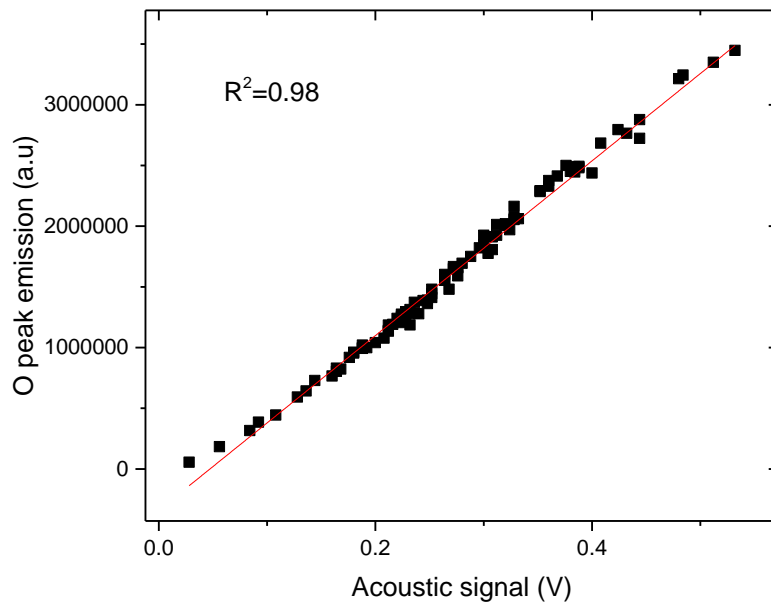
Figure 4.3 The correlation between O atomic peak emission and the acoustic signal from laser induced plasma in the air.
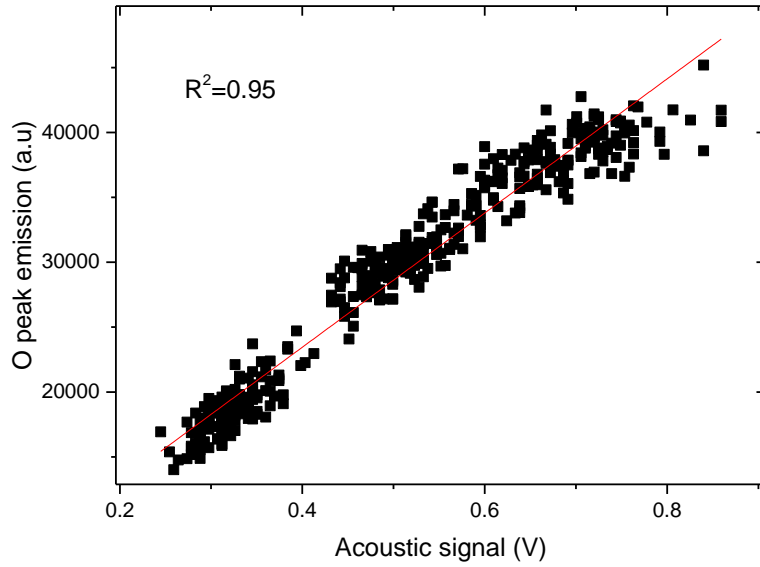
Figure 4.4 The correlation between O atomic peak emission and the acoustic signal from laser induced plasma in the fuel lean flame.
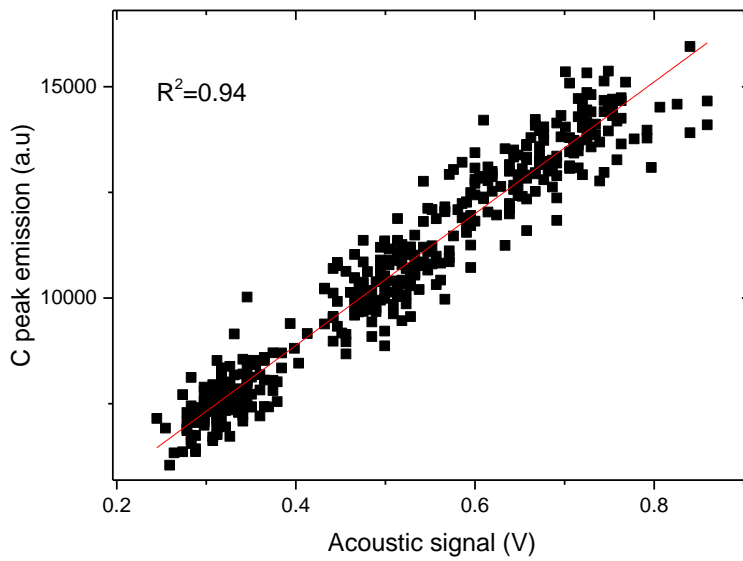
Figure 4.5 The correlation between C atomic peak emission and the acoustic signal from laser induced plasma in the fuel-lean flame.
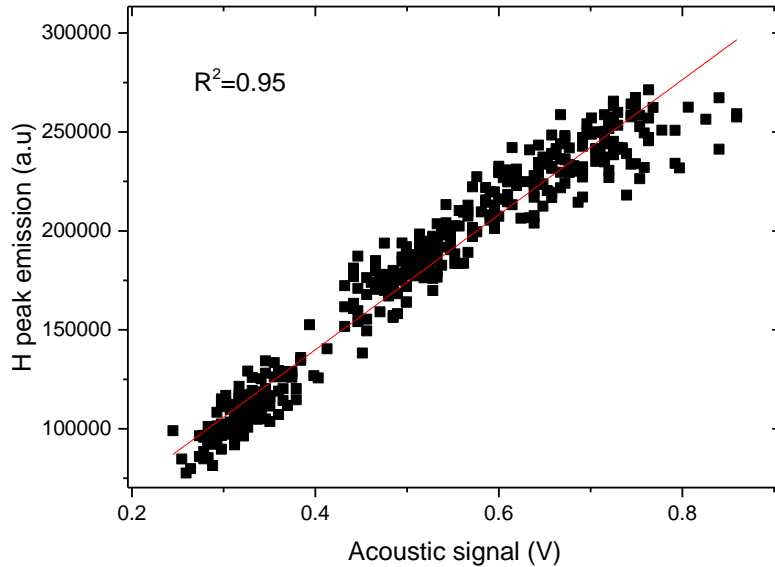
Figure 4.6 The correlation between H atomic peak emission and the acoustic signal from laser induced plasma in the fuel-lean flame.

4.3. The temperature effect on acoustic emission

To the best of author's knowledge, the acoustic signal from laser induced breakdown has not

been utilized in inferring the flame temperature. However, thanks to previous research on

employing the laser-induced plasma as a sound source to simulate a blast wave or a sonic boom

in the laboratory [58-60], the amplitude of the acoustic shock wave can be correlated to the gas

density of the focal region when the laser energy and detection distance remain constant.

Assuming the ideal gas law, such a relationship has a potential to be further utilized to infer the

local gas temperature. As the first step to validate the LIBT concept, the relationship between

the acoustic signal and the local temperature is explored in the following study. The LIBT

experiment was performed on a McKenna burner. The laser was focused on a spot right above

the center of burner head in order to reduce the influence of atmosphere air. To avoid the influence of composition, the total flow rate was varied to yield different flame temperatures while holding the equivalence ratio constant at stoichiometric ($\Phi = 1$). A total of 140 samples were collected at each of 8 different temperatures.

The randomness in optical signals from laser induced plasmas has been widely observed [68, 69]. Our studies in previous section also suggested that in-flame measurement contributes to the randomness in the acoustic signals; thus, the acoustic signal from laser induced breakdown can be prone to the same random nature as the optical signal. Moreover, a study by Michel *et al.* [70] pointed out that the normal distribution is not a good representative of the random LIBS signal compared with the extreme value distribution, even no extreme nature was exhibited by the laser pulse energy fluctuations. Thus, a closer examination should be taken carefully at the distribution of acoustic signal before averaging the samples to reduce any unnecessary error contributed by extreme values. The histograms of acoustic signals are shown in Fig. 4.7. The extreme large values can be observed in almost every temperature; even though they only constitute only a small part of total samples. The positive skewness of samples listed in Table. 4.1 suggests that the distribution is departed from normal due to long tails. In our experimental observation, when dust or other particles were occasionally presented in the focal spot, an extremely strong crack sound can be clearly distinguished from regular cracking sound. The extreme large value generated due to the presence of particles will not share identified distributions with other samples and the underlying assumption of the central limit theorem could not be sufficed. Thus, the sample mean observed in the experiment is no longer a good estimator of the gas phase population mean unless the extreme values are excluded from further data evaluation. When the sample size is large, the effect from such bias would not be

53

pronounced; however, when higher temporal resolution is desired, the extreme value should be paid attention to. A simple signal screening was applied to exclude the outliner larger than twice of the standard deviation from the sample mean. As shown in Table. 4.1, an average 4.6 extreme values were taken out from each temperature under this screening, which is 3.3% of all 140 samples. However, the skewness of data has been reduced significantly. For example, in a flame temperature of 1506K, the skewness dropped dramatically from 0.89 to 0.03. The standard deviation also decreased by 13% on average. The histogram of acoustic signals after the screening shown in Fig. 4.8 confirmed that even the screening criteria was two-sided, most of extreme values are on the large end, which is consistent with our experimental observation. After the screening, the reduced skewness and excess kurtosis suggested that the normal distribution can be a reasonable estimation of the remaining data. The sample mean can be used to represent the population mean after the screening.

Table 4.1 The statistics for McKenna burner measurement.

T(K)	Skewness before screening	Skewness after screening	Number of deleted points
1395	0.1783	0.133906	8
1421	0.26071	0.074858	3
1452	0.50417	0.176583	3
1480	0.57046	0.282227	4
1506	0.89089	0.028536	4
1516	0.44464	0.161533	4
1539	0.48247	-0.06676	5
1563	0.27366	0.131667	6
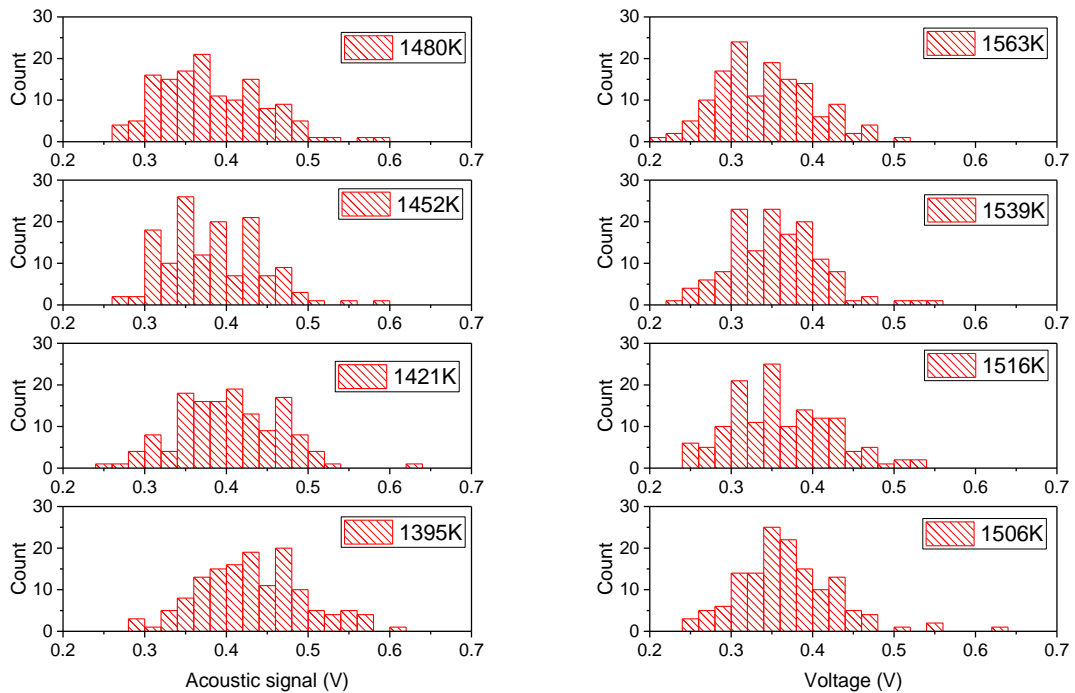
Figure 4.7. Histogram of acoustic signal on the McKenna burner for the same equivalence ratio and varied temperature.
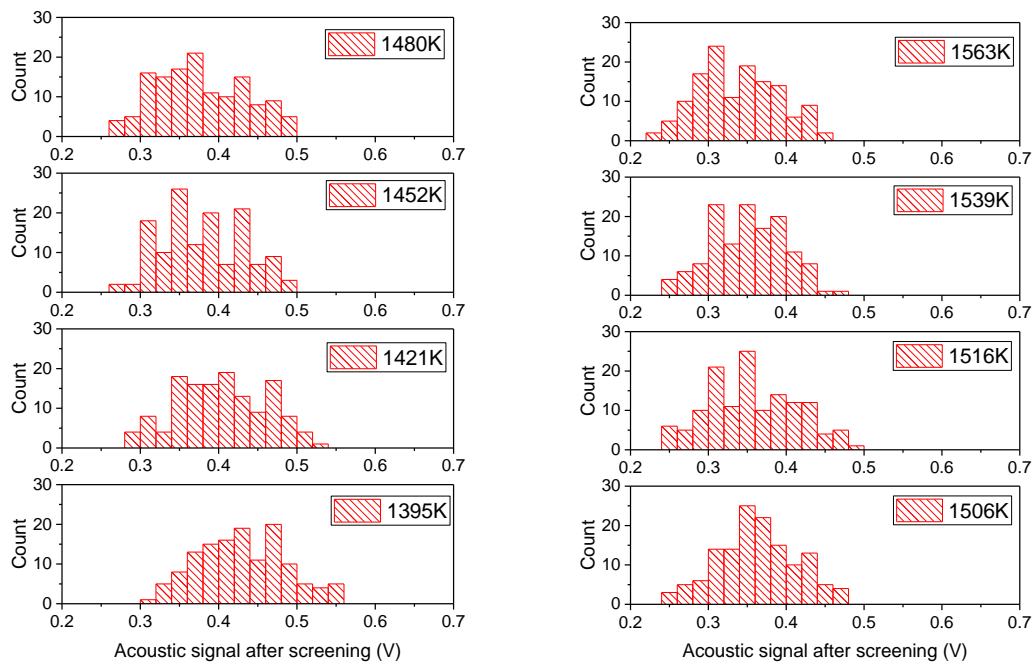
Figure 4.8. Histogram of acoustic signal on the McKenna burner for the same equivalence ratio and varied temperature.
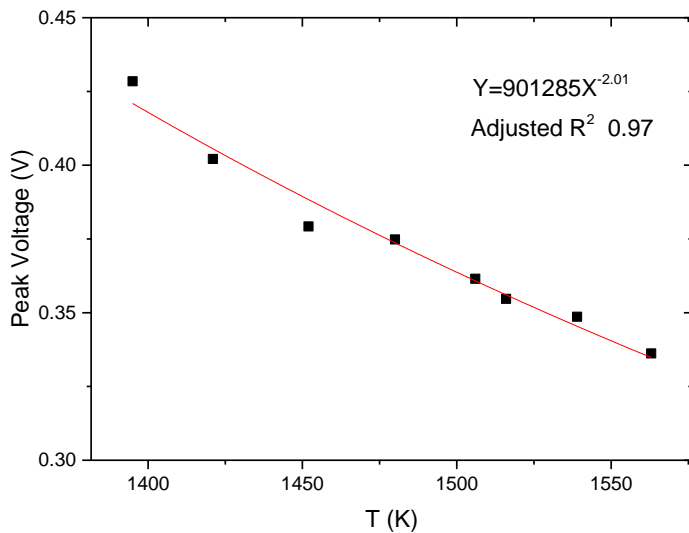
Figure 4.9. The correlation between acoustic signal and thermocouple-measured temperature on a McKenna Burne
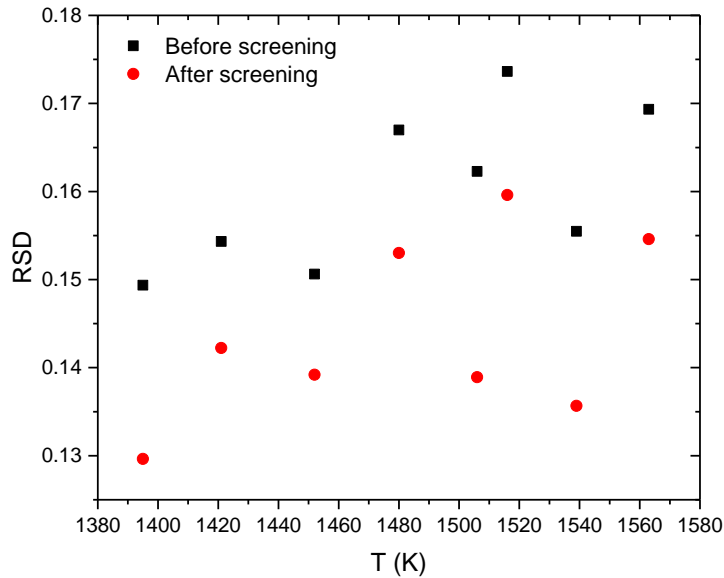
Figure 4.10 RSD (relative standard deviation) for acoustic signals on McKenna burner

The acoustic signals measured by LIBT were fitted with a power law to the radiation corrected temperatures measured by thermocouple with a coefficient of determination of 0.97 as demonstrated in Fig. 4.9. The relative standard deviation(RSD) is used in this study to characterize the shot-to-shot variation of the LIBT signal. In Fig. 4.10, general reduction of 2% in RSD can be achieved by deletion of extreme value, yielding an average RSD of 15%. The 95% CI (confidence interval) can be constructed using RSD value to represent the accuracy of LIBT measurement, which will be discussed the later part of this study. In this specific experiment, temperature differences as low as 20K can be discerned by the measured acoustic signals.

4.4. The compositional effect on acoustic emission

The proposed LIBT technique utilized the correlation between the amplitude of the acoustic shock wave and the gas density of the focal region under the assumption of ideal gas law. In previous literature, the composition was reported to be a weaker factor influencing the laser-induced breakdown threshold compared to the flame temperature [54]. For example, a temperature increase of 1500 K increases the breakdown threshold by 30 mJ while a change in equivalence ratio from 0 to 2 varies the breakdown threshold by less than 2 mJ. To study the compositional effect, the LIBT experiment was performed on a McKenna burner with varying equivalence ratios while the temperature was kept at a constant. Under different equivalence ratios from 0.6 to 1.7, the total flow rate was varied to yield a fixed temperature of 1406 K (with a variation of $\pm$8K). A total of 140 samples were collected at each of 12 equivalence ratios. The recorded acoustic signals were plotted along with the thermocouple measured flame temperature on the equivalence space in Fig. 4.11. The acoustic signals from the laser induced plasma demonstrated a low sensitivity to the change in equivalence ratios. To better interpret this result, the deviations of acoustic signals from their mean value were demonstrated in Fig. 4.12 in relative terms. A fluctuation of up to $\pm$10% can be observed in this range of equivalence ratios. In comparison, the influence from the temperature is much more pronounced. A temperature decrease of 168K (10%) led to a 30% increase in the acoustic signal as shown in Fig. 4.9. Thus, the composition is a second order factor on acoustic signal comparing to the temperature.
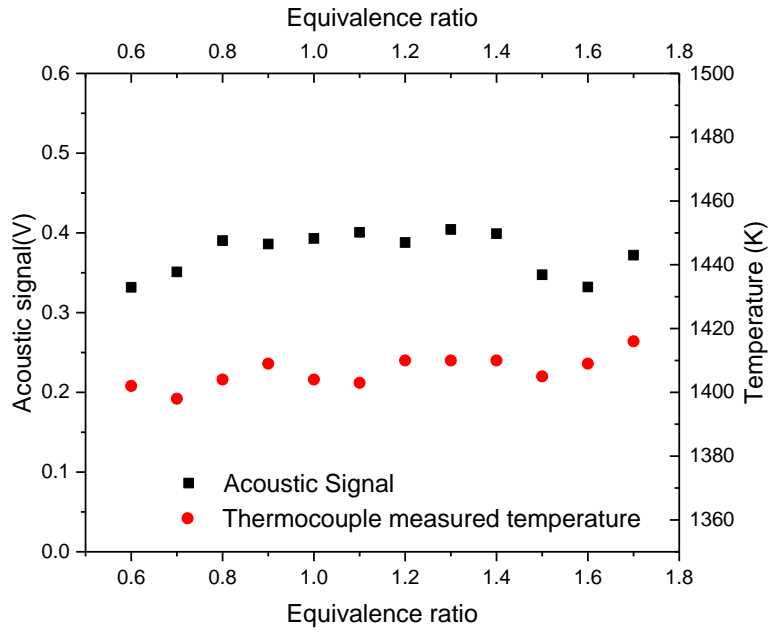
Figure 4.11 The acoustic signals and thermocouple measured flame temperature corresponding to varying equivalence ratios on the McKenna burner.
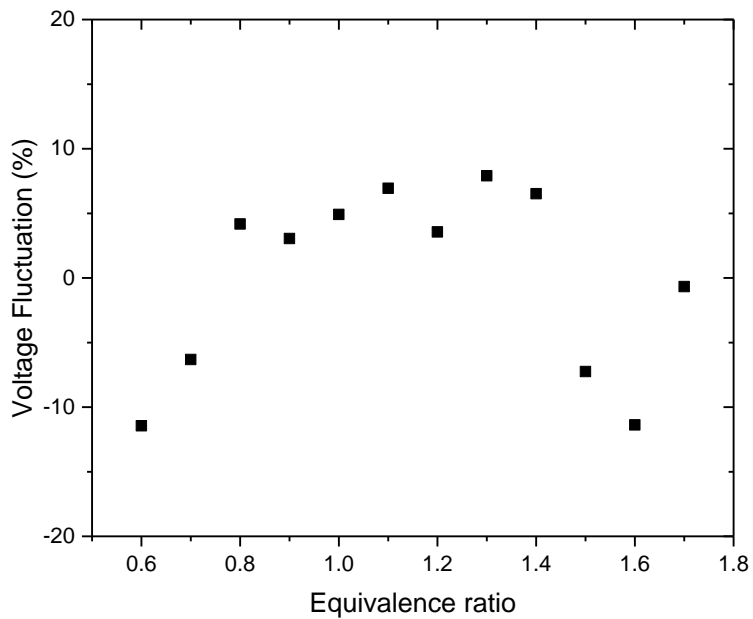
Figure 4.12 The deviations of acoustic signals from their mean value in equivalence ratio space

4.5. Temperature measurement using LIBT

Measurements were further conducted along the centerline of a counter-flow flame. To benchmark the temperature measured with LIBT, the simulation was performed using OPPDIF with a strain rate at 140/s, matching the PDPA measured strain rate (Fig. 4.13). Considering the possibility of subtle differences in the exact flame location between the experiments and the simulations (due to fluid mechanical differences), the location of the peak temperature was used as a common point of reference to allow for a direct comparison of the temperature distributions. Because the acoustic signal is negatively correlated with temperature, the location of the temperature peak was determined by the lowest value of the acoustic signal. The measured acoustic signal profile and the temperature profile obtained in the simulation are shown in Fig. 4.14. Since the composition effect was found to be a second order factor compared to the temperature effect as discussed in the previous section, the composition effect was ignored in this measurement. Utilizing the calibration profile obtained with the McKenna burner (Fig.4.9), the temperature distribution of the counter-flow diffusion flame can be inferred. In Fig. 4.15, both the temperature profiles before and after the screening were plotted along with the simulation results. The difference between the before and after screening results are small but noticeable. The deviation from the simulation profile was 20 to 30K less for the after screening results. In the temperature range from 1400K to 1800K, the measured temperatures are consistently 20-50K lower than the simulation value; while in the high temperature region, from 1800K to 2100K, the measured temperatures are 20-50K higher than the numerical results. Such difference can be attributed to several factors. Firstly, the temperature range used for calibration on the McKenna burner is narrower than that of the counter-flow flame. Secondly, due to the sooting limit of the ethylene-air flame ($\Phi_c = 1.74$), the effects of compositional difference can

only be evaluated in the range of 0.6 to 1.7. While in the counter-flow diffusion flame, the local equivalence ratios can be dramatically different throughout the flame. In Fig. 4.16, the investigated composition range was plotted in the mixture fraction space along with LIBT measured temperature. The calibration for the compositional effects which was carried on a premixed flame was unable to be extended outside the red dashed line in the fuel rich side. Thus, the calibration covers a good portion of the high temperature zone but excluding the region where mixtures were more extreme. Nevertheless, the LIBT measured temperature profiles compared well with the results obtained in simulation.

Since the correlation between the acoustic signal and temperature are easier to be established than that between the acoustic signal and density, even though the LIBT measurement is based on the correlation between the gas density and the acoustic signal but not vice versa, the acoustic signal can sometimes be used to infer the gas density. The molecular weight of ethylene is 28g/mol which is similar to that of air. Assuming a constant average molecular weight of 29g/mol and atmosphere pressure, the density distribution of mixture can also be obtained under the assumption of ideal gas law as shown in Fig.4.17. However, extra caution should be paid when measuring the temperature and gas density in systems where the molecular weight of fuel is dramatically different from that of air. The molecular weight in each location will be very different and this influence will be coupled into the correlation between the flame temperature and the acoustic signal. The molecular weight difference should be first quantified by the LIBS measured composition. Only after the correction in molecular weight differences, the desired correlation between the acoustic signal and the temperature can be constructed.
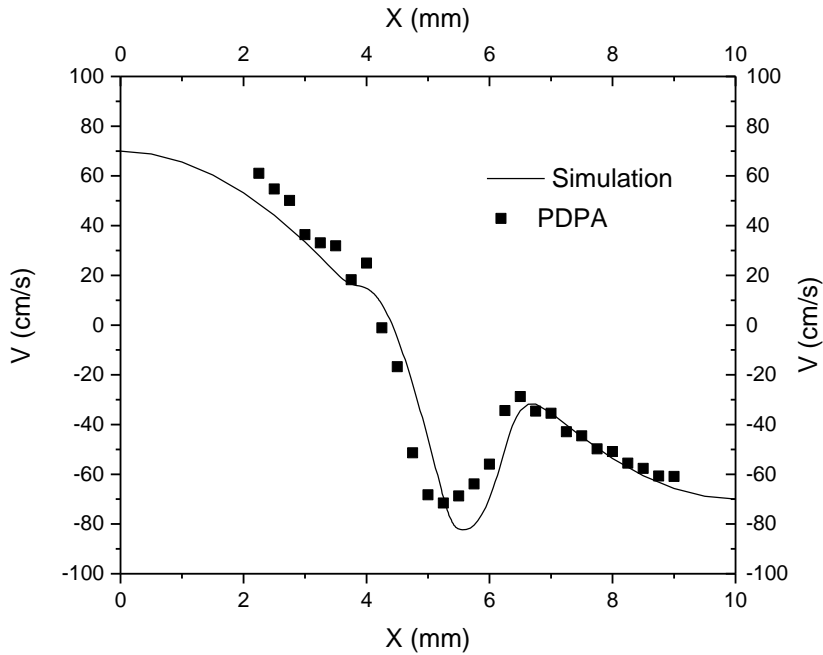
Figure 4.13 The comparison between PDPA measured and OPPDIF simulated flow velocity profile.
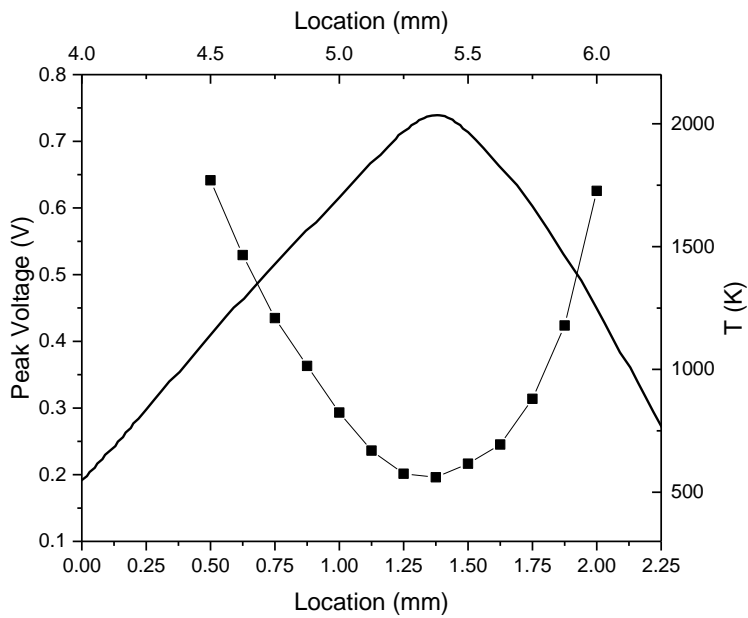
Figure 4.14 The comparison between measured acoustic signal profile and the temperature profile obtained by OPPDIF simulation
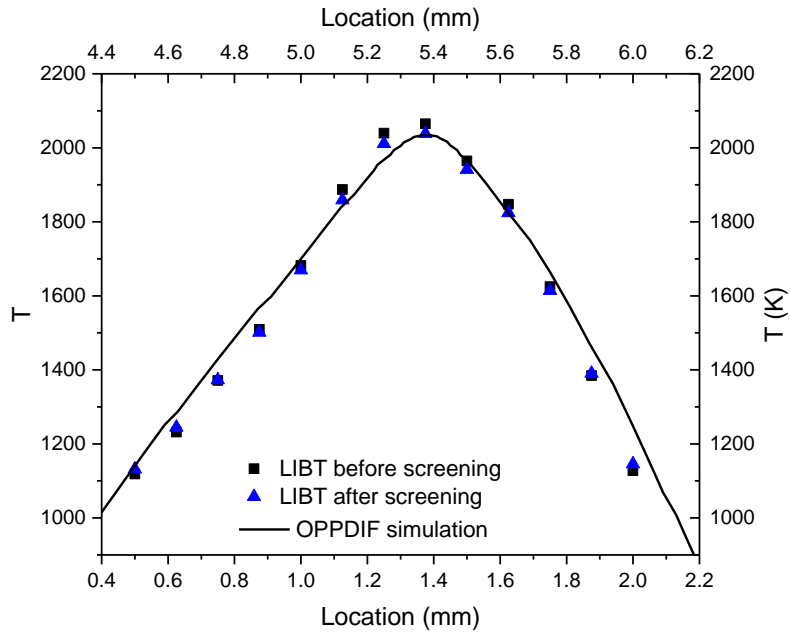
Figure 4.15 The comparison between LIBT measured and OPPDIF simulated temperature profile in the counter-flow diffusion flame.
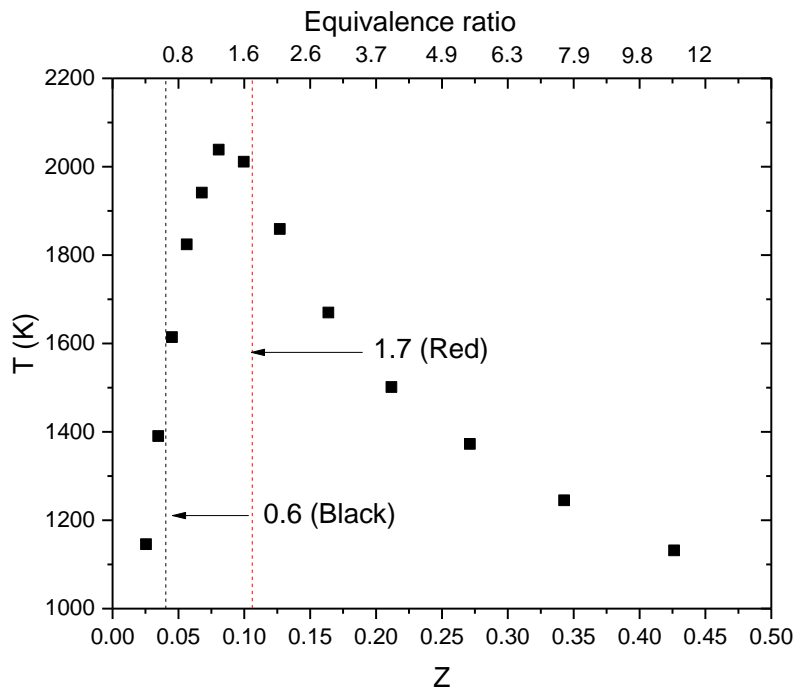
Figure 4.16 An illustration of the calibrated region of compositional effect (from 0.6 to 1.7) in the counter-flow diffusion flame.
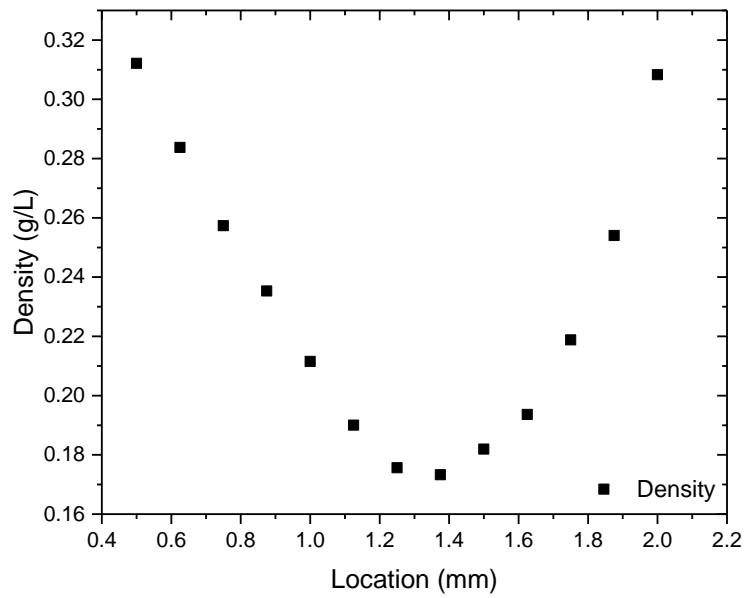
Figure 4.17 The distribution of mixture density in the counter-flow flame

4.6. Summary

In this chapter, the acoustic emissions from the laser induced breakdown were first measured in the air and a premixed ethylene-air flame. A good correlation between the atomic peak emission and the acoustic signal confirmed that acoustic signal is still a valuable method to correct the shot-to-shot fluctuations in the gas phase and in the flame, especially when absolute amount measurement is concerned. The influences from the flame temperature and the composition to the acoustic signal were later investigated on a McKenna burner. The influences from the flame temperature and the composition to the acoustic signal were investigated independent of each other. The composition effect was found to be a second order factor comparing to the temperature effect. A novel approach to measure local temperature by laser induced breakdown thermometry (LIBT) was proposed. The distribution of acoustic signal from laser induce breakdown were analyzed to mitigate the bias towards extreme values. A correlation between the acoustic signal and the thermocouple-measured temperature was established with an ethylene-fueled McKenna burner. This correlation also served as the calibration profile for further studies. The temperature distribution in a counter-flow diffusion flame was measured along the centerline with a spatial resolution of 125μm. The measured temperature distribution compared favorably with the numerical simulation obtained with OPPDIF under matching strain rates. The molecular density distribution of the mixture was also obtained under the assumption of the ideal gas law.

Chapter 5: Simultaneous temperature and composition measurement using laser plasma diagnosis and the preliminary study in turbulent flames

In previous chapters, the LIBS was introduced as an alternative method to obtain the mixture fraction based on its usefulness in elemental ratio measurement. The possibility of utilizing the acoustic signal from the laser induced breakdown to correct the shot-to-shot fluctuations has been explored, which shed a light on the measurement of absolute elemental species amount. The acoustic-based LIBT was also proposed as a novel method to measure the flame temperature. Thus, the laser induced breakdown based diagnostics already demonstrated its potential to measure the composition and temperature. In this chapter, the LIBS and LIBT will be combined to investigate the possibility of simultaneous composition and temperature measurement in flames.

It is worth paying attention to that for a simultaneous composition and temperature measurement in the real world, the temporal and spatial resolutions of two measurements are preferred to be matched in order to exploit the potential of the combined system. As previously discussed, the LIBS technique excels other laser based diagnostic technique in a way that it can be applied in a much broader range of fuels and running conditions while being more convenient and economical. However, when simultaneous composition and temperature measurements are concerned, existing laser induced plasma diagnostics falls in short in this regard. The previous reported laser-induced breakdown flame thermometry reported [54] was based on the

measurement of breakdown threshold. In this approach, for a given location of interest, the laser pulse energy has to be varied until the occurring of breakdown events becomes statistically significant. Thus, to determine the exact breakdown threshold, the statistics at each energy level is required. The corrected LIBS temperatures show excellent agreement with those obtained by CARS while the elemental composition for the mixture was obtained in the same experiment. Successful it is, this technique is short of a simultaneous composition and temperature measurement because the temporal resolution for the temperature measurement is significantly lower than that of the compositional measurement; which, requires an averaging of multiple shots ranging from 30 to 200 in general. To address this concern, in this chapter, not only the composition and temperature in the flame will be measured, the spatial and temporal resolution of the laser plasma diagnostics will be evaluated to determine its capability in simultaneous measurement. In the last part of this chapter, the application in the turbulent system, which places the highest requirement in the temporal resolution, will be studied preliminary.

5.1. Experimental Setup

5.1.1. Laser plasma diagnostic setup

The optical and acoustic setup are the same as described in Chapter 3 and Chapter. 4. The schematic of the system was shown in Fig. 4.1 with the spectrometer and the oscilloscope both synchronized to the laser flash lamp. The same three-bead type-B thermocouple as described in Chapter. 4 will be used in the following study.

5.1.2. Burner setup

For the premixed flame and counter-flow diffusion flame studies, the same McKenna burner and counter-flow burner as described in Chapter 3 are used in this chapter. An up-fired flat flame Hencken burner was used for the turbulent experiments. The Ø80 mm flat flame is composed of 570 non-premixed flamelets at the outlet of hypodermic tubes with 1.2 mm ID. Fuel and oxidizer gases are introduced in separate chambers isolated by a gasket. The fuel flows through the hypodermic tubes and the oxidizer flows through the empty holes of a stainless steel honeycomb core that fixes the position of tubes and ensures uniform flow of the oxidizer. A central tube with a 2 mm ID passes through the burner for coal feeding. Methane (CH_4) is used as the fuel, and a mixture of oxygen (O_2) and nitrogen (N_2) as the oxidizer. The post-flame temperature and gas composition can be well controlled over a large range by adjusting the flow rates of the reactant gases.

5.2. The spatial resolution and temporal resolution of laser plasma diagnostics

The spatial resolution of the laser plasma diagnostics is determined by the size of the plasma, which can be calculated from the known characteristics of the laser. The Nd:YAG laser (Continuum Surelite SL I-10) has a beam diameter of 6 mm with a 0.5 mrad beam divergence. The second harmonic, 532 nm, is focused with a convex lens with a 100 mm focal length. The beam divergence can be related to M^2 value by Eq. 5.1. M^2 is the Beam Propagation Ratio (BPR). The BPR is a value that indicates how close a laser is to being a single mode TEM00 beam, which in turn determines how small a beam waist can be focused. For the perfect Gaussian TEM$_{00}$ condition the M^2 equals 1.

$$\theta_0 = \frac{M^2 * 4\lambda}{\pi D_0} \qquad (5.1)$$

Where λ is the wavelength of the laser beam, D_0 is the beam diameter of the incident laser beam. For the optical setup in this study, the M^2 value equals 4.42. The ideal (minimum) focused spot diameter d_m will be enlarged by the M^2 factor. The ideal (minimum) focused spot diameter d_m and the actual focused spot diameter d_0 can be calculated by Eq. 5.2 and Eq. 5.3 respectively.

$$d_m = \frac{4\lambda f}{\pi D_0} \qquad (5.2)$$

$$d_0 = d_m * M^2 \qquad (5.3)$$

The calculation gives out a d_m value of 11.29 μm. The actual focused spot diameter $d_0 = 50$ μm represents the spatial resolution in our experiment. In the counter-flow diffusion flame

69

experiment, the spatial resolution was 125 µm which determined by the resolution of the translational stage. This estimation suggests that with an excellent spatial resolution of 50 µm for both LIBS and LIBT technique, they are capable for investigating even finer structure in the flame. It is also worth noticing that the size of the focal spot will be increasing proportionally with the focal length. Fortunately, when the longer focal length is required in a large scale flame, the requirement for the spatial resolution will likely to be relaxed at the same time. Moreover, the spatial resolution can also benefit from lower divergence lasers which are readily available commercially.

LIBS measurement in general requires a sample size between 30 to 200, due to its strong shot-to-shot variations. For a 10Hz laser, such requirement results in a temporal resolution from 3s to 20s. Much faster lasers are able to improve the spatial resolution dramatically. For example, recently commercially available lasers are able to produce a pulse output of 100mJ at 1000Hz. However, the temporal resolution of laser plasma technique is inherently restricted by the life time of plasma, which generally in a couple hundred microseconds. Thus, the sampling rate of LIBS technique has an upper limit in 1-3 kHz range. With a sample size of 30 per measurement, it is possible to achieve a temporal resolution of 0.01s in the composition measurement using LIBS.

Compared with well recognized temporal resolution of the composition measurement, the temporal resolution of the temperature measurement using acoustic aided LIBT has not been studied. To evaluate whether the temporal resolution of the temperature can match that of composition measurement, the investigation was performed from the statistics perspective. In Fig. 4.10 and Fig. 5.1, the relative standard deviation (RSD) for the LIBT samples ranged from 10% to 15% in both flat flame and counter-flow diffusion flame after the extreme value

screening. Whereas in Fig. 3.9 and Fig. 3.11, the RSD for the atomic ratio measurements were around 1-4% for the H/O ratio measurement and 6-8% for the C/O ratio measurement. The difference observed is due to the robust nature of relative amount measurements compared with absolute amount measurement.
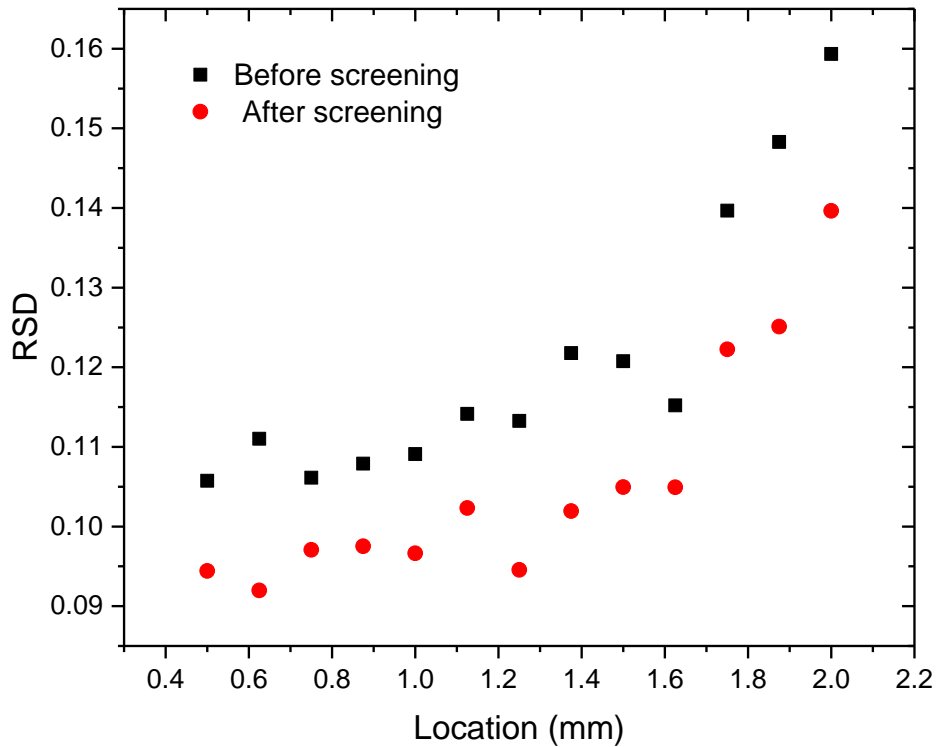
Figure 5.1 RSD (relative standard deviation) for acoustic signals on counter-flow burner

To better understand the temporal resolution of LIBT technique, the confidence interval of measured temperature was analyzed as a function of sample size. The average RSD is 14.4% in the flat flame (Fig. 4.10) and 10.5% in the counter-flow flame (Fig.5.1) after the extreme

screening, which is around twice of the RSD for atomic ratio measurements. The standard deviation S for the samples in one measurement can be expressed as

$$S = \text{RSD} * \overline{X} \qquad (5.4)$$

Where $\overline{X}$ is the sample mean. The CI (confidence interval) for the population mean in LIBT measurement can be constructed as following

$$0.95 \, CI(sample \, number > 30) = \overline{X} \pm z * RSD * \frac{\overline{X}}{\sqrt{n}} \qquad (5.5)$$

$$0.95 \, CI(sample \, number < 30) = \overline{X} \pm t * RSD * \frac{\overline{X}}{\sqrt{n}} \qquad (5.6)$$

where n is sample size, z stands for z score and t stands for t score for specific sample size and critical probability. Here, a critical probability of 0.95 was used which indicates that there is 95% chance for the population mean falling into the constructed confidence interval. Z=1.96 should be used when the sample size is larger than 30. For smaller sample sizes, t score with corresponding degree of freedom should be used instead. The confidence Intervals for the population mean in both relative and absolute terms are presented in Table. 5.1. The sample size can be determined as a function of demanded accuracy. When less accuracy is demanded, less samples are required. Thus, depending on the application, the accuracy of temperature measurement can be relaxed to yield better temporal resolution. For example, with a sample size of 30, the confidence interval is around $\pm5\%$ for the measured temperature. When the sample size is increased to 200, a very good accuracy of $\pm2\%$ can be achieved. Thus, the acoustic aided LIBT can go head to head with the LIBS measurement with matching temporal resolution; yielding an exceptional simultaneous temperature and composition measurement technique in flame diagnosis.

Table 5.1. The 0.95 confidence interval for LIBT measurement as a function of sample size in relative (%) and absolute (K) terms

Sample size	CI (% of temperature)	CI (K, in a 1500K flame)
1	29.4	441
10	9.297096	139.4564
20	6.57404	98.6106
30	5.367681	80.51522
50	4.157788	62.36682
100	2.94	44.1
200	2.078894	31.18341

5.3. The preliminary application in turbulent systems

The successful applications of LIBS and LIBT in the McKenna burner and the counter-flow burner demonstrated their practicality in a broader range of fuels and running conditions than existing techniques. However, the flat flame and counter-flow flame are both laminar flames. Universally presented in the industry, the turbulent flame places an extra degree of uncertainty on the diagnostics due to its transient nature and complexity in the structure. In this section, we would like to expand the laser plasma diagnostics further into the turbulent systems. A Hecken burner was used to produce different flame temperatures under the same equivalence ratio ($\phi = 0.83$). The flow speed for the post combustion gas is around 220cm/s for these experiments. The LIBT experiment was performed on the Hecken burner under 4 different temperatures. In Fig. 5.3, the histograms of acoustic signals were first examined to have an understanding of how the measurement in the turbulent flames is different from that in the laminar flames. The sample distribution in the turbulent flame seems to have much longer tails than that in the laminar flame (Fig 4.7), which suggested that the turbulent flame measurement has more randomness. Even though the RSD before the extreme screening is between 8%-12% (except the measurement under 1917K) as shown in in Fig. 5.4, the number of extremes (defined as those deviated more than two times of the standard deviation from the sample mean) is much larger than what we have observed in the laminar flame. On average, 50% of total points (60 out of 120) were classified as extremes (Fig.5.5) compared with only 3% in the laminar flame. Under a temperature of 1917K, the RSD was as much as 32% and 98 out 120 samples deviated more than 2 standard deviations from the sample mean. Such result was possibly contributed by the shortage in laser power to achieve a breakdown beyond the saturation for this temperature.

Because the distribution of samples is much more dispersed in turbulent systems, the normal distribution assumption is no longer appropriate to describe the measurement. It is difficult to quantity how much the temporal resolution was reduced in the turbulent flame compared to that in the laminar flame under a much flattened data distribution. Nevertheless, as shown in Fig. 5.6, the acoustic signals were still negatively correlated with the flame temperatures. It is still possible to evaluate the temperature quantitatively in the turbulent flames; however, since a methane fueled flame was utilized in this part of study, the calibration experiment has not been performed.
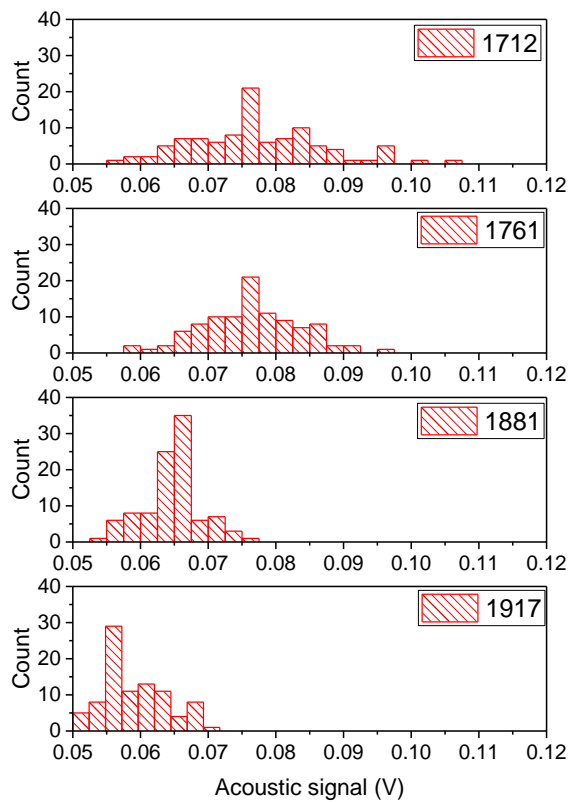
Figure 5.2 Histogram of acoustic signal on the Hecken burner under different temperature.
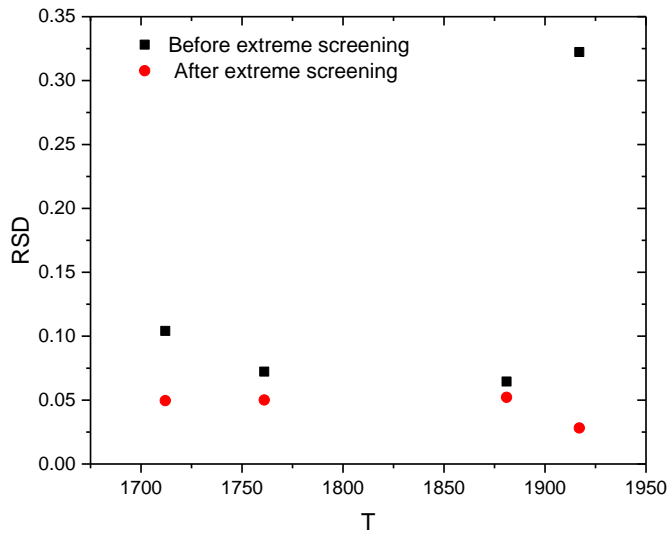
Figure 5.3 The acoustic signal versus the thermocouple measured temperature on the Hecken burner.
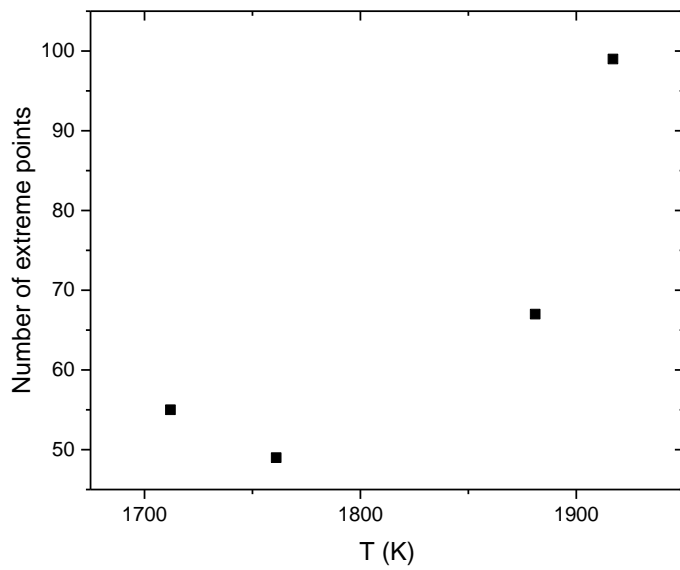
Figure 5.4 The number of extreme values out of 120 samples on the Hecken burner.
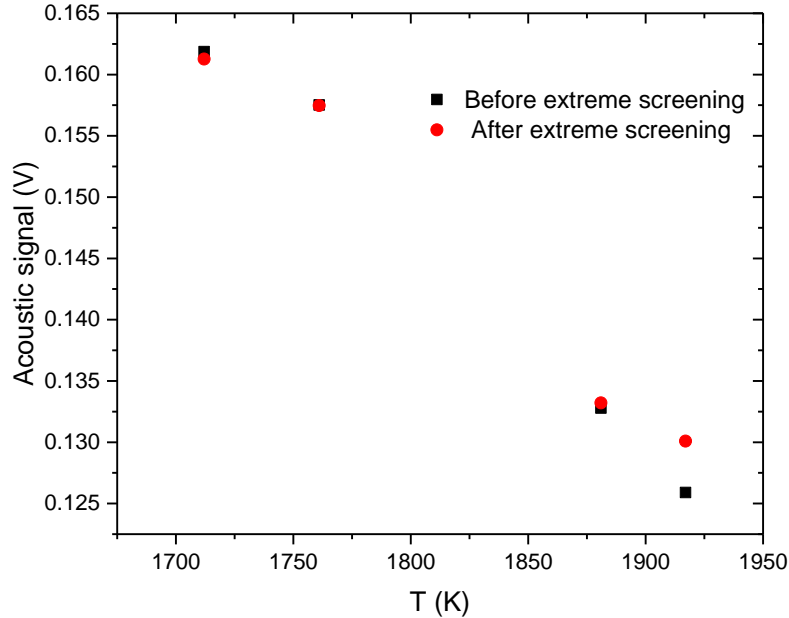
Figure 5.5 The acoustic signal versus the thermocouple measured temperature on Hecken burner

Moreover, to evaluate the influence of turbulent flame when it is presented in the light path instead of in the focal volume, an experiment was performed using a torch. The torch (MT 200, MegaTorch) was placed on the light path after the focal lens. The distance from the focal lens was 3mm and 6mm respectively (f=10mm). The turbulent torch was either waved by the experimenter to simulate a highly unsteady turbulent flame or placed stationary to simulate a stable turbulent flame. The histogram of the acoustic signal is shown in Fig. 5.7. Large shot-to-shot fluctuation can be observed when the unsteady flame was presented in the light path; while the steady turbulent flame was presented, a clearly centered distribution can still be observed with some extremes on the lower end. The further away the flame was placed from the focal lens (where the beam is more tightly focused), the more pronounced was the influence from the

turbulence. Such results suggested that when the turbulent flame was steady, it didn't interfere with the measurement to a large extent; while the unsteady flame had a significant impact on the acoustic signals. Thus, when further expanding the laser plasma diagnostics to large scale turbulent flames, not only the influence of turbulent flames in the focal volume (the creation of the plasma), but also its influence on the light path (defocusing) should be carefully evaluated
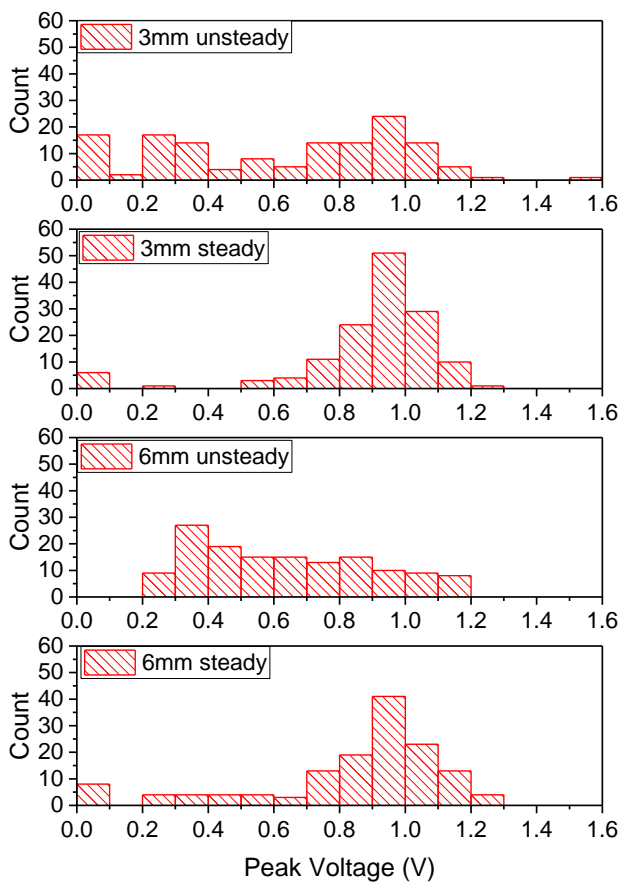
Figure 5.6 Histogram of acoustic signal in the air with a torch presented steady or unsteady in different locations along the light path.

5.4. Summary

In this chapter, to evaluate the potential of simultaneous composition and temperature measurement using laser plasma diagnostics, the spatial and temporal resolution of the LIBS and LIBT technique were evaluated. The calculation indicated that LIBS and LIBT share the same spatial resolution at 50 µm. The temporal resolution of LIBT technique was analyzed on the basis of statistics. The accuracy of the LIBT technique was interpreted as a function of sample size to shed a light on future applications where a higher temporal resolution might be preferred. The results suggested that LIBT can have a matching temporal resolution with LIBS, yielding an exceptional simultaneous temperature and composition measurement technique. Moreover, the temporal resolution of LIBT has a lot of room for improvement utilizing higher frequency laser. The simultaneous measurement was later performed on the counter-flow flame. The results compared favorably with the numerical results obtained through OPPDIF flame code.

Furthermore, the applications of laser plasma diagnostics on turbulent systems were investigated preliminarily. The LIBT experiment was performed on a methane-fueled Hecken burner. The statics of acoustic signals were examined to provide an understanding of the differences between the laminar and turbulent measurement. The turbulent measurement demonstrated much more shot-to-shot fluctuations compared to that in laminar flames. Such fluctuation can reduce the temporal resolution significantly, which unfortunately limits the future application in unsteady flames. However, in a steady turbulent flame, the temperature measurement is still feasible as demonstrated in the Hecken flame. Finally, to evaluate the influence of turbulent flame on the light path, an experiment using a torch was performed. The results suggested that the steady turbulent flame presented in the light path induced only a minor influence while the unsteady flame hugely impacted the shot-to-shot fluctuation. The further the flame was placed down the

light path, the more pronounced is such influence. Thus, not only the influence of turbulence on the focusing volume, but also that on the light path should be carefully evaluated when further adapting the laser plasma diagnostics to larger scale turbulent flames.

Chapter 6: Partial-equilibrium study-observation of water-gas-shift equilibrium in diffusion flames

Measuring mixture fraction from the elemental species perspective provides substantial benefits over traditional measurement technique from the molecular species perspective. The LIBS technique not only can be applied to a broader range of equivalence ratios, but also enables the measurement in higher hydrocarbon fueled flames. In a flame zone where the minor species concentrations are not negligible, LIBS technique is more accurate by encompassing all species instead of tracking only major species. It is also more intuitive to analyze the preferential diffusion effect using the elemental species profile. However, in exchange for such benefits, the information for the major species concentrations can no longer be directly measured by LIBS. To infer the molecular species profile from the elemental species profile, the underlying partial-equilibrium assumption should be examined. Among partially-equilibrated reactions, the water-gas shift (WGS) reaction is most often assumed to be in equilibrium because of its important role in the high temperature zone within the flame. In this chapter, the equilibrium domain of WGS reaction will be systematically analyzed to confirm the validity of partial equilibrium assumption. The numerical studies will be performed on a counter-flow diffusion flame fueled by different hydrocarbons with varying strain rates. Moreover, since most prior studies have been conducted for simple fuels like syngas and methane, not for higher hydrocarbons, it is also necessary to examine the mechanism for WGS-equilibrium among different type of fuels to shed a light on the partial-equilibrium behavior in the flames.

Met Measuring mixture fraction from the elemental species perspective provides substantial benefits over traditional measurement technique from the molecular species perspective. The LIBS technique not only can be applied to a broader range of equivalence ratios, but also enables the measurement in higher hydrocarbon fueled flames. In a flame zone where the minor species concentrations are not negligible, LIBS technique is more accurate by encompassing all species instead of tracking only major species. It is also more intuitive to analyze the preferential diffusion effect using the elemental species profile. However, in exchange for such benefits, the information for the major species concentrations can no longer be directly measured by LIBS. To infer the molecular species profile from the elemental species profile, the underlying partial-equilibrium assumption should be examined. Among partially-equilibrated reactions, the water-gas shift (WGS) reaction is most often assumed to be in equilibrium because of its important role in the high temperature zone within the flame. In this chapter, the equilibrium domain of WGS reaction will be systematically analyzed to confirm the validity of partial equilibrium assumption. The numerical studies will be performed on a counter-flow diffusion flame fueled by different hydrocarbons with varying strain rates. Moreover, since most prior studies have been conducted for simple fuels like syngas and methane, not for higher hydrocarbons, it is also necessary to examine the mechanism for WGS-equilibrium among different type of fuels to shed a light on the partial-equilibrium behavior in the flames.

6.1. Methods

The water-gas shift reaction can be represented as the sum of elementary reactions from the detailed mechanism. In the simplest case it can be written as:

$$H + H_2O \leftrightharpoons OH + H_2 \qquad \text{R1}$$

$$CO + OH \leftrightharpoons CO_2 + H \qquad \text{R2}$$

with the overall reaction -the WGS reaction- being the sum of these two reactions:

$$CO + H_2O \leftrightharpoons CO_2 + H_2 \qquad \text{R3}$$
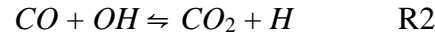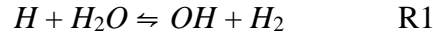
The quotient of the overall reaction is $Q_3 = [CO_2][H_2]/[CO][H_2O]$. For reactions R1 and R2 the quotients are $Q_1 = [OH][H_2]/[H][H_2O]$ and $Q_2 = [CO_2][H]/[CO][OH]$, respectively. Equilibrium can be assumed for the WGS reaction when Q_3 approaches the equilibrium constant for R3 ($K_{eq,3}$).

The kinetic ratio of the overall reaction, Q/K_{eq}, was employed to quantitatively assess the validity of the WGS equilibrium [11, 19] and to determine its parametric domain. The quotient was calculated from the numerical results, and the equilibrium constant was obtained from the CHEMKIN database [20]. WGS equilibrium was considered to be valid if $0.9 < Q/K_{eq} < 1.1$, in other words, when the deviation from equilibrium was less than 10% [5, 71].

The concentration and temperature profiles were numerically determined as functions of physical location (i.e., in 'physical space'). However, for utility of interpretation the modeling results will be presented in both mixture fraction space and C/O space. The mixture fraction Z can be obtained by normalizing a conserved scalar, $Z = \frac{S - S_2}{S_1 - S_2}$, where S is a conserved scalar which can

neither be destroyed nor generated in the combustion system, like the elemental fraction and the concentration of the inert. In this particular study, the physical meaning of the mixture fraction, the fraction of the mass originated from the fuel stream in the local mixture, is used to calculated the mixture fraction.

Recent studies have demonstrated that the C/O atomic ratio is a particularly useful variable to analyze diffusion flames [72]. The C/O atomic ratio (or C/O ratio) identifies the ratio of carbon atoms to oxygen atoms locally, and can be expressed as

$$C/O = \sum_i x * \chi^i_{C_xH_yO_z} \bigg/ \sum_i z * \chi^i_{C_xH_yO_z} \qquad (6.1)$$

where $\chi^i_{C_xH_yO_z}$ is the local mole fraction of the ith species in the flame, and x, y and z are the number of atoms of C, H and O in the substance, respectively. In C/O space, not only is the flame location independent of the boundary concentrations and strain rate, but the locations of critical zones, *e.g.,* the domains for radical depletion and precursor formation, are independent as well. In contradiction, these locations and domains are strongly dependent on boundary conditions in mixture fraction space.

The WGS reaction was systematically studied numerically in the counter-flow diffusion flame geometry for a variety of fuels and as a function of strain rate. The flames were modeled using the OPPDIF flame code. A total of 143 species and 938 reactions were included in the mechanism, which is a combination of the mechanism by Appel *et al.*[66] and USC Mech Version II, with chemistry up to pyrene from Wang and Frenklach [67].

Boundary conditions for the simulations are shown in Table 6.1. Here $V_{F,0}$ and $V_{O,0}$ are the inlet velocities at the fuel and oxidizer boundaries, respectively. All strain rates presented in this study will be global strain rates.

Table 6.1. Boundary conditions for the flames (simulation results)

Fuel	Z_{st}	C/Ost	$Y_{F,0}$	$Y_{O,0}$	$V_{F,0}$(cm/s)	$V_{O,0}$(cm/s)	Global strain rate(s^{-1})
ethylene	0.064	0.33	1.0	0.21	3.75	15	15
					37.5	37.5	75
					75	75	150
					112.5	112.5	225
					150	150	300
50:50 syngas	0.26	0.33	0.5CO/0.5H$_2$	0.21	15	15	30
					75	75	150
					150	150	300
methane	0.086	0.25	1.0	0.21	15	15	30
					37.5	37.5	75
propane	0.114	0.3	1.0	0.21	15	15	30
					37.5	37.5	75
					75	75	150

6.2. The equilibrium domain of the WGS reaction.

The domains of WGS equilibrium are shown in Fig. 6.1 for syngas, methane, ethylene and propane counterflow diffusion flames in air under a strain rate of 30s^{-1}. When analyzing a low strain rate syngas-air flame in either mixture fraction space or C/O space, the WGS kinetic ratio curve is found to have a broad plateau where the kinetic ratio is near unity. For example, for a strain rate of 30 s^{-1} the equilibrium domain for a syngas-air flame extends from $Z = 0.12$ to 0.31 or C/O = 0.11 to 0.51 (Fig. 6.1a). The trends for kinetic ratio are quite different for the hydrocarbon flames (Figs. 6.1b-d). The domain of WGS equilibrium in these flames can be divided into two zones separated by the temperature peak. On the fuel side of the temperature peak the profile exhibits a clear maximum, while on the oxidizer side it is a very narrow plateau. The coincidence of the temperature peak and the inflection point of the kinetic ratio curve can be

seen for all three hydrocarbon-air flames. For the different hydrocarbon flames, a comparison of

the equilibrium domains in mixture fraction and C/O space is presented in Table 6.2.
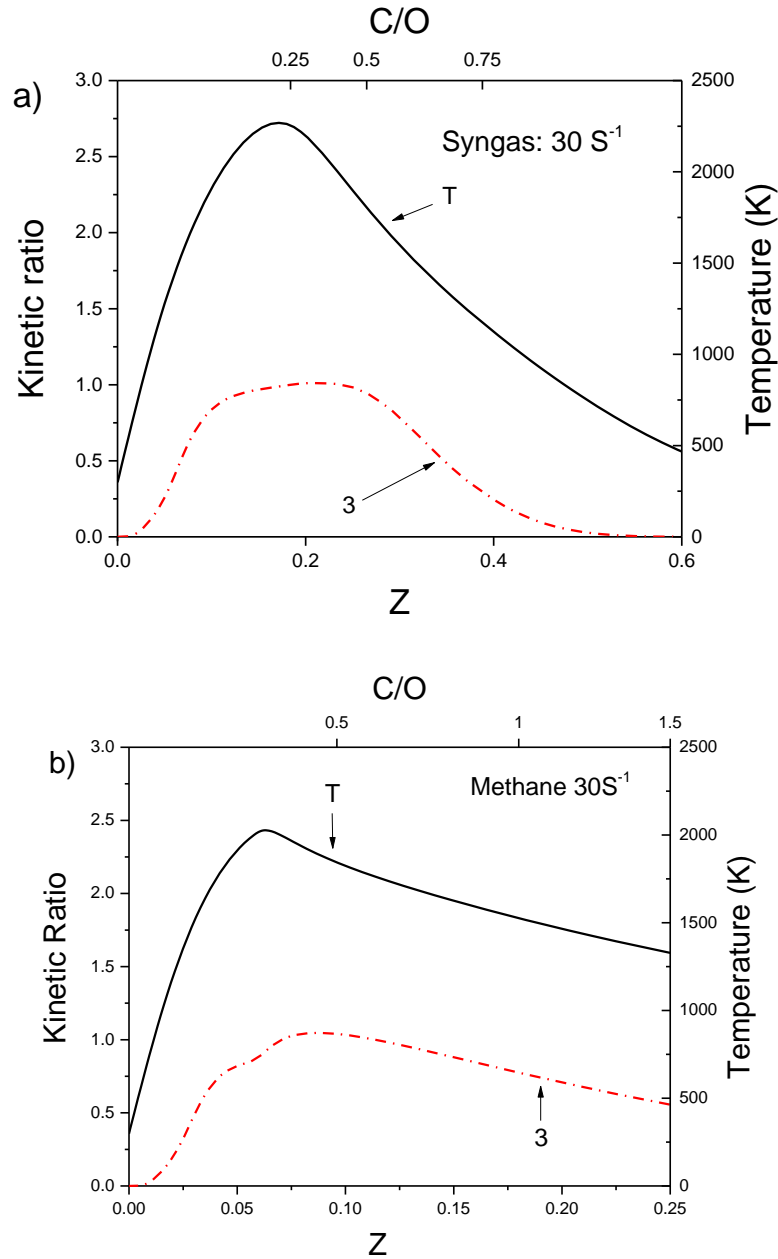
Figure 6.1. The domain of WGS equilibrium in Z and C/O space under a strain rate of $30s^{-1}$ for
(a) syngas-air (b) methane-air (c) ethylene-air and (d) propane-air counterflow diffusion flames
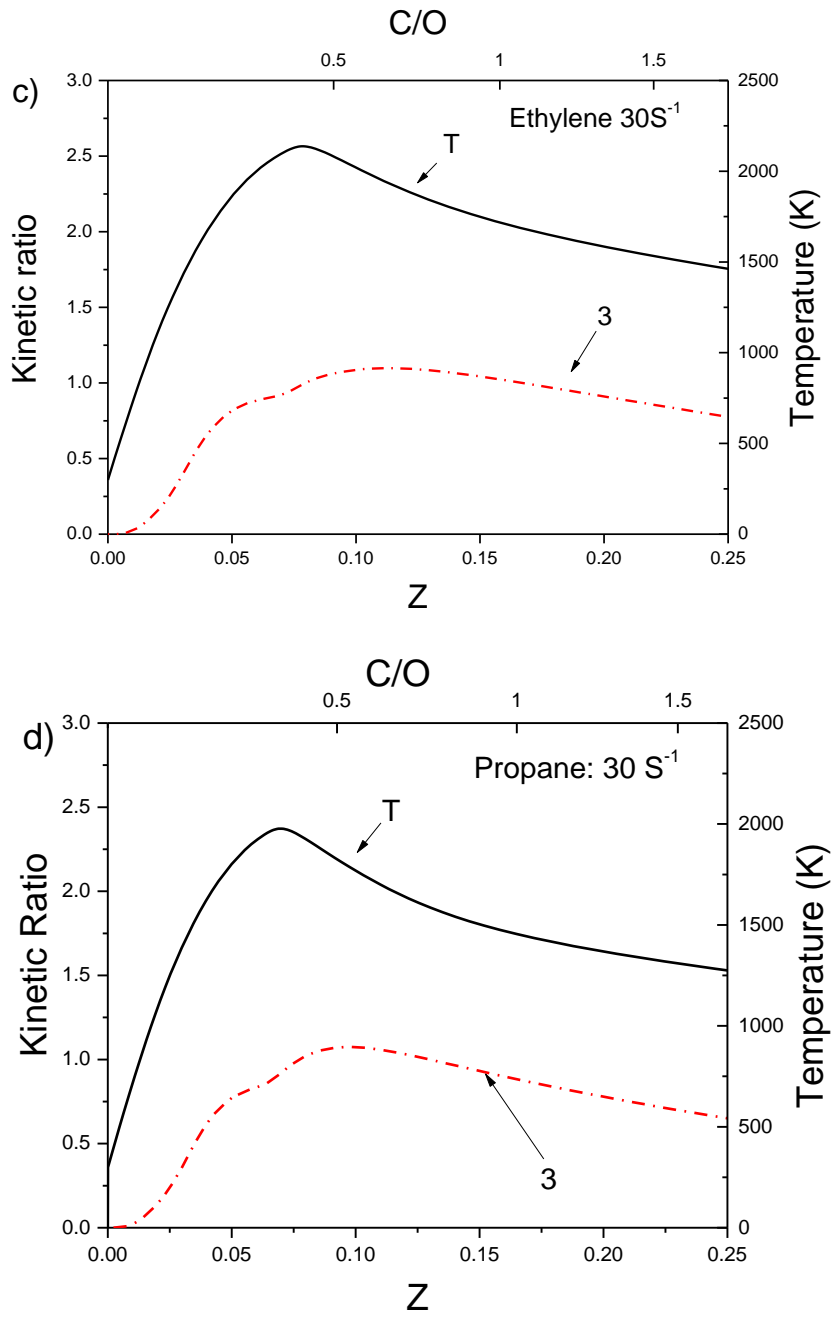
Figure 6.2. The domain of WGS equilibrium in Z and C/O space under a strain rate of 30s^{-1} for (a) syngas-air (b) methane-air (c) ethylene-air and (d) propane-air counterflow diffusion flames

Table 6.2. The domain of WGS equilibrium for different hydrocarbon flames in Z and C/O space

Fuel type	Equilibrium domain in Z space	Equilibrium domain in C/O space
Syngas	0.09-0.25	0.11-0.51
CH_4	0.06-0.14	0.28-0.77
C_2H_4	0.05-0.19	0.29-1.33
C_3H_8	0.05-0.17	0.33-0.95

The effect of strain rate on the WGS equilibrium was studied for diffusion flames of syngas-air and C_2H_4-air (Fig. 6.2). For the syngas flame, the region where the kinetic ratio is near unity shrinks as strain rate increases. In the ethylene-air flame, the peak value of the kinetic ratio can be greater than unity at low strain rate. The WGS reaction is equilibrated over a broad zone, extending into the fuel side. The shape of the kinetic ratio curve is rather invariant with strain rate, however, when the strain rate increases, the peak value of the kinetic ratio decreases. For both flames, when the strain rate is over 300 s^{-1}, the WGS equilibrium cannot be maintained and the peak kinetic ratio falls below unity.
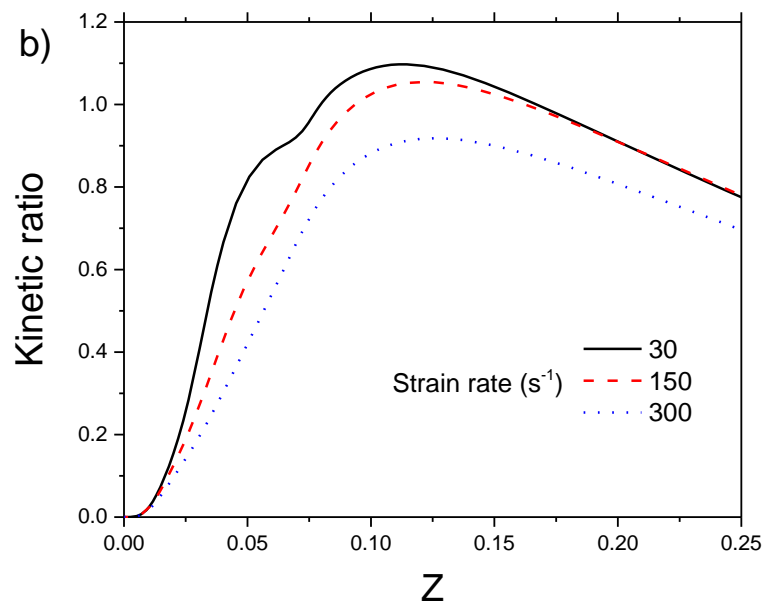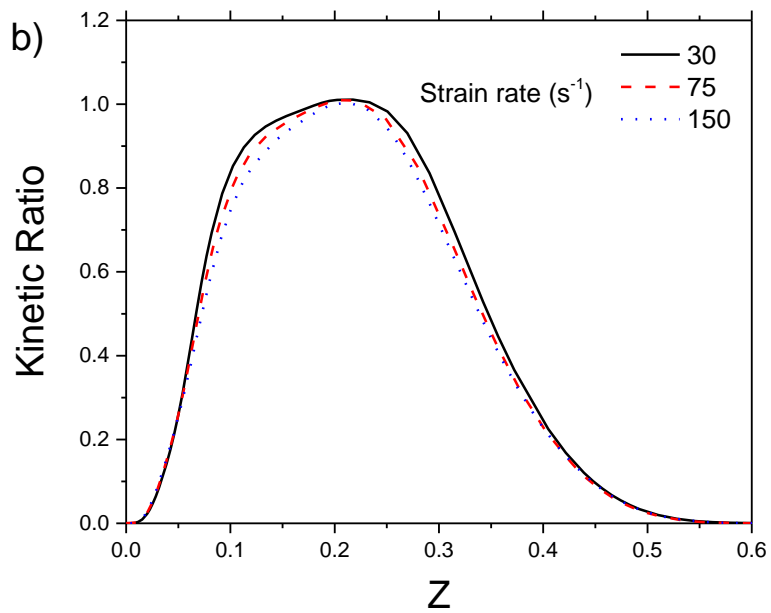
Figure 6.3. The kinetic ratio of WGS reaction under various strain rates: (a) syngas-air and (b) ethylene-air counterflow diffusion flames.

By analyzing the kinetic ratio of the overall WGS-reaction we have identified domains in which the kinetic ratio is close to unity; we consider this domain as the vicinity of overall WGS equilibrium (a domain of "overall equilibrium"). The next step will be to perform a similar analysis for R1 and R2, as these reactions constitute a mechanism for the WGS-route.

The analysis for syngas-air flames was performed for four different strain rates. Under a strain rate of $30s^{-1}$ (Fig. 6.3a), which yields sufficient time for these reactions to achieve the equilibrium, the WGS reaction is equilibrated from $0.15 < Z < 0.25$. Under a higher strain rate of $150 \ s^{-1}$ (Fig. 6.3c), the WGS equilibrium domain shrinks to $0.18 < Z < 0.22$. The same domain on the oxidizer side of the stoichiometric point barely exists, and on the fuel side it is preserved in a narrower region. Reactions R1 and R2 both have broad equilibrium domains, although the equilibrium domain of R2 is narrower than that of R1. Thus, the equilibrium domain for the WGS reaction is as wide as the partial-equilibrium domain for R2. When the strain rate is increased further (Fig. 6.3b-c), the partial-equilibrium domain of R1 shrinks slower than the equilibrium domain of R2; thus, the equilibrium of R2 remains the deciding factor for the overall WGS equilibrium.

a)

Syngas: 30 S^{-1}

b)

Syngas: 75 S^{-1}
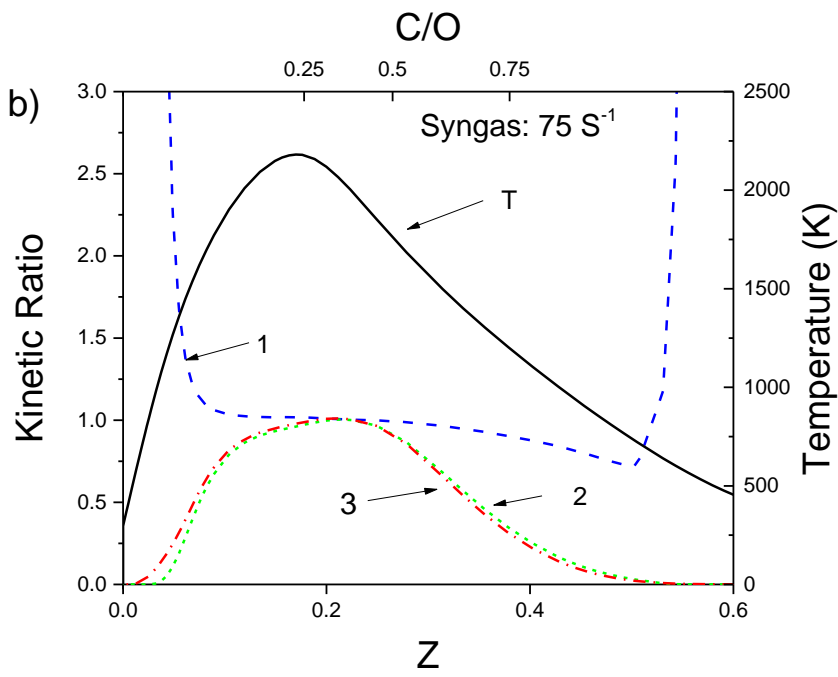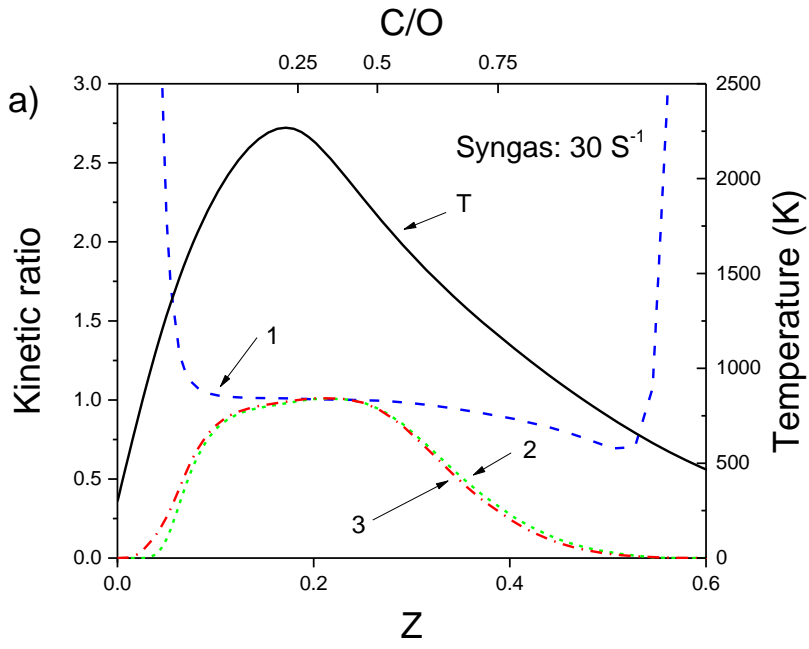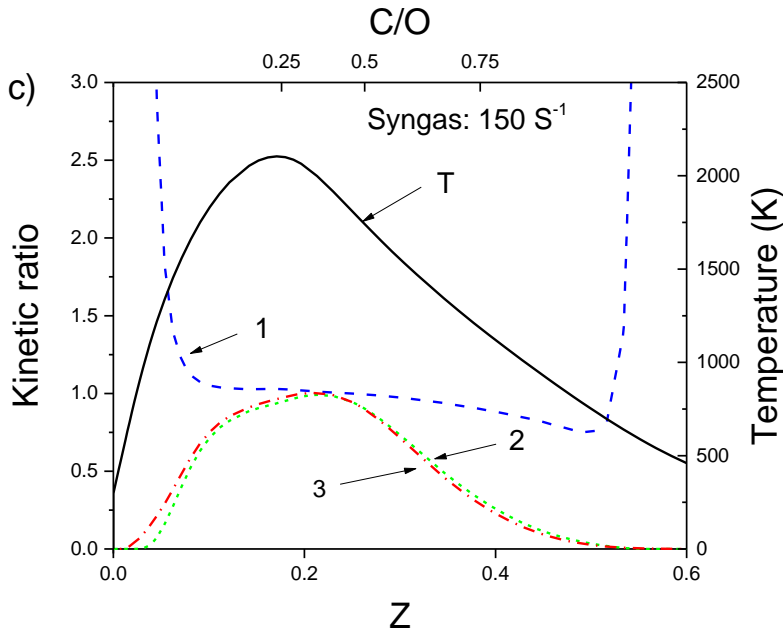
Figure 6.4. The kinetic ratio of R1 $(\frac{Q}{K})_1$ (blue dash), R2 ($(\frac{Q}{K})_2$) (green short dash), and the water-gas-shift overall reaction R3 ($(\frac{Q}{K})_3$) (red dash dot), and the temperature profile (T) (black solid) in syngas-air diffusion flames: (a) 30 s^{-1}, (b) 75 s^{-1}, (c) 150 s^{-1}

In Fig. 6. 4 the kinetic ratio profile was plotted for reactions R1-3 in C/O space for ethylene-air flames. Unlike the syngas-air flames in which R1 and R2 are both equilibrated to achieve water-gas-shift equilibrium, R1 and R2 are not in partial-equilibrium, and yet the overall WGS reaction is equilibrated. Distinctive behaviors can be observed in the two zones of WGS equilibrium. On the oxidizer side, R2 features a much narrower equilibrium domain than R1. This result indicates that R2 has a very narrow region of equilibrium even under the extremely low strain rate of 15 s^{-1}. The fuel side is characterized by a different behavior. The kinetic ratios for R1 and R2 deviate rapidly and stray away from unity throughout the regime. With increasing strain rate, R2 loses its equilibrium even in the vicinity of stoichiometry (Fig. 6.4b at 150 s^{-1}). Because there is essentially no equilibrium domain for R2 under the high strain rate (Fig. 6.4c), we might expect

that the WGS equilibrium is not achievable throughout the flame. However, as observed in Fig. 6.2b, the WGS reaction maintains its equilibrium until a strain rate of 300 s^{-1}. These results, when compared with those of Fig. 6.3, suggest that there are different causes for WGS equilibrium in syngas and ethylene flames; in other words, the 'co-equilibrium' for R1 and R2 cannot explain the cause for the WGS overall equilibrium in all scenarios. This will be elaborated in the next section.
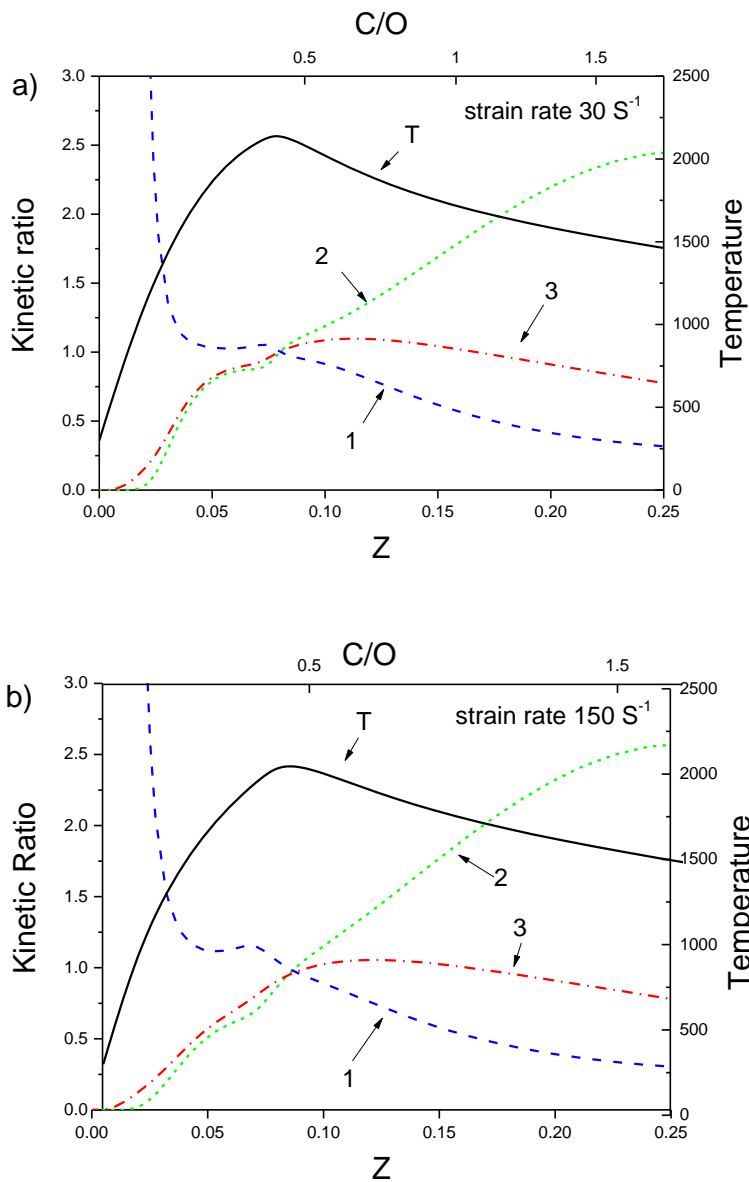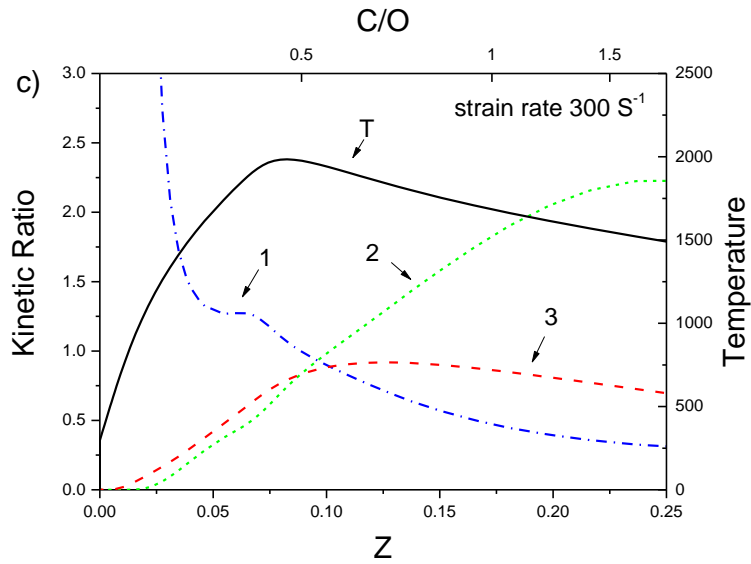
Figure 6.5. The kinetic ratio of R1 $(\frac{Q}{K})_1$ (blue dash), R2 ($(\frac{Q}{K})_2$) (green short dash), and the water-gas-shift overall reaction R3 ($(\frac{Q}{K})_3$) (red dash dot), and the temperature profile (T) (black solid) in ethylene-air diffusion flames: (a) 30 s^{-1}, (b) 150 s^{-1}, (c) 300 s^{-1}

6.3. The two scenarios of WGS equilibrium

The equilibrium constants and kinetic ratios of the WGS reaction and R1 and R2 are related by

$$\left(\frac{[CO_2][H_2]}{[CO][H_2O]}\right) eq = K_3 = K_1 K_2 \qquad (6.2)$$

$$\frac{[CO_2][H_2]}{[CO][H_2O]} = Q_3 = Q_1 Q_2 \qquad (6.3)$$

Thus,

$$\left(\frac{Q}{K}\right)_3 = \left(\frac{Q}{K}\right)_1 * \left(\frac{Q}{K}\right)_2 \qquad (6.4)$$

A trivial solution to Eq. 6.4 is that near equilibrium, *i.e.,* when $(Q/K)_3$ is close to 1, the kinetic ratio of the overall WGS-reaction can be achieved under conditions where R1 and R2 are equilibrated. However, it is also true that the same result can be achieved if R1 and R2 are shifted in opposite directions, *e.g.*, R1 to the forward reaction and R2 to the reverse reaction. As observed from the expressions for R1 and R2, this can occur when there is a relative excess of radical H in the working zone, and as a result, R1 and R2 are shifted to the forward and reverse directions, respectively.

Mathematically, this means that the overall WGS equilibrium will be valid as long as the relationship $1/\left(\frac{Q}{K}\right)_1 = \left(\frac{Q}{K}\right)_2$ holds approximately. Thus, there are two scenarios by which the overall equilibrium of the WGS reaction can exist in the flame, as will be explained in more detail below.

6.3.1. Full equilibrium

In the full equilibrium scenario, R1 and R2 are both under partial-equilibrium. The domain of full equilibrium for the WGS reaction is created as a result of the overlapping of two domains, i.e. partial-equilibrium domains of R1 and R2.

$$(\frac{Q}{K})_1 \approx (\frac{Q}{K})_2 \approx 1$$

In the syngas flame (Fig. 6.3), the partial-equilibrium zone of R1 is much wider than that of R2, preserving its broadness in both the fuel and oxidizer side of the flame even when the strain rate increases. Compared with R1, the partial-equilibrium domain of R2 shrinks quickly when the strain rate increases (Fig. 6.3b). In other words, the domain of R2 is more sensitive to the change of strain rate in both sides of the flame, which leads to the narrow WGS equilibrium zone in the vicinity of stoichiometry under higher strain rates for syngas flames.

6.3.2. Apparent equilibrium

We use the term 'apparent equilibrium' to distinguish this equilibrium from full equilibrium in which every relevant reaction is equilibrated. In the apparent equilibrium scenario, neither R1 nor R2 are equilibrated. However, in some regions of the flame the relationship $1/(\frac{Q}{K})_1 \approx (\frac{Q}{K})_2$ holds. Thus, $(\frac{Q}{K})_3 = (\frac{Q}{K})_1 * (\frac{Q}{K})_2 \approx 1$, and apparent equilibrium is exhibited.

Taking the ethylene-air flame as an example, on the fuel side, neither R1 nor R2 achieve partial-equilibrium even under extremely low strain rates (Fig. 6.4a). Instead, the reciprocal kinetic ratio of R1 and the kinetic ratio of R2 increase coherently. Consequently, we have $1/(\frac{Q}{K})_1 = (\frac{Q}{K})_2 \neq 1$; $(\frac{Q}{K})_3 = (\frac{Q}{K})_1 * (\frac{Q}{K})_2 \approx 1$, and in this way, the overall equilibrium for the WGS reaction is preserved. With increasing strain rate (Figs. 6.4b & c), the kinetic ratio of the WGS reaction remains around unity as long as $1/(\frac{Q}{K})_1$ and $(\frac{Q}{K})_2$ change coherently. As a result, the WGS equilibrium on the fuel side is sustained up to a strain rate of 375 s^{-1}. The WGS equilibrium is preserved at a much higher strain rate in the apparent equilibrium scenario than in the full equilibrium scenario, even though R1 and R2 are never equilibrated at the same time.

It is worth noting that the WGS equilibrium on the oxidizer side results from full equilibrium, i.e., both R1 and R2 are equilibrated. However, as we previously mentioned in the full equilibrium section, the equilibrium domain of R2 is quite narrow. Thus, full equilibrium in hydrocarbon flames can be observed only for very low strain rates (Fig. 6.4a). This result explains why full equilibrium is less often observed under higher strain rate (Fig. 6.4b) than apparent equilibrium.

The main factor contributing to this phenomena is the abundance of the H radical on the fuel side of the flame; this leads to a fast forward reaction for the first step and a fast reverse reaction for the second step, and the two balance each other, yielding apparent equilibrium. In comparison with the full equilibrium scenario, the domain of apparent equilibrium can be maintained under much higher strain rates, as shown in Figs. 6.4 – 6.6.

This scenario, where there are two modes of WGS equilibrium, is observed for other hydrocarbon diffusion flames as well. The results shown in Fig. 6.5 for propane-air flames under different strain rates reveal that even though R1 and R2 are not equilibrated individually at any point throughout the reaction zone, the net effect of two non-equilibrium reactions can yield the apparent equilibrium for the WGS reaction. This conclusion is also valid for methane-air flames (Fig. 6.6). For a clearer illustration of this phenomenon, the net reaction rates of R1 and R2 are shown in Fig. 6.7a for the ethylene-air flame under a strain rate of 150 s^{-1}, as an example. Throughout the reaction zone, R1 and R2 are found to be always proceeding in opposite directions. Nonetheless, apparent equilibrium is exhibited on the fuel side, and full equilibrium is exhibited on the oxidizer side. On the fuel side, both reactions yield H radical destruction, resulting in a net reaction as follows:

$$H + H_2O \; \rightarrow \; H_2 + \; OH \quad \text{R1}$$
$$CO_2 + H \rightarrow \; CO + OH \quad \text{-R2}$$
$$2H + H_2O + CO_2 \; \rightarrow \; CO + H_2 + 2\,OH. \; \text{R5}$$
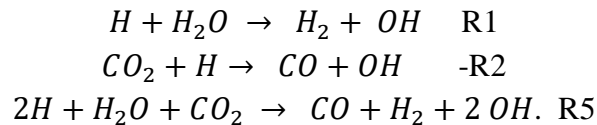
Taking the fact that on the oxidizer side the OH radical is enriched and on the fuel side the H radical is enriched (Fig. 6.7b), R1 and R2 are controlled by the external supply of radicals from the radical pool instead of being self-balanced by their thermodynamic nature. Since they are

both driven by the same abundant radical, $1/(\frac{Q}{K})_1$ and $(\frac{Q}{K})_2$ can be equal and yield an overall

water-gas-shift equilibrium.
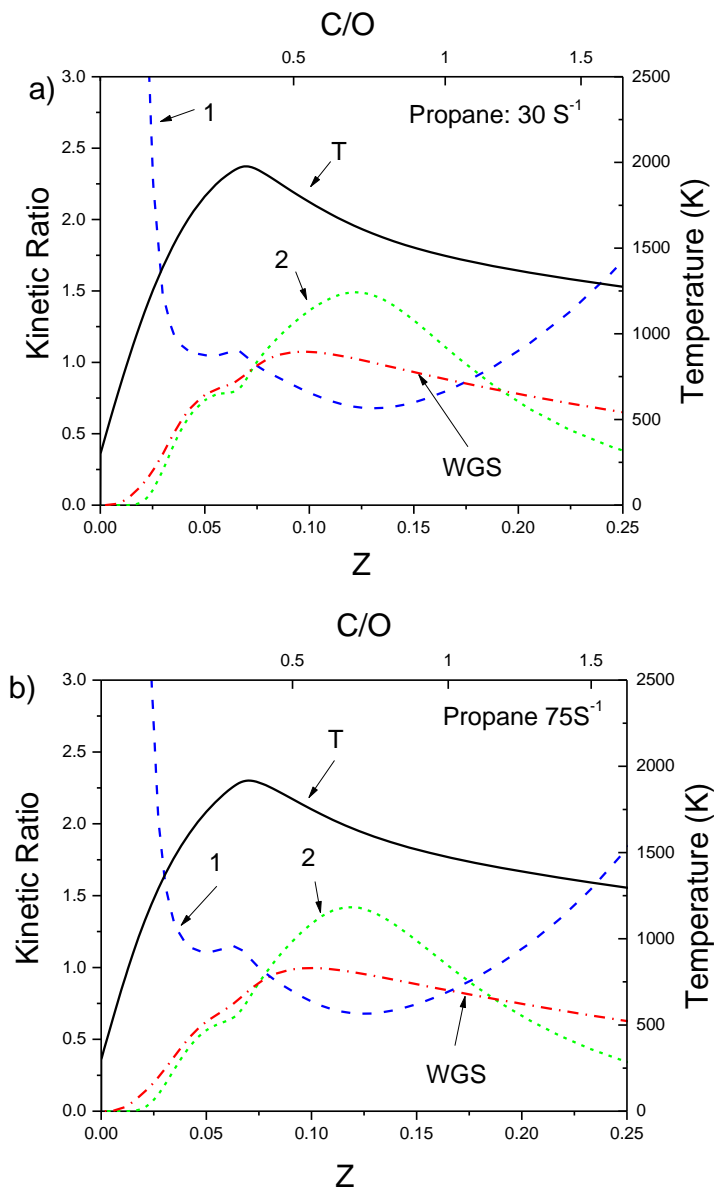
Figure 6.6. The kinetic ratio of R1 $(\frac{Q}{K})_1$ (blue dash), R2 ($(\frac{Q}{K})_2$) (green short dash), and the water-gas-shift overall reaction R3 ($(\frac{Q}{K})_3$) (red dash dot), and the temperature profile (T) (black solid) in propane-air diffusion flames: (a) 30 s^{-1}, (b) 75 s^{-1}.
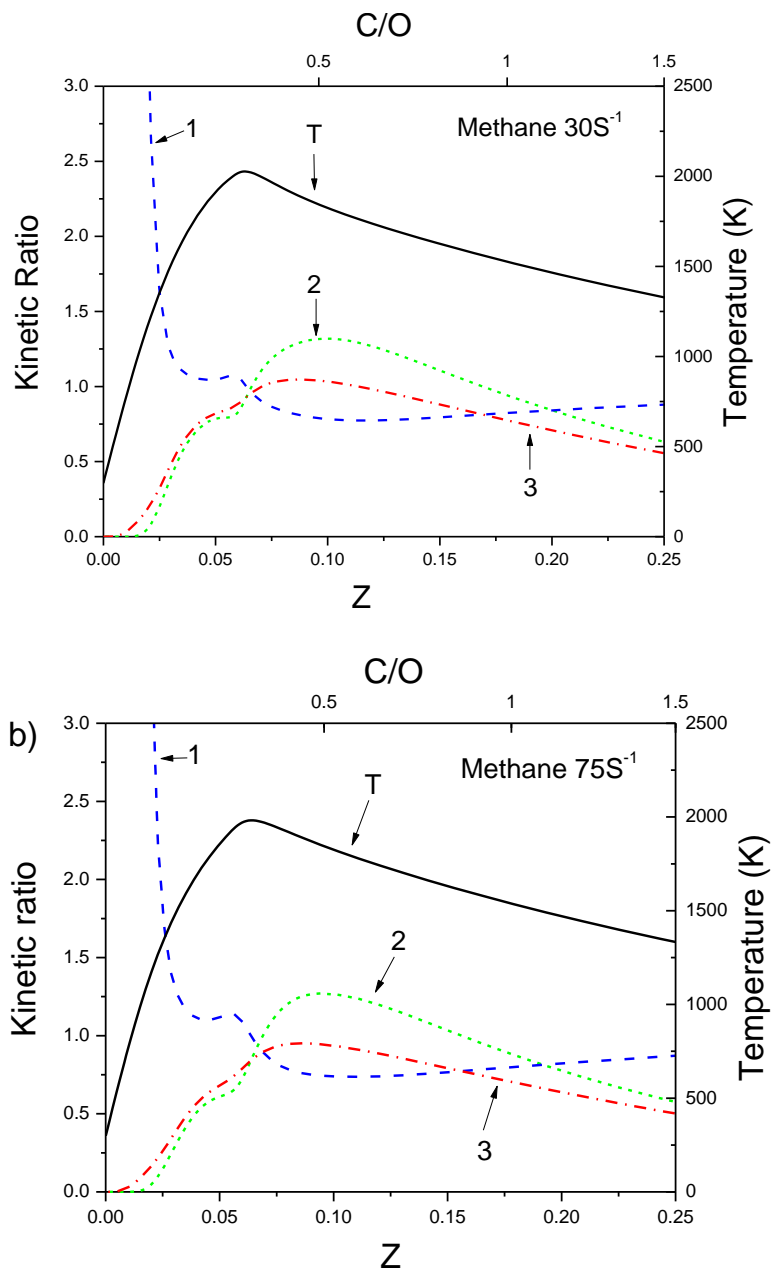
Figure 6.7 The kinetic ratio of R1 $(\frac{Q}{K})_1$ (blue dash), R2 ($(\frac{Q}{K})_2$) (green short dash), and the water-gas-shift overall reaction R3 ($(\frac{Q}{K})_3$) (red dash dot), and the temperature profile (T) (black solid) in methane-air diffusion flames: (a) 30s^{-1}, (b) 75s^{-1}.
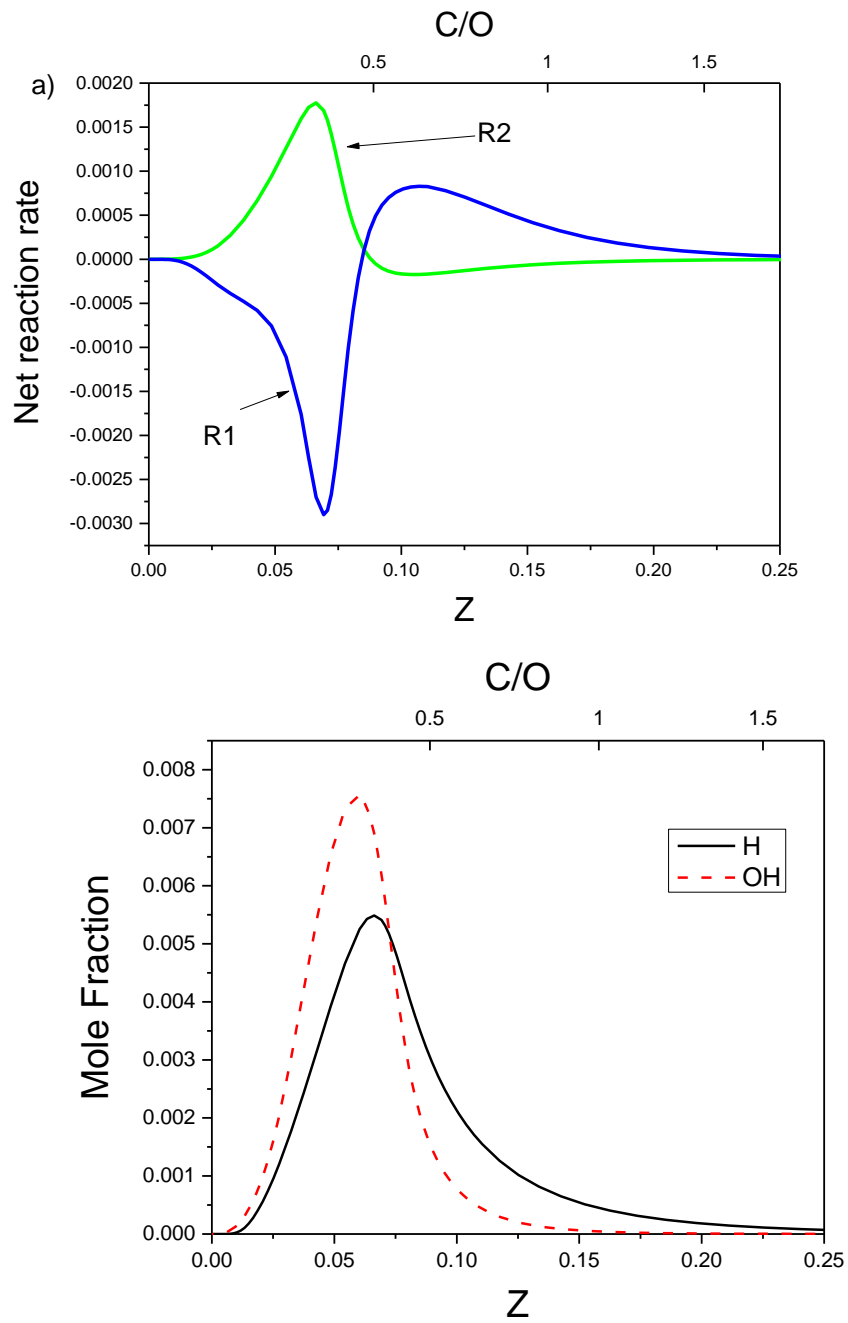
Figure 6.8. Profiles of (a) reactions rates for R1 and R2 and (b) mole fractions of H and OH under a strain rate of 150 s^{-1} in an ethylene-air counterflow flame.

A more detailed interpretation of this phenomenon can be presented as follows. The kinetic ratio of the net reaction R4 can be represented as

$$(\frac{Q}{K})_4 = (\frac{Q}{K})_1/(\frac{Q}{K})_2 = (\frac{Q}{K})_1 * \frac{(\frac{Q}{K})_2}{(\frac{Q}{K})_2^2} = (\frac{Q}{K})_3/(\frac{Q}{K})_2^2 \qquad (6.5)$$

The kinetic ratios of R4 and R3 are related by the square of $\frac{Q}{K_2}$. Defining $(\frac{Q}{K})_4$ as parameter A and looking for conditions of apparent equilibrium, $i.e.$, $(\frac{Q}{K})_3 = 1$, we get

$$A * \left(\frac{Q}{K}\right)_2^2 = 1 \qquad (6.6)$$

or

$$\frac{1}{\sqrt{A}} = (\frac{Q}{K})_2 = \frac{\frac{[CO_2][H]}{[CO][OH]}}{K_{eq2}} \qquad (6.7)$$

Thus,

$$\frac{[CO_2]}{[CO]} = \frac{K_{eq2}}{\sqrt{A}} * \frac{[OH]}{[H]} \qquad (6.8)$$

This relationship exhibits the specific nature of apparent equilibrium and establishes a possible link between the radical composition ratio $\frac{[OH]}{[H]}$ and the ratio of major species $\frac{[CO_2]}{[CO]}$ in the domain of WGS equilibrium. It can be used to gain a more detailed understanding of the kinetic behavior of counterflow flames.

This form of apparent equilibrium is an interesting phenomenon that apparently has not been identified previously [15-18]. A well-known form of apparent equilibrium is quasi-equilibrium, where equilibrium is observed when the forward and reverse reactions for one step are much

faster than for consecutive reactions. Here, however, we have identified a different type of apparent equilibrium. In this case the apparent equilibrium of the overall reaction is caused by the presence of a significant amount of one radical which is consumed by one elementary reaction and produced by another. Specific to our system, the overall reaction is the WGS reaction, the radical is H and the two elementary reactions are R1 and R2. While we have observed this new form of apparent equilibrium in hydrocarbon oxidation reactions, it has broader implications and is not limited to flames.

6.4.Summary

In this chapter, the WGS reaction was systematically studied in counterflow diffusion flames fueled by various hydrocarbons as well as syngas. Utilizing the kinetic ratio concept, the simulation results for syngas, methane, ethylene, and propane flames were compared and discussed. The evolution of the equilibrium domain due to changes in strain rate was also investigated.

The major conclusions are as follows:

1. The profiles of the kinetic ratio of the WGS reaction are similar for methane, ethylene and propane flames, but differ from that of the syngas flame. The hydrocarbon flames exhibit two zones of WGS equilibrium that are separated by the location of stoichiometry. The zone on the fuel side of stoichiometry shows a profile with a clear broad region of equilibrium, while the zone on the oxidizer side exhibits a very narrow region of equilibrium or none at all.

2. The domain of WGS equilibrium shrinks when the strain rate increases. The characteristic shape of the kinetic ratio curve is independent of strain rate; it always has a maximum, and the value of the maximum decreases with strain rate.

3. There are two scenarios for WGS equilibrium — full equilibrium and apparent equilibrium.

a) Full equilibrium of the overall WGS-reaction is a case in which both R1 and R2 are in equilibrium. In this region, R1 is more readily equilibrated; thus, the domain of full equilibrium is dictated by the domain of partial-equilibrium for R2. Such full equilibrium is observed in syngas flames and also on the oxidizer side for hydrocarbon flames.

b) Apparent equilibrium is observed on the fuel side of hydrocarbon flames. In this case, the WGS equilibrium is not caused by equilibrium for both R1 and R2, but rather by the coherent

opposing shifts of these reactions. Here R1 shifts to the right (forward), and R2 shifts to the left (reverse), and as a result, the reactions balance each other. Such apparent equilibrium of the overall WGS reaction can be sustained at much larger strain rates than in the case of full equilibrium. The mechanism responsible for this is that the H radical is common to both reactions, and is supplied to R1 an R2 as part of the radical pool.

4. The parametric domain for equilibrium for the overall WGS reaction is much wider than the domain of full equilibrium, in which every elementary reaction associated with WGS is in equilibrium. This effect is achieved by the elevated concentration of the intermediate (in our case, H radical). It is possible that apparent equilibrium can be observed, not only for the WGS-reaction in flames, but also for other complex chemical reactions with cyclic mechanisms.

Chapter 7: Summary and recommendations for future work

Motivated to improve the efficiency of combustion process and reduce the emission, in this dissertation, we would like to advance the fundamental understanding of flame structure through the development of laser plasma diagnostics. The laser induced breakdown spectroscopy (LIBS) was adapted as a mixture fraction measurement method. The acoustic aided laser induced breakdown thermometry (LIBT) was developed to measure the temperature simultaneously. The spatial and temporal resolution of LIBS and LIBT were investigated to demonstrate the potential of simultaneous composition and temperature measurement. In order to retrieve the concentrations of major molecular species from the elemental species profiles, the domain and mechanism of water-gas-shift partial equilibrium were also investigated. Preliminary research on turbulent systems was conducted as well to shed a light on future applications. The summary of major achievements and the recommendations for future work will be discussed in more details below.

7.1. Summary of major achievements.

1. From the elemental species perspective instead of molecular species perspective, the laser-induced breakdown spectroscopy (LIBS) technique was adapted as a mixture fraction measurement method. Using an ethylene fueled flat flame under equivalence ratios from 0.6 to 1.5, LIBS technique demonstrated that its usefulness can be expanded

to a broader range of equivalence ratios and fuels than existing methods like Raman spectroscopy.

2. A back-scattering setup was introduced to mitigate the beam steering effect in the flame. Using an economical ungated spectroscopy, LIBS technique achieved a spatial resolution of 125 µm in a counter-flow diffusion flame. The LIBS measured mixture fraction distribution compared favorably to the numerical results.

3. On the basis of LIBS measured elemental species profiles, the preferential diffusion effect was investigated experimentally without ignoring the minor species like molecular species based diagnosis. The LIBS measured results agreed well with the prediction of simulation, demonstrating that the light hydrogen containing species have diffused rapidly into the oxidizer side while the less-mobile carbon containing species have diffused to a lesser degree

4. The correlation between the acoustic signal and the atomic peak emission from the laser induced plasma was studied in the air and for the first time in the flame. The established correlation demonstrated the potential of utilizing the acoustic signal as an internal standard to normalize the LIBS spectra.

5. The acoustic based laser-induced breakdown thermometry (LIBT) was developed as a novel method to measure the flame temperature. The concept was validated on a McKenna burner with thermocouple measured temperature. The temperature and compositional effects on the acoustic signal from the laser induced plasma were both evaluated. The composition is a secondary factor compared to the temperature in the equivalence ratio domain of 0.8-1.7; thus, the influence from the composition was ignored in the later determination of temperature.

6. The spatial and temporal resolution of LIBS and LIBT were investigated based on the statistics. The results indicated that LIBS and LIBT having matching spatial and temporal resolution. The capability of simultaneous composition and temperature measurement using laser plasma diagnostics was not only explored theoretically, but also demonstrated on a counter-flow diffusion flame.

7. A preliminary evaluation of laser plasma diagnostics in turbulent flames was conducted using a Hecken burner. The results suggested that the shot-to-shot fluctuation is much more severe in the turbulent flames than in the laminar flames. The temporal resolution is lower for a given accuracy. The influence of the turbulent flames on the light path was investigated as well using a Burke Schumann flame. The steady turbulent flame presented in the light path induced only a minor influence while the unsteady flame hugely impacted the shot-to-shot fluctuation.

8. In order to retrieve the major molecular species concentrations from the elemental species profiles measured by the laser plasma diagnostics, the domain and mechanism of water-gas-shift partial equilibrium were investigated. The results suggested that even though the WGS reaction has a broad partial-equilibrium domain in syngas, methane, ethylene and propane flames, the mechanisms behind the partial equilibrium were very different. The water-gas-shift reaction can achieve partial equilibrium in hydrocarbon flames while two elemental reactions behind it are not equilibrated but preceding in the same direction instead.

7.2. Recommendations.

The LIBS and LIBT demonstrated their capability in measuring the composition and temperature simultaneously in a broader range of systems and equivalence ratios than existing techniques. The spatial resolution of them is restricted by the beam quality of laser and the optical setup. Given current spatial resolution of 50 μm with a M^2 of 4.4, limited benefits can be yielded from improving the focusing; however, a 4.4 times improvement is theoretically possible. To further exploit the potential of laser plasma diagnostics in the flame research, the efforts should be oriented towards pushing the temporal resolution to the plasma lifetime, which is the theoretical ceiling of this technique. The major challenge faced by future researchers is that due to the random nature of plasma generation, the shot-to-shot fluctuation is unavoidable and hard to mitigate. Compared with absolute amount measurement, the atomic ratio measurement suffers much less because its inherent robustness. On the other hand, the acoustic signal from the laser plasma suffers from significant shot-to-shot fluctuations along with the atomic peak emission it correlates to, especially in the turbulent flames. Since the temporal resolution is critical to the application in the unsteady flames, further efforts should be allocated in this direction. The time-resolved LIBS can possibly improve the S/N ratio of composition experiment. On the other hand, the spatial-resolved LIBS is not recommended because of the beam steering effect caused by the changing flame front.

References

[1] U.S.E.I. Administration, Annual Energy Review, 2012.

[2] S. Turns, An introduction to combustion : concepts and applications, WCB/McGraw-Hill2000.

[3] C.K. Law, Combustion physics, Cambridge University Press2006.

[4] R.W. Bilger, REACTION-RATES IN DIFFUSION FLAMES, Combustion and Flame 30 (1977) 277-284.

[5] R.S. Barlow, J.H. Frank, A.N. Karpetis, J.Y. Chen, Piloted methane/air jet flames: Transport effects and aspects of scalar structure, Combustion and Flame 143 (2005) 433-449.

[6] R.W. Bilger, S.H. Stårner, R.J. Kee, On reduced mechanisms for methane   air combustion in nonpremixed flames, Combustion and Flame 80 (1990) 135-149.

[7] J.C. Biordi, C.P. Lazzara, J.F. Papp, Flame Structure Studies of Cf3br-Inhibited Methane Flames .3. Effect of 1-Percent Cf3br on Composition, Rate Constants, and Net Reaction-Rates, J Phys Chem-Us 81 (1977) 1139-1145.

[8] J.D. Bittner, A molecular beam mass spectrometer study of fuel-rich and sooting benzene-oxygen flames, Massachusetts Institute of Technology, 1981, pp. 3 v. (960 i.e. 961 leaves).

[9] R.J. Cattolica, OH radical nonequilibrium in methane   air flat flames, Combustion and Flame 44 (1982) 43-59.

[10] R.E. Teets, J.H. Bechtel, Sensitivity analysis of a model for the radical recombination region of hydrocarbon-air flames, Symposium (International) on Combustion 18 (1981) 425-432.

[11] J.R. Bulau, W.E. Kaskan, Radical Overshoots and Dissociation in Methane-Air Flames, J Chem Phys 62 (1975) 3605-3608.

[12] S.R. Smith, A.S. Gordon, Studies Of Diffusion Flames. I. The Methane Diffusion Flame, The Journal of Physical Chemistry 60 (1956) 759-763.

[13] R.E. Mitchell, A.F. Sarofim, L.A. Clomburg, PARTIAL EQUILIBRIUM IN THE REACTION ZONE OF METHANE-AIR DIFFUSION FLAMES, Combustion and Flame 37 (1980) 201-206.

[14] R.E. Mitchell, A.F. Sarofim, L.A. Clomburg, EXPERIMENTAL AND NUMERICAL INVESTIGATION OF CONFINED LAMINAR DIFFUSION FLAMES, Combustion and Flame 37 (1980) 227-244.

[15] K.C. Smyth, J.H. Miller, R.C. Dorfman, W.G. Mallard, R.J. Santoro, Soot Inception in a Methane Air Diffusion Flame as Characterized by Detailed Species Profiles, Combustion and Flame 62 (1985) 157-181.

[16] K.C. Smyth, P.J.H. Tjossem, A. Hamins, J.H. Miller, Concentration measurements of OH· and equilibrium analysis in a laminar methane-air diffusion flame, Combustion and Flame 79 (1990) 366-380.

[17] J. Warnatz, STRUCTURE OF FREELY PROPAGATING AND BURNER-STABILIZED FLAMES IN THE H2-CO-O2 SYSTEM, Ber. Bunsen-Ges. Phys. Chem. Chem. Phys. 83 (1979) 950-957.

[18] M.C. Drake, R.J. Blint, STRUCTURE OF LAMINAR OPPOSED-FLOW DIFFUSION FLAMES WITH CO/H-2/N-2 FUEL, Combust. Sci. Technol. 61 (1988) 187-224.

[19] K.C. Smyth, P.J.H. Tjossem, RADICAL CONCENTRATION MEASUREMENTS IN HYDROCARBON DIFFUSION FLAMES, Applied Physics B-Photophysics and Laser Chemistry 50 (1990) 499-511.

[20] K.C. Smyth, P.J.H. Tjossem, A. Hamins, J.H. Miller, CONCENTRATION MEASUREMENTS OF OH. AND EQUILIBRIUM-ANALYSIS IN A LAMINAR METHANE AIR DIFFUSION FLAME, Combust. Flame 79 (1990) 366-380.

[21] S.H. Chung, F.A. Williams, ASYMPTOTIC STRUCTURE AND EXTINCTION OF CO-H2 DIFFUSION FLAMES WITH REDUCED KINETIC MECHANISMS, Combust. Flame 82 (1990) 389-410.

[22] R.S. Barlow, G.J. Fiechtner, C.D. Carter, J.Y. Chen, Experiments on the scalar structure of turbulent CO/H2N2 jet flames, Combustion and Flame 120 (2000) 549-569.

[23] H.Y. Shih, J.R. Hsu, A computational study of combustion and extinction of opposed-jet syngas diffusion flames, Int. J. Hydrog. Energy 36 (2011) 15868-15879.

[24] R.S. Barlow, Unexpected Effects Of Preferential Transport In Turbulent Premixed Flames, JOINT MEETING- US SECTIONS OF THE COMBUSTION INSTITUTE 2 (2011).

[25] R.S. Barlow, R.W. Dibble, J.Y. Chen, R.P. Lucht, Effect of Damköhler number on superequilibrium OH concentration in turbulent nonpremixed jet flames, Combustion and Flame 82 (1990) 235-251.

[26] R.S. Barlow, A.N. Karpetis, J.H. Frank, J.Y. Chen, Scalar profiles and NO formation in laminar opposed-flow partially premixed methane/air flames, Combustion and Flame 127 (2001) 2102-2118.

[27] A.N. Karpetis, R.S. Barlow, Measurements of scalar dissipation in a turbulent piloted methane/air jet flame, Proceedings of the Combustion Institute 29 (2002) 1929-1936.

[28] F. Fuest, G. Magnotti, R.S. Barlow, J.A. Sutton, Scalar structure of turbulent partially-premixed dimethyl ether/air jet flames, Proceedings of the Combustion Institute 35 (2015) 1235-1242.

[29] F. Fuest, R.S. Barlow, G. Magnotti, A. Dreizler, I.W. Ekoto, J.A. Sutton, Quantitative acetylene measurements in laminar and turbulent flames using 1D Raman/Rayleigh scattering, Combustion and Flame 162 (2015) 2248-2255.

[30] V. Narayanaswamy, R. Burns, N.T. Clemens, Kr-PLIF for scalar imaging in supersonic flows, Optics Letters 36 (2011) 4185-4187.

[31] A.G. Hsu, V. Narayanaswamy, N.T. Clemens, J.H. Frank, Mixture fraction imaging in turbulent non-premixed flames with two-photon LIF of krypton, Proceedings of the Combustion Institute 33 (2011) 759-766.

[32] R.L. Axelbaum, C.K. Law, W.L. Flower, Preferential diffusion and concentration modification in sooting counterflow diffusion flames, Symposium (International) on Combustion 22 (1989) 379-386.

[33] A. Michalakou, P. Stavropoulos, S. Couris, Laser-induced breakdown spectroscopy in reactive flows of hydrocarbon-air mixtures, Applied Physics Letters 92 (2008).

[34] K. Johannes, L. Zhongshan, A. Marcus, Laser-induced breakdown spectroscopy in a partially premixed turbulent jet flame, Measurement Science and Technology 24 (2013) 075205.

[35] S. Joshi, D.B. Olsen, C. Dumitrescu, P.V. Puzinauskas, A.P. Yalin, Laser-Induced Breakdown Spectroscopy for In-Cylinder Equivalence Ratio Measurements in Laser-Ignited Natural Gas Engines, Appl. Spectrosc. 63 (2009) 549-554.

[36] J. Kiefer, J.W. Tröger, Z.S. Li, M. Aldén, Laser-induced plasma in methane and dimethyl ether for flame ignition and combustion diagnostics, Applied Physics B 103 (2011) 229-236.

[37] J. Kiefer, J.W. Tröger, T. Seeger, A. Leipertz, B. Li, Z.S. Li, M. Aldén, Laser-induced breakdown spectroscopy in gases using ungated detection in combination with polarization

filtering and online background correction, Measurement Science and Technology 21 (2010) 065303.

[38] M.S. Mansour, H. Imam, K.A. Elsayed, W. Abbass, Local equivalence ratio measurements in turbulent partially premixed flames using laser-induced breakdown spectroscopy, Spectrochimica Acta Part B: Atomic Spectroscopy 64 (2009) 1079-1084.

[39] V. Sturm, R. Noll, Laser-Induced Breakdown Spectroscopy of Gas Mixtures of Air, CO2, N2, and C3H8 for Simultaneous C, H, O, and N Measurement, Applied Optics 42 (2003) 6221-6225.

[40] S. Zhang, X. Yu, F. Li, G. Kang, L. Chen, X. Zhang, Laser induced breakdown spectroscopy for local equivalence ratio measurement of kerosene/air mixture at elevated pressure, Optics and Lasers in Engineering 50 (2012) 877-882.

[41] M.M. Tripathi, K.K. Srinivasan, S.R. Krishnan, F.Y. Yueh, J.P. Singh, A comparison of multivariate LIBS and chemiluminescence-based local equivalence ratio measurements in premixed atmospheric methane-air flames, Fuel 106 (2013) 318-326.

[42] F. Ferioli, S.G. Buckley, Measurements of hydrocarbons using laser-induced breakdown spectroscopy, Combustion and Flame 144 (2006) 435-447.

[43] F. Ferioli, P.V. Puzinauskas, S.G. Buckley, Laser-induced breakdown spectroscopy for on-line engine equivalence ratio measurements, Applied Spectroscopy 57 (2003) 1183-1189.

[44] T.X. Phuoc, Laser-induced spark for simultaneous ignition and fuel-to-air ratio measurements, Optics and Lasers in Engineering 44 (2006) 520-534.

[45] T.X. Phuoc, F.P. White, Laser-induced spark for measurements of the fuel-to-air ratio of a combustible mixture, Fuel 81 (2002) 1761-1765.

[46] P. Stavropoulos, A. Michalakou, G. Skevis, S. Couris, Quantitative local equivalence ratio determination in laminar premixed methane-air flames by laser induced breakdown spectroscopy (LIBS), Chemical Physics Letters 404 (2005) 309-314.

[47] A.E. Majd, A.S. Arabanian, R. Massudi, M. Nazeri, Spatially Resolved Laser-Induced Breakdown Spectroscopy in Methane?Air Diffusion Flames, Applied Spectroscopy 65 (2011) 36-42.

[48] M. Kotzagianni, S. Couris, Femtosecond laser induced breakdown spectroscopy of air-methane mixtures, Chemical Physics Letters 561 (2013) 36-41.

[49] M. Mansour, H. Imam, K.A. Elsayed, A.M. Elbaz, W. Abbass, Quantitative mixture fraction measurements in combustion system via laser induced breakdown spectroscopy, Optics and Laser Technology 65 (2015) 43-49.

[50] D.X. Du, R.L. Axelbaum, C.K. Law, SOOT FORMATION IN STRAINED DIFFUSION FLAMES WITH GASEOUS ADDITIVES, Combustion and Flame 102 (1995) 11-20.

[51] S. Krishnan, B.M. Kumfer, W.D. Wu, J.C. Li, A. Nehorai, R.L. Axelbaum, An Approach to Thermocouple Measurements That Reduces Uncertainties in High-Temperature Environments, Energy & Fuels 29 (2015) 3446-3455.

[52] P.R.N. Childs, J.R. Greenwood, C.A. Long, Review of temperature measurement, Rev. Sci. Instrum. 71 (2000) 2959-2978.

[53] I.C.E. Turcu, M.C. Gower, P. Huntington, Measurement of KrF laser breakdown threshold in gases, Optics Communications 134 (1997) 66-68.

[54] J. Kiefer, J.W. Troger, Z.S. Li, T. Seeger, M. Alden, A. Leipertz, Laser-induced breakdown flame thermometry, Combustion and Flame 159 (2012) 3576-3582.

[55] A. Hrdlicka, L. Zaoralkova, M. Galiova, T. Ctvrtnickova, V. Kanicky, V. Otruba, K. Novotny, P. Krasensky, J. Kaiser, R. Malina, K. Palenikova, Correlation of acoustic and optical

emission signals produced at 1064 and 532 nm laser-induced breakdown spectroscopy (LIBS) of glazed wall tiles, Spectrochimica Acta Part B-Atomic Spectroscopy 64 (2009) 74-78.

[56] G.Y. Chen, E.S. Yeung, ACOUSTIC-SIGNAL AS AN INTERNAL STANDARD FOR QUANTITATION IN LASER-GENERATED PLUMES, Analytical Chemistry 60 (1988) 2258-2263.

[57] C. Chaleard, P. Mauchien, N. Andre, J. Uebbing, J.L. Lacour, C. Geertsen, Correction of matrix effects in quantitative elemental analysis with laser ablation optical emission spectrometry, Journal of Analytical Atomic Spectrometry 12 (1997) 183-188.

[58] M. Oksanen, J. Hietanen, PHOTOACOUSTIC BREAKDOWN SOUND SOURCE IN AIR, Ultrasonics 32 (1994) 327-331.

[59] Q. Qin, K. Attenborough, Characteristics and application of laser-generated acoustic shock waves in air, Applied Acoustics 65 (2004) 325-340.

[60] N. Hosoya, M. Nagata, I. Kajiwara, Acoustic testing in a very small space based on a point sound source generated by laser-induced breakdown: Stabilization of plasma formation, Journal of Sound and Vibration 332 (2013) 4572-4583.

[61] N. Hosoya, M. Nagata, I. Kajiwara, R. Umino, Nano-second Laser-induced Plasma Shock Wave in Air for Non-contact Vibration Tests, Experimental Mechanics 56 (2016) 1305-1311.

[62] D.A. Hutchins, Mechanisms of pulsed photoacoustic generation, Canadian Journal of Physics 64 (1986) 1247-1264.

[63] C. DeMichelis, Laser interaction with solids - A bibliographical review, IEEE Journal of Quantum Electronics 6 (1970) 630-641.

[64] S. Maurice, R.C. Wiens, M. Saccoccio, B. Barraclough, O. Gasnault, O. Forni, N. Mangold, D. Baratoux, S. Bender, G. Berger, J. Bernardin, M. Berthe, N. Bridges, D. Blaney, M. Bouye, P. Cais, B. Clark, S. Clegg, A. Cousin, D. Cremers, A. Cros, L. DeFlores, C. Derycke, B. Dingler, G. Dromart, B. Dubois, M. Dupieux, E. Durand, L. d'Uston, C. Fabre, B. Faure, A. Gaboriaud, T. Gharsa, K. Herkenhoff, E. Kan, L. Kirkland, D. Kouach, J.L. Lacour, Y. Langevin, J. Lasue, S. Le Mouelic, M. Lescure, E. Lewin, D. Limonadi, G. Manhes, P. Mauchien, C. McKay, P.Y. Meslin, Y. Michel, E. Miller, H.E. Newsom, G. Orttner, A. Paillet, L. Pares, Y. Parot, R. Perez, P. Pinet, F. Poitrasson, B. Quertier, B. Salle, C. Sotin, V. Sautter, H. Seran, J.J. Simmonds, J.B. Sirven, R. Stiglich, N. Striebig, J.J. Thocaven, M.J. Toplis, D. Vaniman, The ChemCam Instrument Suite on the Mars Science Laboratory (MSL) Rover: Science Objectives and Mast Unit Description, Space Science Reviews 170 (2012) 95-166.

[65] R.C. Wiens, S. Maurice, B. Barraclough, M. Saccoccio, W.C. Barkley, J.F. Bell, S. Bender, J. Bernardin, D. Blaney, J. Blank, M. Bouye, N. Bridges, N. Bultman, P. Cais, R.C. Clanton, B. Clark, S. Clegg, A. Cousin, D. Cremers, A. Cros, L. DeFlores, D. Delapp, R. Dingler, C. D'Uston, M.D. Dyar, T. Elliott, D. Enemark, C. Fabre, M. Flores, O. Forni, O. Gasnault, T. Hale, C. Hays, K. Herkenhoff, E. Kan, L. Kirkland, D. Kouach, D. Landis, Y. Langevin, N. Lanza, F. LaRocca, J. Lasue, J. Latino, D. Limonadi, C. Lindensmith, C. Little, N. Mangold, G. Manhes, P. Mauchien, C. McKay, E. Miller, J. Mooney, R.V. Morris, L. Morrison, T. Nelson, H. Newsom, A. Ollila, M. Ott, L. Pares, R. Perez, F. Poitrasson, C. Provost, J.W. Reiter, T. Roberts, F. Romero, V. Sautter, S. Salazar, J.J. Simmonds, R. Stiglich, S. Storms, N. Striebig, J.J. Thocaven, T. Trujillo, M. Ulibarri, D. Vaniman, N. Warner, R. Waterbury, R. Whitaker, J. Witt, B. Wong-Swanson, The ChemCam Instrument Suite on the Mars Science Laboratory (MSL) Rover: Body Unit and Combined System Tests, Space Science Reviews 170 (2012) 167-227.

[66] J. Appel, H. Bockhorn, M. Frenklach, Kinetic modeling of soot formation with detailed chemistry and physics: Laminar premixed flames of C-2 hydrocarbons, Combustion and Flame 121 (2000) 122-136.

[67] H. Wang, M. Frenklach, A detailed kinetic modeling study of aromatics formation in laminar premixed acetylene and ethylene flames, Combustion and Flame 110 (1997) 173-221.

[68] R. Noll, Laser-Induced Breakdown Spectroscopy: Fundamentals and Applications, Springer2012.

[69] J.P. Singh, S.N. Thakur, Laser-Induced Breakdown Spectroscopy, Elsevier Science2007.

[70] A.P.M. Michel, A.D. Chave, Analysis of laser-induced breakdown spectroscopy spectra: The case for extreme value statistics, Spectrochimica Acta Part B-Atomic Spectroscopy 62 (2007) 1370-1378.

[71] F. Xia, R.L. Axelbaum, Simplifying the complexity of diffusion flames through interpretation in C/O ratio space, Computers & Mathematics with Applications 65 (2013) 1625-1632.

[72] F. Xia, G.S. Yablonsky, R.L. Axelbaum, Numerical study of flame structure and soot inception interpreted in carbon-to-oxygen atom ratio space, Proceedings of the Combustion Institute 34 (2013) 1085-1091.

Appendix A

Influence of renewable energy source penetration on the grid inertia

Wendong Wu[1]

[1]Department of Energy Environmental &Chemical Engineering,

Washington University in St Louis, St Louis, Missouri, USA

Abstract: Large-scale deployment of Renewable Energy Sources (RES) has led to significant reduction in the grid inertia because they do not provide rotational mass as conventional synchronized generators. As a result, the frequency dynamics are faster in power systems with low rotational inertia, making frequency control and power system operation more challenging. In this project, the impact of low rotational inertia resulted from large-scale RES penetration was investigated by using numerical tool. The benefit of introducing large-scale energy storage systems to RES penetrated grid as additional primary control was also investigated numerically. The results indicated that the reduced inertia have a significantly negative impact on the system dynamics however can be mitigated by faster primary control. Such results shed light on possible low cost solution in for higher RES penetrated electricity system.

1. Introduction

In recent years, the renewable energy sources (RES) has took an increasing portion in the total electric profile (Fig.1). In particular, the solar has increased from 0% to 0.5% in total generation and the wind jumped from 0.1% to 4.1% from 2000 to 2013. A large amount of penetration of wind turbines and PV panel is replacing the synchronous generators and the level of penetration is expected to further increase in the near future. Traditionally, the grid inertia is provided by conventional power plants consisting of large synchronous generators. The replacement of conventional power plants with renewable energy sources such as wind turbines which are not synchronized or the PV panels which do not provide any rotating mass leads to a reduction of

total inertia of the system. As a result, large rate of change in frequency will be observed during incident power fault. To maintain the stability of the grid, it is of necessity to investigate how the system dynamics will be changed under higher level of RES penetration before introducing more RES units into the electricity system. Moreover, it is also of interest that how to improve the stability in power systems with low inertia. Energy storage systems (ESSs) can contribute to power system with low inertia. Moreover, ESSs are considered as the perspective elements of the modern power system for integration of RES. They can as well participate at improving power quality and reliability. Thus, in this project, the impact of low rotational inertia resulted from large-scale RES penetration will be investigated by using numerical tools. The benefit of introducing large-scale energy storage systems to RES penetrated grid as additional primary control will also be investigated numerically.

U.S. Renewable Electricity Generation as a Percentage of Total Generation

	Hydropower	Solar	Wind	Geothermal	Biomass	Total Renewables
2000	7.2%	0.0%	0.1%	0.4%	1.6%	9.4%
2001	5.8%	0.0%	0.2%	0.4%	1.3%	7.7%
2002	6.8%	0.0%	0.3%	0.4%	1.4%	8.9%
2003	7.1%	0.0%	0.3%	0.4%	1.4%	9.1%
2004	6.7%	0.0%	0.4%	0.4%	1.3%	8.8%
2005	6.7%	0.0%	0.4%	0.4%	1.3%	8.8%
2006	7.1%	0.0%	0.7%	0.4%	1.3%	9.5%
2007	5.9%	0.0%	0.8%	0.4%	1.3%	8.5%
2008	6.2%	0.1%	1.3%	0.4%	1.3%	9.3%
2009	6.9%	0.1%	1.9%	0.4%	1.4%	10.6%
2010	6.3%	0.1%	2.3%	0.4%	1.4%	10.4%
2011	7.8%	0.2%	2.9%	0.4%	1.4%	12.6%
2012	6.8%	0.3%	3.4%	0.4%	1.4%	12.4%
2013	6.6%	0.5%	4.1%	0.4%	1.5%	13.1%

Figure. 1. US renewable electricity generation as a percentage of
total generation from 2000 to 2013[1]

2. Methods

The rotational energy in the synchronized generator can be given as

$$E_{kin} = \frac{1}{2}J(2\pi f_m)^2$$

where J is the moment of inertia of the synchronous machine and f_m is the rotating frequency of the machine. The inertia constant H for a synchronous machine is defined by

$$H = \frac{E_{kin}}{S_B} = \frac{J(2\pi f_m)^2}{2S_B}$$

Where S_B is the rated power of the generator and H denoting the time duration during which the machine can supply its rated power solely with its stored kinetic energy. Typical values for H are in the range of 2–10s.

When a power fault $\Delta P = P_m - P_e$ happens, where P_m is the mechanical power supplied by the generator and P_e as the electric power demand. The change in rotational energy can relates the frequency change to the power fault by $\frac{f_m}{2HS_B}$. This equation is referred to as the classic swing equation.

$$\dot{E}_{kin} = J(2\pi)^2 f_m \cdot \dot{f}_m = \frac{2HS_B}{f_m} \cdot \dot{f}_m = (P_m - P_e)$$

After assuming the frequency change is small and replacing f_m with f_0 which is the default frequency of the grid. $\frac{f_m}{2HS_B}$ become a system constant $\frac{f_0}{2HS_B}$ in the above swing equation. To investigate the effect of primary control in this study, we can further add augmented frequency damping which includes the load damping contributed by the synchronized load and the primary control damping to the swing equation and yield the following differential equation.

$$\Delta \dot{f} = \frac{f_0}{2HS_\text{B}} \cdot \left(\underbrace{-\left(k_\text{load} + k_\text{prim.}(t)\right) \cdot \Delta f}_{\text{Augmented Frequency Damping}} + \underbrace{\Delta P}_{\text{Fault}} \right)$$

Modeling this equation in MATLAB, the frequency response versus time can be obtained. The inertia constant H was varied from 3s to 9s in representative of different level of RES penetration. Moreover, to investigate the benefits of adding ESS to a RES highly penetrated grid, $k_{prim}(t)$ was varied in terms of both the magnitude and response time to represent the capacity and the response speed of ESS. Important parameters and decision variables put into this model is shown and explained in Table.1 below.

Input Parameter	Values	Comments
Power Fault ΔP	5% S_B	As percentage of Base Power S_B
Rotational Inertia H	3,6,9 s	Representing different level of RES penetration.
Load Damping k_{load}	1.5% S_B	As percentage of Base Power S_B, represent synchronized load
Primary Control $k_{prim}(t)$	0,10,20,30% of S_B	As percentage of Base Power S_B to represent the battery system capacity. $k_{prim}(t)$ is a dummy function representing the response time of the primary control. Equals 0 when t<response time, a constant when t>response time

Table.1 The important parameters in the MATLAB model

3. Results and Discussion

The influence of RES penetration to the system inertia was all lumped into inertia constant H. Here, the typical value of 9s was taken to represent a grid with minimal RES penetration while 6s and 3s was employed in representative of moderately and severely RES penetrated system, respectively. Keeping the primary control damping as a constant at 20% of rated power and taken effect after 3 second, the influence of reduced system inertia is shown in Fig.2. The same amount power error (5% of the rated power) was introduced to the system. Before the primary control took effect at 3s, the highly RES penetrated system (H=3s) has reached a much lower maximum excursion point than the RES less penetrated system. In 3 seconds, the frequency dropped to 58.80 Hz for H=3s, 59.35Hz for H=6s and 59.55Hz for H=3s. The lost inertia from the synchronized generator result in much faster frequency dynamics, in other words, much steeper frequency drop slope after a power error was introduced. As a result, much less response time is given to governing control before the system reaches the dead point. Such results were expected and placed challenges in maintaining grid stability with increasing level of RES penetration.
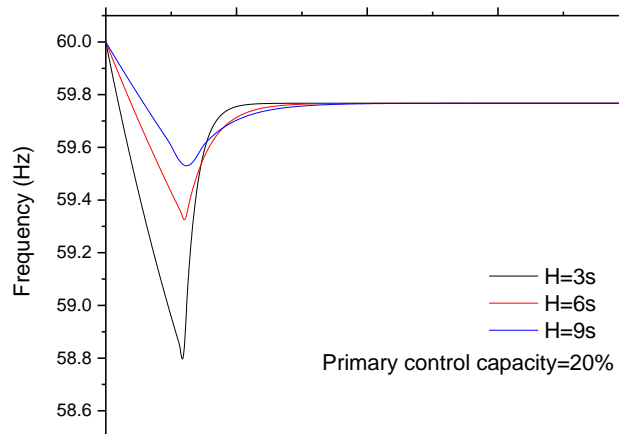
Fig 2. Frequency response after a 5% power error in systems with different level of RES penetration.

Furthermore, the influence of primary control are further investigated by varying both the magnitude and response tine of $k_{prim}(t)$. In Fig. 3, the frequency response of a moderately RES penetrated system (H=6s) was plotted with different level of primary control capacity. The results indicated that since the inertia of the grid and response time of the primary control are kept as constants, the maximum excursion point which determines whether the system will be damaged will remain the same regardless how large the capacity is. However, the system with a larger primary control capacity does have more headroom in restoring the default frequency in a short time frame before the secondary control takes place. In Fig.4, the capacity of primary control was kept at a constant of 20% S_B but the response time was varied instead from 2s to 4s. The influence of reduction in response time is very significant. A moderately RES penetrated system (H=6s) with a faster primary control of 2s has almost the same maximum frequency excursion at 59.55Hz with a minimal RES penetrated system (H=9s) with a slower primary control of 3s. A faster response primary control system instead of a large capacity system is more beneficial to mitigate the consequence of the lost inertia.
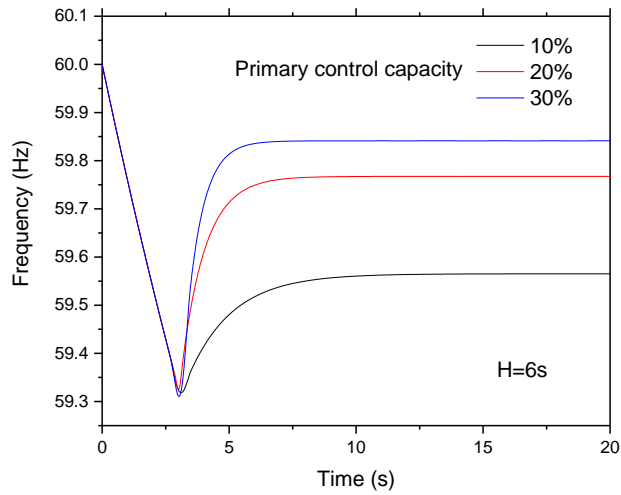
Fig.3 Frequency response after a 5% power error in systems with different capacities of primary control
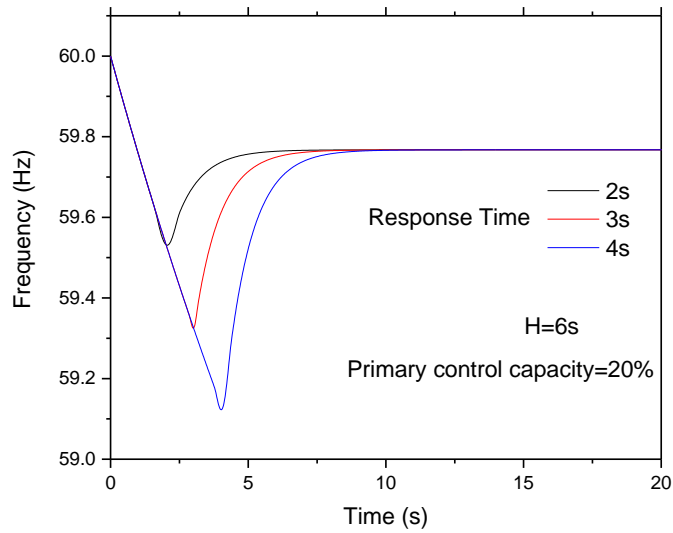
Fig.4 Frequency response after a 5% power error in systems with different response time of primary control

In this simple model, the characteristics of the system were lumped to 3 variables, the inertia constant H, the load damping constant k_{load} and the primary control parameter $k_{prim}(t)$. It is very straightforward that we can tell from the simulation that the smaller the inertia constant H, the steeper the frequency slope after a power error happens. It is also easy to tell that the larger the larger the load damping constant k_{load} is, the slower the system dynamic will be. Moreover, the response time of primary control seems to be more important than the capacity of the primary control. The response time determines when the system frequency is stopped from further dropping and determines the maximum frequency excursion along with the inertia. In the simulation, a moderately RES penetrated system (H=6s) with a faster primary control of 2s has almost the same maximum frequency excursion at 59.55Hz with a minimal RES penetrated system (H=9s) with a slower primary control of 3s. This result shed light on how faster ESS could help mitigate the influence of RES penetration.

The solution could be categorized into two approaches, the first one is increase the synchronized rotating mass in the system, it could be synchronized generators on the supply end, or synchronized load on the demand end. Without increasing conventional generators, the flywheel energy storage system which serves as the synchronized load could be a viable solution. Also, there some under developing technology like the WindINERTIA™ Control from GE would allow wind turbine to contribute to the system inertia. However, these solutions have to be put under careful techno-economic examination to see its feasibility in the real world. Another approach is to develop faster primary control technology. This is particularly attractive since the capacity is not as important as the response time. Faster battery storage systems could lead to low cost solution for higher RES penetrated systems.

4. **Conclusion**

In this study, a simple model has been applied to investigate the frequency response of the grid after a power error happens. The characteristics of the system were lumped to 3 variables, the inertia constant H, the load damping constant k_{load} and the primary control parameter $k_{prim}(t)$. The influence of RES penetration represented by H changes the frequency dropping slope thus a lower maximum excursion is achieved with larger scale RES penetration. Larger primary control capacity helps restore the frequency faster and gives more headroom before the secondary control takes place, however it has no impact on the maximum excursion in an event. Faster battery response time help mitigate the consequence of lost inertia. As a conclusion, the response time of the primary control is more important than the capacity in maintaining the grid stability. Such results shed light on possible low cost solution for higher RES penetrated electricity system.

References

[1]http://breakingenergy.com/2015/02/05/6-new-charts-that-show-us-renewable-energy-progress/

[2] O. Alsayegh, S. Alhajraf, H. Albusairi, Grid-connected renewable energy source systems: Challenges and proposed management schemes, Energy Conversion and Management 51 (2010) 1690-1693.

[3] A.P. Antony, D.T. Shaw, Empowering the electric grid: Can SMES coupled to wind turbines improve grid stability?, Renewable Energy 89 (2016) 224-230.

[4] N. Armaroli, V. Balzani, Towards an electricity-powered world, Energy & Environmental Science 4 (2011) 3193-3222.

[5] R. Bessa, C. Moreira, B. Silva, M. Matos, Handling renewable energy variability and uncertainty in power systems operation, Wiley Interdisciplinary Reviews-Energy and Environment 3 (2014) 156-178.

[6] O. Ellabban, H. Abu-Rub, F. Blaabjerg, Renewable energy resources: Current status, future prospects and their enabling technology, Renewable & Sustainable Energy Reviews 39 (2014) 748-764.

[7] J. Khan, M.H. Arsalan, Solar power technologies for sustainable electricity generation - A review, Renewable & Sustainable Energy Reviews 55 (2016) 414-425.

[8] M.U. Khan, K. Wali, K.S. Karimov, M.A. Saeed, A new proposed hierarchy for renewable energy generation to distribution grid integration, 2015 International Conference on Emerging Technologies, Ieee2015, pp. 6 pp.-6 pp.

[9] Y. Kumar, J. Ringenberg, S.S. Depuru, V.K. Devabhaktuni, J.W. Lee, E. Nikolaidis, B. Andersen, A. Afjeh, Wind energy: Trends and enabling technologies, Renewable & Sustainable Energy Reviews 53 (2016) 209-224.

[10] C.B. Li, H.Q. Shi, Y.J. Cao, J.H. Wang, Y.H. Kuang, Y. Tan, J. Wei, Comprehensive review of renewable energy curtailment and avoidance: A specific example in China, Renewable & Sustainable Energy Reviews 41 (2015) 1067-1079.

[11] T. Nacer, A. Hamidat, O. Nadjemi, A comprehensive method to assess the feasibility of renewable energy on Algerian dairy farms, Journal of Cleaner Production 112 (2016) 3631-3642.

[12] M. Nurunnabi, N.K. Roy, Renewable energy based hybrid power system: the best way to keep the world pollution free from GHG, 2015 2nd International Conference on Electrical Information and Communication Technologies, Ieee2015, pp. 539-544.

[13] A. Ulbig, G. Andersson, Analyzing operational flexibility of electric power systems, International Journal of Electrical Power & Energy Systems 72 (2015) 155-164.

[14] Y.S. Yu, J. Yang, B. Chen, The Smart Grids in China-A Review, Energies 5 (2012) 1321-1338.

[15] P. Kundur, "Power system stability and control," McGraw-Hill Inc., New York, 1994.

[16] P. Tielens and D. Van Hertem, "Grid inertia and frequency control in power systems with high penetration of renewables," Young Researchers Symposium in Electrical Power Engineering, Delft, vol. 6, April 2012.

[17] http://www.nrel.gov/docs/fy12osti/55335.pdf

[18] A. Ulbig, T. Borsche, G. Andersson, Impact of Low Rotational Inertia on Power System Stability and Operation https://arxiv.org/pdf/1312.6435.pdf

Appendix B

The land usage of renewable energy sources

Wendong Wu[1]

[1]Department of Energy Environmental &Chemical Engineering,

Washington University in St Louis, St Louis, Missouri, USA

Abstract: Renewable Energy Sources (RES) including wind and solar power has higher area requirement per unit capacity than conventional combustion based power plant. As a result, large-scale deployment of RES will place challenge in land arrangement especially near the power-demanding urban area. In this project, the land usage of RES is analyzed preliminary. Based on power density and consumption density data, the land usage in urban area was investigated.

1. The land use requirement and power density for wind power plant.

Development of a wind power plant results in a variety of temporary and permanent (lasting the life of the project) disturbances. These disturbances include land occupied by wind turbine pads, access roads, substations, service buildings, and other infrastructure which physically occupy land area, or create impermeable surfaces. Additional direct impacts are associated with development in forested areas, where additional land must be cleared around each turbine. While land cleared around a turbine pad does not result in impervious surfaces, this modification represents a potentially significant degradation in ecosystem quality. However, the direct impact area only accounts for the area taken up by physical infrastructure development. In order to characterize the land associated with the complete wind plant project, the more commonly cited land-use metric associated with wind power plants is the footprint of the project as a whole.

Generally, the total area of a wind power plant consists of the area within a perimeter surrounding all of the turbines in the project.

Table.1 Summary of collected wind power plant area data [1]

Data Type	Direct Impact Area		Total Area
	Permanent	Temporary	
Number of Projects with Corresponding Data	93	52	161
Total Capacity (MW) with Corresponding Data	13,897	8,984	25,438
Total Number of Turbines with Corresponding Data	8,711	5,541	15,871
Total Reported Area (km^2)	37.6	61.4	8,778.9
Average Area Requirements (hectare/MW)^4	0.3± 0.3	0.7 ± 0.6	34.5 ± 22.4

In Table.1, the wind power plant area data is demonstrated. It is worth paying attention that the data and analysis in Table.1 is associated with modern, large wind power plants (defined as greater than 20 megawatts (MW) and constructed after 2000). Considering these wind power plant already taken the best sites, this data could be considered as an optimistic estimation of large scale wind power deployment. The total project area of the wind power plant at 34.5 hectare/MW is 2 orders higher than the permanent direct impact area at 0.3hectare/MW, which corresponding to an energy density of only 3W/m^2 for the total project area and 33.3 W/m2 for the permanent direct impact area for installed name plate capacity. Thus, using direct impact area data could hugely underestimate the actual influence of wind power plant to the surrounding. Without considering the capacity value which refers to the contribution of a power plant to

129

reliably meet demand (In the case of wind power plants, it is 14.7% In MISO, 8.7% in ERCOT), the power factor for wind power is around 20% to 30% as shown in Fig. 1. Taking the capacity factor into our consideration will further reduced the power density of wind power plant to below 1W/m2 for total project area.
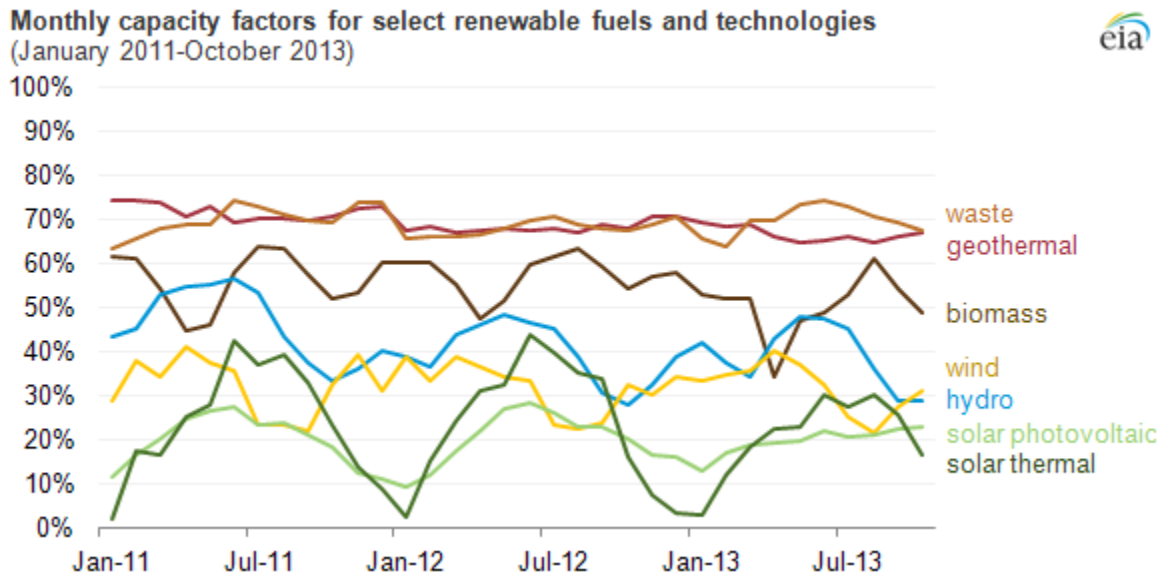
Fig.1 Monthly capacity factors for select renewable fuels and technologies from Jan 2011 to Oct 2013 [2]

2. The land use requirement and power density for solar power plants

The land usage for the solar power plants can be characterized similar to that of the wind power plants. The total area is defined by all land enclosed by the site boundary. The perimeter of this area is usually specified in blueprint drawings and typically fenced or protected. The direct impact area concept will only comprise land directly occupied by solar arrays, access roads, substations, service buildings, and other infrastructure. The direct-impact area is much smaller than the total area and is contained within the total-area boundaries as shown in Table.2. and Table. 3.

Table.2 Summary of direct land-use requirement for PV and CSP projects in the US[3]

Technology	Direct Area					
	Number of projects analyzed	Capacity for analyzed projects (MWac)	Capacity-weighted average land use (acres/MWac)	Capacity-weighted average land use (MWac/km^2)	Generation-weighted average land use (acres/GWh/yr)	Generation-weighted average land use (GWh/yr/km^2)
Small PV (>1 MW, <20 MW)	92	374	5.9	42	3.1	81
Fixed	43	194	5.5	45	3.2	76
1-axis	41	168	6.3	39	2.9	86
2-axis flat panel	4	5	9.4	26	4.1	60
2-axis CPV	4	7	6.9	36	2.3	105
Large PV (>20 MW)	15	1,405	7.2	34	3.1	80
Fixed	7	744	5.8	43	2.8	88
1-axis	7	630	9.0	28	3.5	71
2-axis CPV	1	31	6.1	41	2.0	126
CSP	18	2,218	7.7	32	2.7	92
Parabolic trough	7	851	6.2	40	2.5	97
Tower	9	1,358	8.9	28	2.8	87
Dish Stirling	1	2	2.8	88	1.5	164
Linear Fresnel	1	8	2.0	124	1.7	145

Table.3 Summary of total land-use requirement for PV and CSP projects in the US [3]

Technology	Total Area					
	Number of projects analyzed	Capacity for analyzed projects (MWac)	Capacity-weighted average land use (acres/MWac)	Capacity-weighted average land use (MWac/km^2)	Generation-weighted average land use (acres/GWh/yr)	Generation-weighted average land use (GWh/yr/km^2)
Small PV (>1 MW, <20 MW)	115	550	8.3	30	4.1	61
Fixed	52	231	7.6	32	4.4	56
1-axis	55	306	8.7	29	3.8	66
2-axis flat panel	4	5	13	19	5.5	45
2-axis CPV	4	7	9.1	27	3.1	80
Large PV (>20 MW)	32	3,551	7.9	31	3.4	72
Fixed	14	1,756	7.5	33	3.7	67
1-axis	16	1,637	8.3	30	3.3	76
2-axis CPV	2	158	8.1	31	2.8	89
CSP	25	3,747	10	25	3.5	71
Parabolic trough	8	1,380	9.5	26	3.9	63
Tower	14	2,358	10	24	3.2	77
Dish Stirling	1	2	10	25	5.3	46
Linear Fresnel	1	8	4.7	53	4.0	62

Using the most optimistic total land-use requirement for the 2-axis CPV in Table.3. The generation weighted average land use of 89GWh/yr/km^2 translates to 10W/m^2. Thus, the power density of solar power plant is significant higher than the power density of the wind power plant, however, it is economically inferior due to the high cost of solar power electricity.

3. The consumption density

The urban population of the US rose to 249.3 million in 2010, out of a total population of 308.7 million, that is 80% of population. Urbanization covered 106,000 square miles, representing 3.0 percent of the US land mass [5]. Approximately, the urban area places 1.5TW real time energy load on the electricity system. Thus, the consumption density of US urban area is around $5W/m^2$, which is about 5 times higher than the power density of wind power plant. In a modern society 100% powered by wind sourced electricity, more than 5 times of the total urbanized area need to be occupied by wind power plants. In relative terms, it is 16% of US total landmass or 1.5 million km^2 of land usage. Every urban area has to draw power from 5 "power cities" to support its energy need. It is very hard to image how to maintain such huge power cities especially the full life cycle of wind power plants is only around 30 years. It is also worth paying attention to that the capacity value of wind and solar is very low, which means their capacity has to be overly installed many times to reliably meet energy requirements. On top of this, the long range transmission loss and cost associated with transmitting electricity from remote power plants to urban area should also not be ignored. And as previous mentioned, the grid inertia will be diminished completely by 100% RES penetration. Hugh storage systems must be deployed to offset such impact.

Reference

[1] http://www.nrel.gov/docs/fy13osti/56290.pdf

[2] U.S.E.I. Administration, Annual Energy Review, 2012

[3] http://www.nrel.gov/docs/fy09osti/45834.pdf

[4] The US Bureau of the Census

Appendix C

An Approach to Thermocouple Temperature Measurements that Reduces Uncertainties Associated with Radiative Corrections

Siddharth Krishnan[†], Benjamin M. Kumfer[‡], Wendong Wu[‡], Jichuan Li[⊥], Arye Nehorai[⊥],

Richard L. Axelbaum[‡],*

AUTHOR ADDRESS Washington University in St. Louis, One Brookings Drive, St. Louis, MO

63130, USA

ABSTRACT Obtaining accurate temperature measurements with thermocouples in flame

environments is challenging due to the effects of radiative heat losses, as these losses are difficult

to quantify. Efforts to minimize radiative losses by, for example, suction pyrometry often result

in a significant sacrifice in spatial resolution. In this work, a new experimental methodology is

presented that both minimizes the temperature correction and allows the remaining correction to

be accurately quantified. The approach is based on increasing and controlling the convective heat

transfer to the thermocouple junction, and is accomplished by spinning the thermocouple at high

speed. The rotation yields a large and known convective velocity over the thermocouple. Heat

transfer can then be modeled for the thermocouple, and a functional relationship between

134

temperature and rotational speed can be found. Fitting this model to the data allows for an accurate temperature correction. To test the feasibility of the rotating thermocouple (RTC) technique for temperature measurement in high temperature gases, experiments were conducted over a range of rotational speeds in a controlled flame where the temperature was known. The measured thermocouple temperatures as a function of rotational speed closely match the theoretical temperatures, yielding a straightforward approach to highly accurate gas temperature measurement. The results also demonstrate minimal perturbation to the flow field, even at high rotational speeds. Finally, a deconvolution technique is proposed that would significantly enhance the spatial resolution of the technique, approaching that of a stationary thermocouple.

Nomenclature

A Area (m^2)

D Diameter of bead (m)

h Convective heat transfer coefficient (W/m^2-K)

RTC   Rotating thermocouple

L Length (m)

$\dot{Q}$ Heat flux (W)

r Radius (m)

T Temperature ($°C$)

V Velocity (m/s)

ω Rotational speed (*revolutions/min*)

σ   Stefan-Boltzmann constant $(5.67051 \times 10^{-8} \frac{W}{m^2 K^4})$

ε   Emissivity

k Thermal conductivity $(\frac{W}{m-K})$

μ Dynamic viscosity $(\frac{kg}{m-s})$

ρ Density (kg/m^3)

t Time (s)

τ Time constant (s)

Subscripts

b Bead (thermocouple bead)

cr Cross section

D Diameter

g Gas

s Surface

w Wall

Dimensionless Numbers

Bi Biot Number

Nu Nusselt Number

Pr Prandtl Number

Re Reynolds Number

1. Introduction

Temperature measurements are ubiquitous in combustion systems. These measurements are useful in a wide range of applications, from laboratory–scale flames to large scale boilers and furnaces. A variety of methods have been employed to make gas temperature measurements in flames. Broadly speaking, these methods can be classified into optical and probe-based measurements. Though optical approaches to gas temperature measurements provide some advantages over probe-based methods, they are often difficult to implement, can be costly and cumbersome, and are often not effective in particle laden flames [73]. Thus, probe-based measurements remain the method of choice for many combustion studies.

Among probe-based measurements, thermocouples have gained preeminence because they are inexpensive, robust and easy to use. The use of fine-wire thermocouples for flame temperature measurements has been extensively discussed.[73] Unfortunately, the use of thermocouples is subject to systematic errors arising from heat losses due to conduction and radiation.[73-78]

For fine-wire thermocouples, conduction losses are negligible and thus it is the radiation correction that presents the most difficult challenge to accurate measurement of gas temperatures. Radiation varies with the fourth power of temperature, so a sharp increase in radiative losses is observed with increasing gas temperature. At the high temperatures typically encountered in flame environments the error resulting from these losses can be hundreds of degrees [79, 80]. While the common challenge in laboratory flames is to correct for radiative cooling of the thermocouple due to radiation losses from the thermocouple to the environment,

Blevins and Pitt [80] have shown that radiative heating can be significant in the cooler parts of large scale flames where the thermocouple is heated by radiation from the hot surroundings such as furnace walls or from soot particle radiation.

Correcting for radiation losses or gains is complicated by uncertainties in variables such as the convective heat transfer coefficient, the bead size, shape and emissivity and the temperature and emissivity of the surroundings. The presence of particles in the flow creates additional challenges. Many simple algebraic models have been developed to correct for radiation losses from the bead [80]. [79] and some have been validated using CFD models.[81] Radiation gains due to radiation from the environment to the bead are system dependent, and thus no simple models are available for this correction.

One approach to radiation correction that has been extensively discussed is the use of multiple thermocouples (typically two) that are made of identical materials but of different diameters. In this way it is possible to extrapolate to zero-diameter.[82, 83] In unsteady flows the accuracy of this technique is limited by the different time constants of the thermocouples, owing to their different diameters, providing no clear relationship between bead size and temperature, though several frequency-based compensation techniques have been suggested.[83-86] Additionally, there is a dependence on the geometry and orientation of the thermocouples, which makes the technique difficult to implement in many practical combustion systems.

Perhaps the most widespread industrial approach to addressing the problem of radiation correction is the use of suction pyrometers, otherwise known as aspirated thermocouples, which are designed to minimize radiation losses.[80, 81, 87, 88] As the name suggests, suction pyrometers locally extract the combustion gases into a probe. The flow is accelerated within the probe so that it when it passes over the thermocouple the convective heat transfer is high and controlled. This high convective heat transfer brings the thermocouple closer to the gas temperature. Additionally, suction pyrometers are fitted with ceramic shields that enclose the thermocouple junction to protect it from incoming particles and reduce the radiative heat loss to the surroundings.[80, 89]

Suction pyrometers, however, have important limitations. They rely on extremely high aspiration velocities, often on the order of 150 m/s, to minimize the value of the error. This requires suction flow rates on the order of 300 L/min, and results in extremely poor spatial resolution and large disturbances to the flow field. This high sampling volume can also mean that suction pyrometers are impossible to implement in smaller burners. The probes are also large and cumbersome, and can be expensive. Additionally, in particle-laden flows, clogging is a problem, as the molten ash can deposit on surfaces.[73, 80, 89] Finally, the measurement may be affected by the orientation of the probe, and the probe has a very large time constant due to the shields,[73] making the measurements slow and cumbersome. For example, even at the extremely high aspiration velocity of 250 m/s, and an ambient temperature of 1600˚C, the probe can take up to 3 minutes to reach its equilibrium temperature, and an estimated 1 minute for a 100˚C increase in temperature.[90]

Aspiration velocity is the key operating parameter for suction pyrometers, but there is a disparity in views with respect to the optimal aspiration velocity. The ASTM recommended value is 5 m/s while others have recommended anywhere between 150 and 250 m/s [80, 89]. Blevins and Pitts[80, 89] discussed this disparity and showed that an aspiration velocity of as low as 5 m/s is usually a significant improvement over an open thermocouple measurement, but operation at this low velocity will result in high errors. For example, when the true gas temperature is 927 ºC and the surroundings are at room temperature, the temperature measured with a 1.5 mm thermocouple will increase sharply from 450 ºC to 730 ºC when the aspiration velocity is increased to 5 m/s, but will not approach the true gas temperature until the aspiration velocity is increased to 200 m/s, [80, 89] illustrating the diminishing value in operating at higher aspiration velocities.

The present study seeks to introduce a new experimental methodology to minimize radiation and conduction losses, and allow for accurate determination of temperature correction, and to do this without the level of sacrifice to spatial and temporal resolution that is inherent in aspiration thermocouple measurements. This is achieved by means of a high-speed rotating thermocouple (RTC), which ensures a high and quantifiable convective heat transfer, thereby minimizing the effects of radiation and conduction and ensuring a known correction value. A detailed description of the methodology and experimental system follows.

2. Design Considerations

Figure 1a shows a thermocouple in a flow of hot gas in an enclosure. A simple steady-state heat balance for this thermocouple bead, as shown in Fig. 1b, is given by

$$\dot{Q}_{conv} + \dot{Q}_{cond} + \dot{Q}_{rad} = 0 \qquad (1)$$

can either heat or cool the bead, depending on whether the bead is cooler or hotter than the gas, respectively. It can lose heat by conduction through its wires, and gain or lose heat through radiative exchange with its surroundings. If the temperature of the surroundings, T_s is lower than that of the thermocouple bead T_b, then the net radiation heat transfer will be from the bead to the surroundings. In practice, the emissivities of the surroundings and the bead can be difficult to accurately predict. The emissivity of the surroundings is system-dependent, and in particle-laden flows, it can be particularly difficult to calculate, as it will depend on the temperatures and the emissivities of the particles throughout the entire flow field. The emissivity of the bead can change based on length of exposure to the flow, as it can undergo chemical changes or be coated with soot or ash.

The convective heat transfer can be expressed simply by Newton's law of heating/cooling, and is equal to the product of the temperature difference between the gas and the bead, and the convective heat transfer coefficient, h and surface area A_{surf}. The conductive heat loss is directly proportional to the temperature gradient across the wire, given by ΔT, the cross-sectional area of the wire, A, and the thermal conductivity of the thermocouple material, k_b.

The net radiative heat flux entering or leaving the thermocouple depends on the temperatures of the thermocouple and the surroundings, the emissivity of the thermocouple, ε_b and the emissivity of the surroundings ε_s For illustrative purposes, we will assuming that the absorptivity and emissivity of the thermocouple are equal (Kirckoff's law) and that the emissivity of the

surroundings is unity. Using these assumptions and the above simplifications, Eq. (1) can be expanded and rewritten as

$$h(T_g - T_b) + e_b S(T_b^4 - T_w^4) + (\frac{k_b A}{L A_{surf}})DT = 0 \tag{2}$$

Rearranging Eq. (2), we get

$$T_g = T_b + \frac{[e_b S(T_b^4 - T_w^4) + (k_b A / L A_{surf})DT]}{h} \tag{3}$$

The second term on the right side of Eq. (3) represents a correction, or inaccuracy due to radiative and conductive heat losses. Increasing the value of the convective heat transfer coefficient, h, minimizes the value of the correction. The value of h can be calculated from the Nusselt number, which is a function of the Reynolds number and Prandtl number. A generalized form for the Nusselt number is given by

$$Nu_D = C \operatorname{Re}^m \operatorname{Pr}^n = hD/k_g \tag{4}$$

The constants C, m and n vary for different thermocouple geometries, Reynolds numbers and gas compositions. Solving Eq. (4) for h and plugging into Eq. (3) yields

$$T_g = T_b + \frac{[e_b S(T_b^4 - T_w^4) + (k_b A_{cr} / L A_{sur})DT]}{C \operatorname{Re}^m \operatorname{Pr}^n (\frac{k_g}{D})} \tag{5}$$

Eq. 5 contains a number of terms that are difficult to accurately quantify in laboratory and industrial-scale flames. The uncertainties in the emissivities of both the surroundings and the bead have already been discussed. The gas-properties, such as the Prandtl number and k_g are

dependent on temperature and composition, which are typically unknown. The Reynolds number is dependent on the local gas velocity over the thermocouple bead, V_g, which is also typically unknown. Moreover, in a turbulent system, V_g fluctuates, further complicating interpretation since the heat balance becomes an unsteady problem and the thermal mass of the bead becomes important.

While inherent uncertainties in thermocouple measurement can exist (for example, from installation errors of the thermocouple, signal errors in the transmission wires, analog-to-digital conversion, and conversion to temperature from voltage,[91], these uncertainties are typically small for flame temperature measurements and can often be ignored.

The challenges associated with thermocouple measurements in flames can be largely circumvented if the thermocouple is rotated at high speed. These benefits are clarified below.

The linear speed of the bead, V_b, is a function of the rotational speed, ω, and, if the rotational speed is fast enough that the surrounding gas velocity is small compared to V_b, then $V_{rel,}$ the total relative velocity between the bead and the gas, can be approximated by

$$V_{rel} \gg \frac{2\rho r W}{60} \qquad (6)$$

where r is the radius of the circular motion of the thermocouple, as shown in Fig. 2.

Here r is a design parameter and dictates how rotational speed translates into linear speed. This demonstrates one of the important benefits of spinning the thermocouple: while the gas velocity

143

over a thermocouple is typically unknown, spinning the thermocouple at sufficiently high speed

removes this uncertainly since, for sufficiently high rotational speeds the gas velocity over the

thermocouple can now be determined from the known rotational speed of the thermocouple.

Combining Eqs. (5) and (6), we obtain

$$T_g - T_b \approx \frac{S e_b (T_b^4 - T_w^4) + (\frac{k_b A}{L A_{surf}}) D T}{C(\frac{2 p r D_b r}{60 m} W)^m \Pr^n (\frac{k_g}{D_b})}$$
(7)

Eq. (7) provides us with a functional relationship between the rotational speed, the diameter of

the thermocouple and the correction. The denominator goes like ω^m, indicating that as the

rotational speed is increased, the magnitude of the correction is decreased. The exponent m is

typically around 0.5. This demonstrates a second important benefit of spinning the

thermocouple: the large relative velocity of the gas over the thermocouple leads to an increase in

the convective heat transfer coefficient, which decreases the radiation and conduction

corrections.

To gain an appreciation for the magnitude of the effect of spinning for realistic values of

rotational speed and bead size, the following assumptions are made. A flame temperature of

1500 °C is used and r is assumed to be 12 mm. The gas properties are evaluated at 1500 °C and

are assumed for nitrogen since a large fraction of the combustion gas is typically nitrogen. The

kinematic viscosity, v, is taken to be $27.5 \times 10^{-5} m^2/s$, the thermal conductivity, k, to be 0.09W/ m-

K, and the Prandtl number to be 0.73. The temperature of the surroundings, T_s, is taken to be 300

K. An emissivity of 0.1, that of uncoated platinum, is assumed for the thermocouple bead , and conduction losses are neglected.

For these assumptions, the Reynolds number is obtained and shown in Fig. 3a as a function of rotational speeds, with thermocouple bead diameter as a parameter. In Fig. 3b this is translated into Nu for a bead diameter of 0.203 mm. Since thermocouple beads are sometimes represented by a sphere and at other times by a cylinder, correlations for both geometries are considered in Fig. 3b.

In Fig. 4, the normalized bead temperature, T^*, as obtained from Eqn. (7), is plotted, using the Churchill-Bernstein correlation[92, 93] for flow over a cylinder. The normalized temperature is defined as the ratio of the thermocouple bead temperature T_b, to the true gas temperature T_g, in °C and is plotted as a function of rotational speed for various bead diameters. The smaller thermocouple bead size results in smaller radiative losses because of the reduced surface area. A key observation from this figure is that the effect of rotational speed on T^* is significant, and T^* asymptotes to unity for rotational speeds that are practically attainable (20,000 rpm). The bead temperature is strongly dependent on speed at low rpm and asymptotes to the true gas temperature as the speed goes to infinity.

Based on this information, an experimental apparatus was constructed to test the feasibility of this concept for measuring gas temperature in hot environments.

3. Experimental

A schematic of the system is shown in Fig. 5. A hollow shaft made of 347 stainless steel is fitted with a platinum-platinum/rhodium 10% (Type S) thermocouple. The dimensions of the shaft are 12.7 mm outer diameter, 3.18 mm inner diameter, and 165 mm length. The diameter of the thermocouple wire is 0.13 mm, and the size of the bead in these experiments is 0.20 mm. The wire diameter chosen represents an optimum, as it is significantly more robust than finer wire thermocouples while also being thin enough to minimize conduction losses. Tests were also conducted with a 0.05 mm diameter thermocouple, and stroboscopic measurements revealed that the thermocouple maintained its shape and did not deform while being spun. Nonetheless, fine wires of this size are not robust. Since the primary drawback of the larger wire size is the larger corrections due to radiation and conduction, which this work seeks to address, most experiments were conducted with the larger wire size of 0.13 mm diameter.

The thermocouple wire is housed inside an alumina ceramic tube and the wires protrude 14 mm from holes in the ceramic tubing, and are bent at nearly right angles to the longitudinal axis of the shaft, thereby creating a radius of 14 mm. The shape of the thermocouple bead more closely resembled a cylinder than a sphere, though it was not perfectly cylindrical. As will be shown, with the RTC it is not necessary to know the exact shape of the thermocouple.

The shaft is mounted to an AC motor that is equipped with a variable speed control and the rotational speed can be varied from 0 to 23,000 rpm. The rotational speed is measured using a non-contact laser tachometer. The low-voltage thermocouple signal is transmitted by means of a slip ring-brush system (Fabricast Inc., South El Monte, California) that is specifically designed

for thermocouple measurements. The analog signal is converted into a digital temperature reading using an MC USB-TC (Measurement Computing, Norton, MA) A/D board. The signal is converted to a temperature using a Type S calibration curve and fed to a computer where it is recorded in real-time using LabView (National Instruments, Austin, TX) software.

An important goal of this feasibility study was to experimentally determine the functional relationship between thermocouple bead temperature, T_b, on the rotational speed, ω. Once this is obtained, the value for T_g obtained from this functional relationship could then be compared with the value of T_g obtained from a stationary thermocouple. The stationary thermocouple was placed under conditions where the radiation correction could be estimated accurately to within 20°C and thus this temperature was treated as a known reference temperature.

To perform such a calculation, a McKenna premixed flat-flame burner was used to generate the experimental flame because of its ability to yield a controlled and quantifiable local velocity, its minimal temporal temperature variation and its well-characterized temperature distribution.[94, 95] The RTC assembly was mounted over the burner head. The 60 mm-diameter burner head is composed of sintered stainless steel and is water-cooled. The burner was fed with a propane-air mixture, and was shielded with an inert nitrogen shroud. The bead of the thermocouple was positioned 7.5 mm above the visible flame, and no disturbance to the flame was perceptible under these conditions. The sampling rate for these experiments was arbitrarily chosen to be 2 Hz, as the flame was steady and displayed negligible temporal variation in temperature. Three flames were produced for the experiments, with equivalence ratios of φ=1.0, 0.85 and 0.70. The air flow rate was held constant at 2.3 kg/hr, while the flow rate for propane was 0.092 kg/hr,

0.073 kg/hr or 0.068 kg/hr to yield the three equivalence ratios respectively, and a gas flow velocity of ~1.2 m/s. Catalytic effects, while often significant, can be neglected here because the thermocouple was in the post-flame region and the premixed system was operated with a fuel-lean stoichiometry.

The RTC assembly was mounted such that the plane of rotation for the thermocouple was parallel to the surface of the flat-flame burner, in other words, the bead was a fixed height above the burner head during its rotation. However, the McKenna burner is not truly one dimensional, as temperature gradients exist along the surface of the burner.[96] To address this and ensure that the gas temperature along the path of the spinning thermocouple was nearly constant, a portion of the burner that displayed minimal temperature variations was identified and used. This is important because when the thermocouple rotates it traces out a circumference of 44 mm. For the region of the burner that was used, a temperature variation of 35±5 °C was observed for the three flames that were used in this study. To obtain the average thermocouple temperature over this circumference, stationary temperature measurements were taken at 44 points around the circumference, with each measurement 1-mm apart, and the average of these measurements was computed. A radiation correction was then performed on this average temperature to yield the average gas temperature T_g along the path of the thermocouple bead

Additionally, a control thermocouple was constructed of Pt 30% Rh-Pt 6%Rh (Type B) alloy, with 0.20 mm bead diameter. This thermocouple was placed in the flame at the same height as the rotating thermocouple ± 1 mm, but at a distance of 5 mm from the rotating thermocouple at its closest location during rotation. This second thermocouple was used to evaluate the effect of

flame perturbation caused by the high-speed rotation, and the data was recorded simultaneously with the RTC as part of the same experiment, also at a sampling rate of 2Hz.

The stainless steel supporting rod and motor, shown in Fig. 5, were not cooled in this experiment because the heat from the flame products could be easily shielded from the rod and other components, so that the temperatures were never too high. In larger scale system, for example in a furnace, these parts would need to be cooled to ensure that the temperatures of these components are never too high. In particular the stainless rod, which must protrude into the flame, would need to be shielded, *e.g.*, with a water jacket, to keep it from warping.

The slip-ring bearings exhibited frictional heating. This heating led to a well-defined error in the signal, which was on the order of 7°C at 10,000 rpm, and virtually nonexistent below 5,000 rpm. The error was corrected for by using a calibration.

4. Results

Figure 6 shows raw data so that the dynamics of the system can be understood. Once the flame was lit, the thermocouple was kept stationary until it reached its steady-state temperature of 1207 $\pm$ 2 °C. The motor was then ramped up to a steady-state rotational speed of 3,000 rpm. This was not an instantaneous change and the ramping time was on the order of 2 seconds. The temperature was then allowed to reach steady state and attained a value of 1252 $\pm$ 2°C. The experiment was repeated, and this time the motor speed was ramped up to 7,000 rpm, and at this speed the steady-state temperature was 1277 $\pm$ 5 °C. As expected, the temperature of the rotating

thermocouple, T_b, is strongly dependent on rotational speed. Images were recorded of the RTC in motion at each of the rotational speeds discussed and are shown in Figs. 7a-d. Figure 7a shows the system. The aperture setting in this photograph is larger than for subsequent photographs to clearly illustrate the flat flame and the relative position of the RTC. Figs. 7b-d are taken with a smaller aperture setting to avoid saturation and clearly show differences in the brightness of the RTC with rotational speed. The increased brightness of the RTC at 7,000 rpm over that at 3,000 rpm is clearly visible, and is consistent with the data shown in Fig. 6.

To accurately quantify the dependence between the bead temperature and the rotational speed, separate flames were produced, each with a different equivalence ratio. The thermocouple was rotated at a range of rotational speeds between 0 and 10,000 rpm and allowed to come to steady state at each speed. The data was then averaged over 10 seconds and is shown in Fig. 8 along with a curve-fit of the data. The fluctuation in temperature at each speed was minimal, on the order of 1 °C. The effect of the fluctuation in temperature, along with other potential uncertainties, such as errors in the thermocouple calibration, are included in the error bars.

The gas temperature can be accurately estimated from stationary thermocouple measurements for this particular burner because the burner mass flow rate is known and the flow rate exiting the burner is nearly uniform, allowing for an accurate prediction of gas velocity. This was done to obtain a gas temperature with which to compare to the curve-fitted gas temperature. In Fig. 8, this temperature is shown as the horizontal green line.

To obtain the gas temperatures from the curves, no assumptions were needed as to the thermocouple shape and geometry. Instead, the data was fitted to the general form for the Nusselt number given in Eq. 4, and yielded the following values for the fitting constants: $C = 0.6$, $m = n = 0.5$, $Pr = 0.69$ which match up well with values reported in the literature. The quality of the fit is illustrated by r^2 values of 0.99, 0.99 and 0.95 respectively for the three data sets.

For the rotating thermocouples the relative velocity of the gas over the thermocouple bead was obtained from rotational speed, neglecting the actual gas velocity since it was small compared to the velocity of the bead. The total relative velocity between the gas and the bead is therefore the magnitude of the vector sum of the gas velocity and that of the rotating thermocouple. As expected, the gas velocity plays a much more important role at lower rotational speeds (<3000 rpm). Conduction losses are negligible here because of the high aspect-ratio of the thermocouple wire. The gas temperature obtained from curve-fitting the data, $T_{g,RTC}$ is in excellent agreement with the value of T_g estimated from the radiation correction for a stationary thermocouple. These results are summarized in Table 1.

5. Discussion

Validity of Technique

The results shown in Figs. 6 and 7 display the dynamics of the technique. Increased rotational speed yields an increased bead temperature due to increased convection. Increasing convection to reduce the radiation correction is much like what is done in a suction pyrometer. However, if the technique simply relied on high convection, then the accuracy would be severely limited, as even at rotational speeds as high as 10,000 rpm the corrections were still on the order of 150 °C.

As can be seen from the form of the curves in Fig. 4, the benefit of high speed diminish with increased speeds, which is a frequent problem with suction pyrometers. Additionally, the losses to spatial resolution and the effects of flow-perturbation make high-speed operation restrictive for suction pyrometers.

More saliently, the high-speed rotation controls and defines the local velocity, and therefore the local convective heat transfer coefficient can be accurately predicted. The minimal number of assumptions that are required to yield excellent curve fits suggests the ability to accurately predict gas temperature with low uncertainty. The value of gas temperature predicted by the data is within 17 °C of T_g. Additionally, the values of the fitting parameters correspond very well to values reported in the literature, and this serves as further validation of the fitting technique. It is highly likely that the curve-fitted value is, in fact, more accurate than T_g since T_g was obtained from a radiation correction that required an assumption about bead shape and the functional form of the Nusselt number correlation. Moreover, this accuracy is virtually impossible to attain with a suction pyrometer because the flow rates do not approach infinity, the gas sample volume is large and the measurement times are long.

Spatial Resolution

The improvement in spatial resolution of the RTC over the suction pyrometer represents a significant advantage of the technique. Furthermore, to increase accuracy with the RTC technique the rotating speed can be increased, but the circumference over which the RTC averages the temperature (*i.e.,* the spatial resolution) remains the same. This means that there is no tradeoff between accuracy and spatial resolution in the RTC. This is not the case with the

suction pyrometer: the accuracy of the measurement is dependent on the amount of gas aspired

into the suction pyrometer and the spatial resolution of a suction pyrometer reduces as the flow

rate at which gas is aspirated increases. Fig. 9 shows the sampling of gas by a suction

pyrometer. In any system of practical interest, the gas will have some velocity given by V_{gas}. The

suction pyrometer accelerates that gas to the desired aspiration velocity, given by V_{sp}.

The area of gas sampled is therefore related to the ratio of velocities, V_{SP} and V_{gas}, where V_{SP} is

the aspiration velocity of the suction pyrometer, V_{gas} is the velocity of the gas being sampled,

$A_{sampled}$ is the effective region of gas sampled by the suction pyrometer and A_{SP} is the area of

the suction pyrometer's inlet. Typical free stream gas velocities are on the order of 1 m/s, and

suction pyrometer velocities , as discussed, can be as high as 200 m/s. The spatial resolution of

the suction pyrometer, therefore, is system dependent in that it is heavily dependent on the flow

rate of the gas being sampled. However, since aspiration velocities are typically an order of

magnitude greater than the velocities of the gases being sampled, the sacrifice in spatial

resolution is significant.

Averaging over Space and Time

The RTC measure an average temperature in space and time. Fig. 10a shows the circle traced out

by an RTC with a rotational radius 'r', rotating at a speed ω in a temperature field. The

instantaneous temperature of the bead is shown in Fig. 10b. If the RTC were allowed to reach

steady state at each point θ along the circle, then it would measure a temperature distribution $T_{b,\theta}$,

based on the varying temperature field as θ varies from 0 to 2π. This is represented by the solid

curve $T_b(\theta,\omega_0)$ in Fig. 10b. If ω was any positive nonzero value, then the RTC would not be able

153

to reach steady-state at each point along the circle, resulting in a flattening of the curve $T_b(\theta,\omega_0)$, and a temperature lag that are due to the thermal mass of the thermocouple. The magnitudes of both of are dictated by the time constant of the RTC, τ_b. As ω is increased, $T_{b,\theta}$, will further flatten out, as shown in Fig. 10b by curves $T_b(\theta,\omega_1)$ and $T_b(\theta,\omega_2)$.

Table 2 shows the relative magnitude of the RTC time constant, τ_b, and the time taken to traverse the circle at two rotational speeds of interest, for a range of bead diameters. It is apparent that at both rotational speeds, 5,000 rpm and 10,000 rpm, τ_b is much longer than the time taken to traverse the circle once, and is therefore insensitive to changes in the temperature over the circle. The RTC therefore measures a single mean temperature, $T_{b,m}$, while rotating around a point as it traverses the circumference, at sufficiently high rotational speeds.

If the temperature field that the RTC is spinning in experiences a change on a time scale that is significantly longer than τ_b, then it can completely capture this change, as a normal non-rotational thermocouple would. Similarly, if the temperature field changes on a time scale that is significantly shorter than τ_b, then the RTC would not be able to capture these changes. If the change were on the order of the time-constant of the thermocouple, then the rotation would average the measurement in both space and time.

Deconvolution to improve spatial resolution

We have shown that the RTC measures a constant, averaged temperature $T_{b,m}$ for practical rotational speeds and RTC time constants. For a measurement at a single location, the spatial

154

resolution of the RTC measurement is dictated by the circumference that is swept by the RTC. However, when the RTC is traversed across a temperature field the information obtained is the convolved temperature field. Deconvolution of this field can then yield an increased spatial accuracy.

Below we construct a methodology by which the RTC measurements in a temperature field can be deconvolved to yield spatial resolution approaching that of the diameter of the thermocouple wire. Let $f(x_1,y_1)$ be the temperature at a point (x_1,y_1) on the two-dimensional plane under investigation, $h(x_1,y_1)$ be the impulse function of the RTC measurement system, and $g(x_1,y_1)$ be the measurement obtained from a thermocouple when it rotates along a circle whose center is (x_1,y_1). These are illustrated in Fig.11.

From convolution theory

$$g = f*h \qquad (9)$$

where $*$ indicates the convolution operation. To simplify the calculation, f, g, and h are discretized into block grids. By doing so, the coordinates (x, y) are no longer made of real numbers indicating the exact location. Instead, they are made of integers indicating the indices of a certain block in the grid. Also, the integral involved in the RTC measurement system is simplified to a sum, and thus the impulse function h is significantly simplified to a two-dimensional grid with blocks being $\frac{1}{N}$ if crossed by the circumference and 0 otherwise, where N is the total number of blocks crossed by the circumference. Such a discretized impulse function is equivalent to a filter or mask in digital image processing, and corresponding deconvolution algorithms can be found in Ref [97].

Fig. 12. shows the results of the deconvolution simulation. In Fig. 11a, a temperature distribution is assumed between 20˚C and 1000˚C over a 2-Dimensional plane that is 100 mm × 100 mm. The plane is then discretized with each grid square measuring 1mm × 1mm. An RTC with rotational radius 10 mm is then swept across the plane in both the x- and y- directions, with each new RTC measurement centered at the next grid point. This "measured" distribution, $g(x,y)$ is shown in Fig. 12b. The deconvolution operation is then applied to the measured distribution in Fig 12b. to yield a deconvolved distribution, shown in Fig. 12c.

The deconvolved distribution is in excellent agreement with the original distribution. The RMS error of the deconvolved distribution is 0.37˚C, while the RMS error of the measured distribution is 24˚C. The distribution of this error for the deconvolved distribution is shown in Fig. 12d.

Required modifications for use in industrial systems

This work represents a proof-of-concept for the RTC technique; however, in order to be viable for use in for industrial-scale, particle-laden flows, a number of design modifications are required. The experimental probe used was 165 mm long, but in order to get a complete temperature profile in larger systems, a probe as long as the inner diameter of the combustion chamber would be required. Additionally, a cooling jacket would be required to protect the probe from the heat of the furnace or combustion chamber.

Finally, in order to protect the RTC from excessive particles, a shield would be required. The shield would rotate along with the RTC, but in front of it, as shown in Fig 13. The shield would have a small enough characteristic length so as not to alter the flow around the RTC, while creating a particle-free zone in its wake so as to protect the RTC.

6. Conclusions

In this work, the challenges associated with accurate temperature measurement using thermocouples in large, radiating flame environments are summarized, along with the limitations of techniques currently in use. A method employing a Rotating Thermocouple (RTC) is presented that seeks to alleviate many of the inaccuracies that currently limit temperature measurement. An experimental system has been constructed to tests the ability of a RTC to make accurate flame temperature measurements. The results show a significant reduction in the required value of the radiation correction, while the curve fit yields a temperature value that is within 15 °C of the calculated value using radiative correction. A deconvolution methodology has also been introduced, which could improve the spatial resolution to the level of the stationary thermocouple. Table 4 compares and contrasts the various approaches to thermocouple measurement: fine wire thermocouple, suction pyrometer and rotating thermocouple.

Acknowledgments
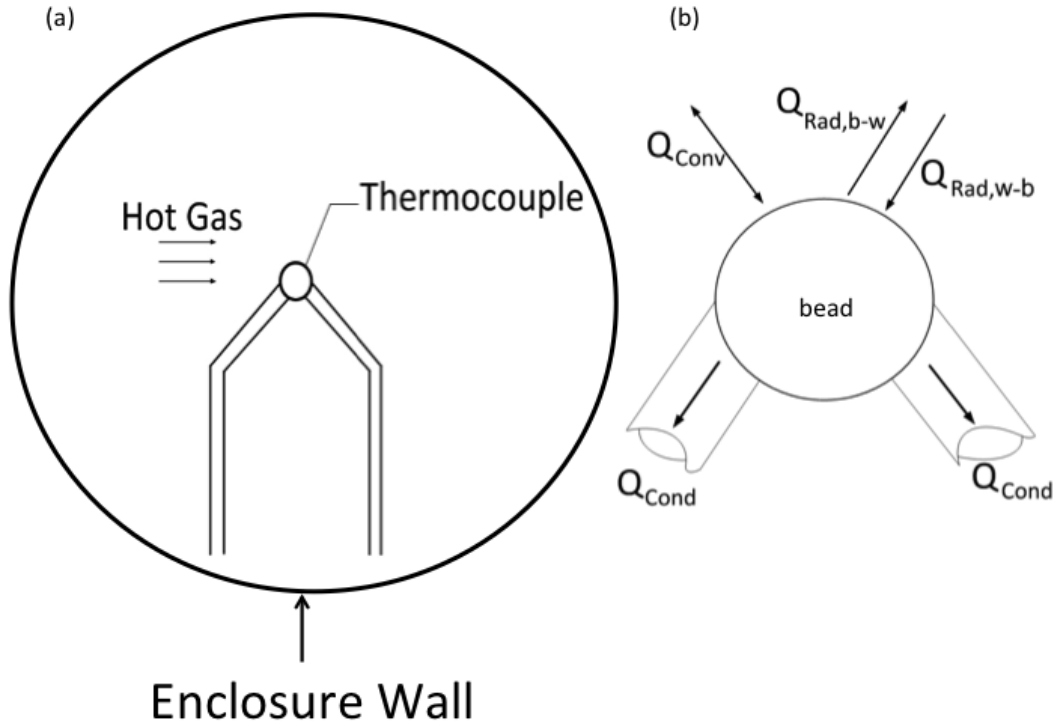
FIGURES

Figure 1: Schematic illustrating heat transfer to and from thermocouple bead: (a) Thermocouple in a stream of hot gas; (b) Control volume of thermocouple
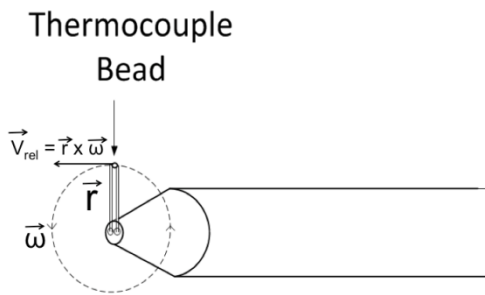
Figure 2. Schematic illustrating the quantities Vrel, ω and r
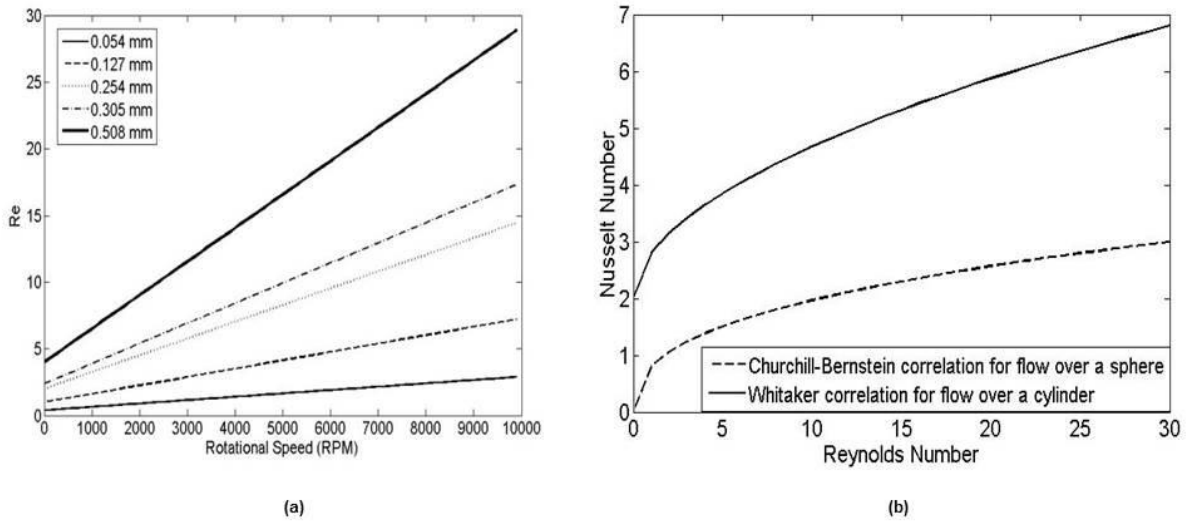
Figure 3. (a) The Reynolds number as a function of rotational speed for different thermocouple diameters, (b) The Nusselt number as a function of Reynolds number for spherical and cylindrical bead geometries as determined from various correlations.
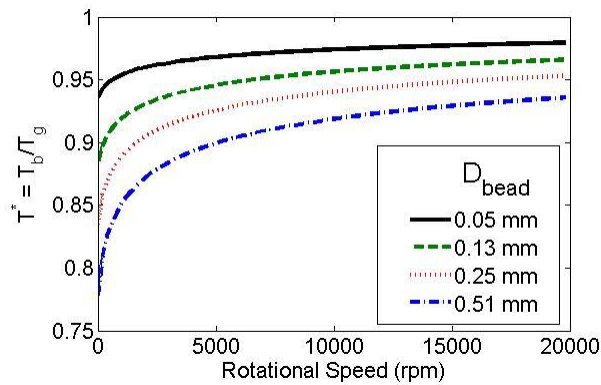
Figure. 4: The normalized temperature, which is the ratio of the thermocouple bead temperature, T_b, to the true gas temperature, T_g, (in °C) plotted as a function of rotational speed.
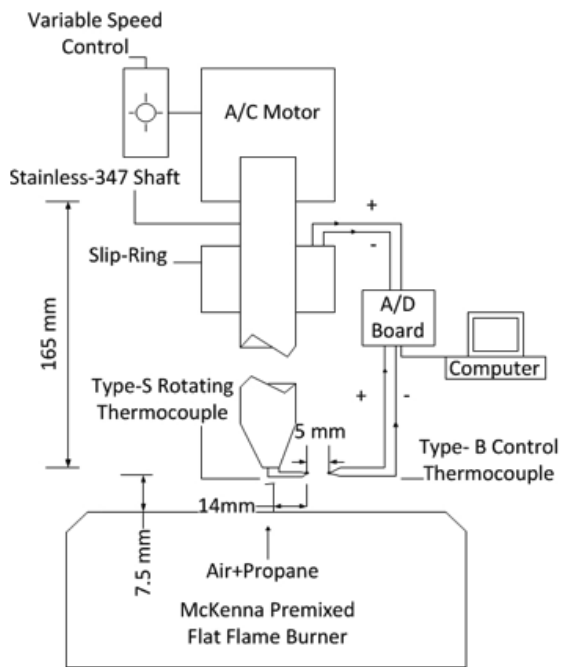
Figure 5. Schematic of experimental setup.
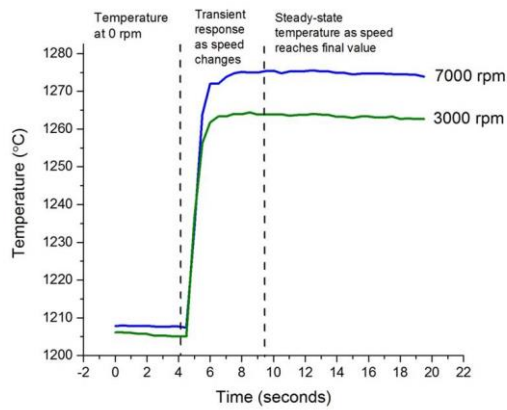
Figure 6. Dynamics of RTC: Experimental data showing transient temperature measured by RTC during the changing of rotational speed, demarcated into transient zone and steady-state zones for two different rotational speeds: 3000 rpm and 7000 rpm.
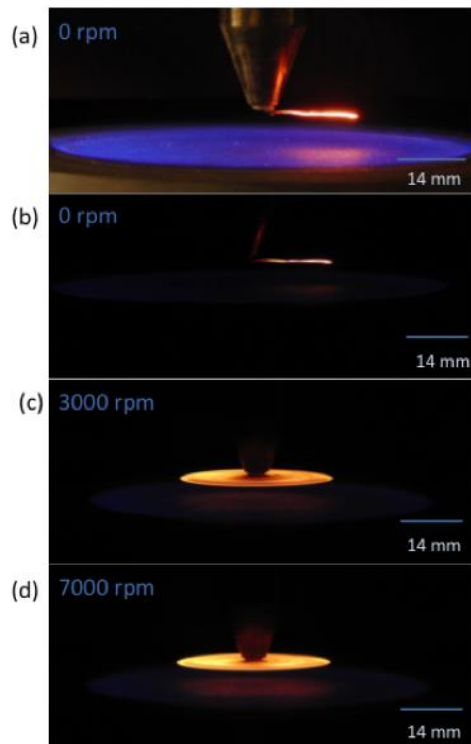
Figure. 7. Images of (a) the RTC assembly and the McKenna flat-flame burner, and the thermocouple at (b) 0 rpm, (c) 3000 rpm and (d) 7000 rpm. The camera settings for aperture and shutter speed were constant in Figs. 7b-d.
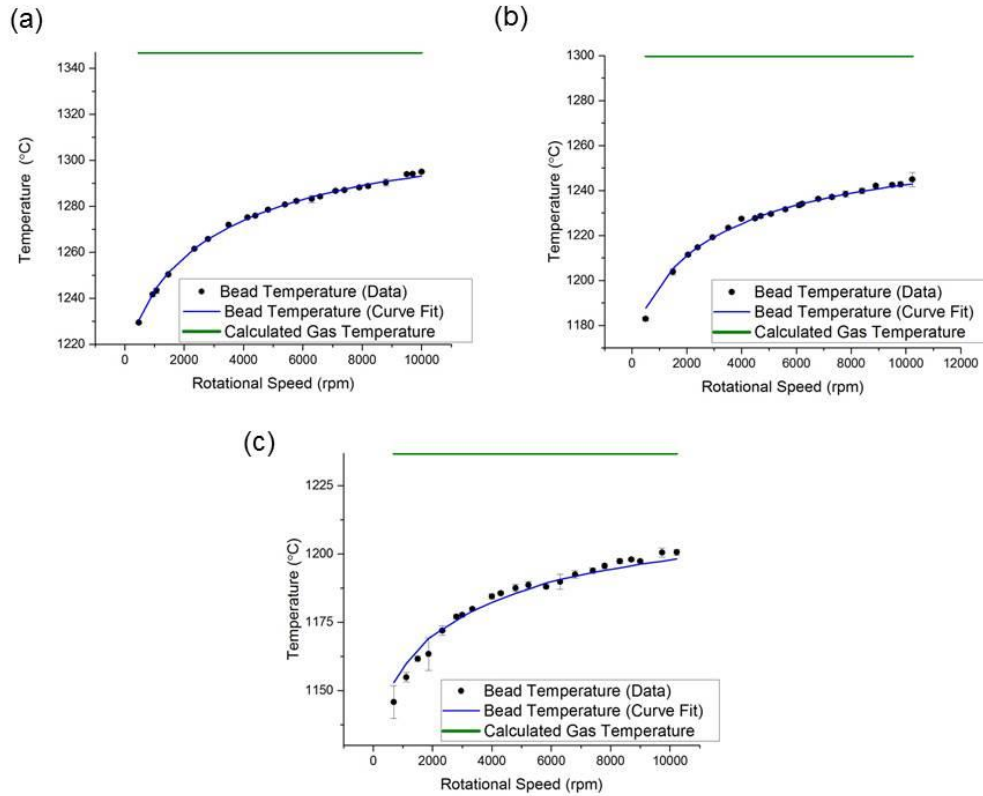
Figure. 8. Relationship between temperature and rotating speed for RTC: Experimental temperatures measured by RTC plotted against rotational speed for a) φ=1.0, b) φ= 0.85 and c) φ = 0.70. The radiation-corrected gas temperature is presented with the horizontal dotted line, and the curve fit predicted by the theory is included for each
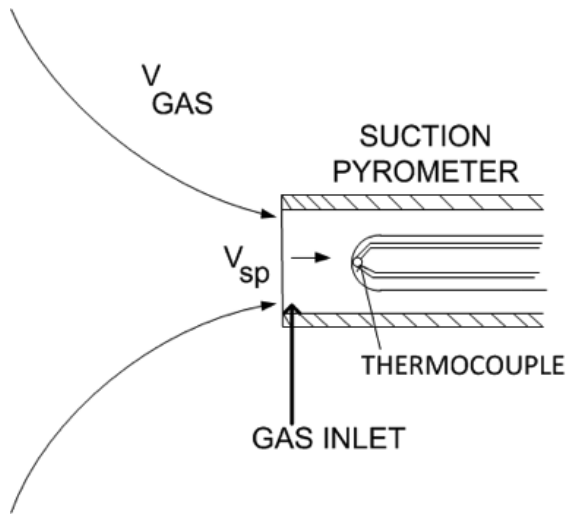
Figure. 9. Schematic illustrating high sampling area of suction pyrometer.
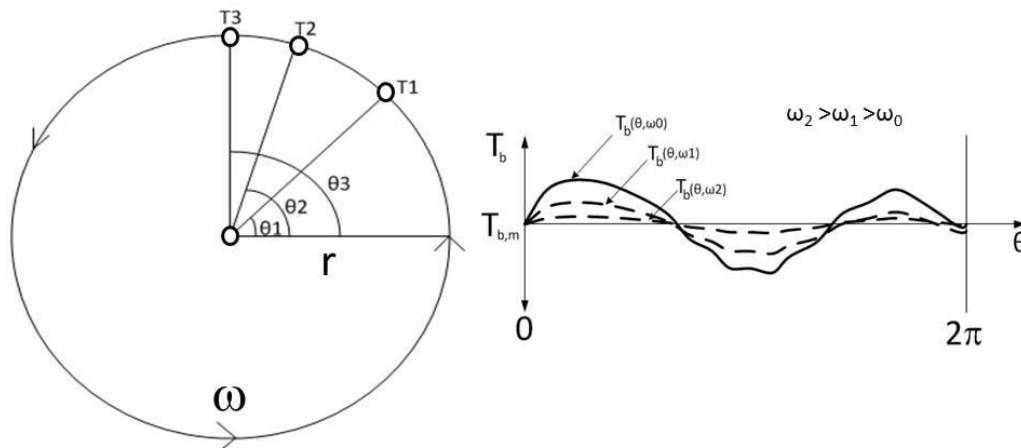
Figure. 10. Averaging over circumference. (a) RTC rotating with a radius r and a rotational speed ω in a temperature field, (b) shows the instantaneous temperature measured by the RTC in the temperature field at different rotational speeds.
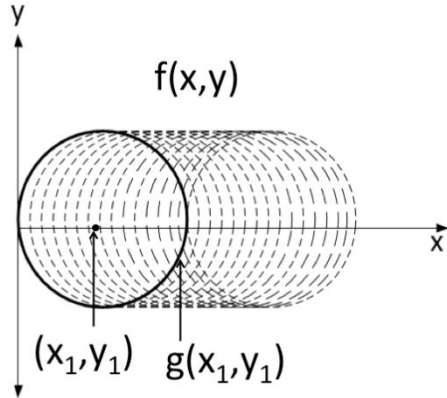
Figure 11. Schematic of deconvolution operation.
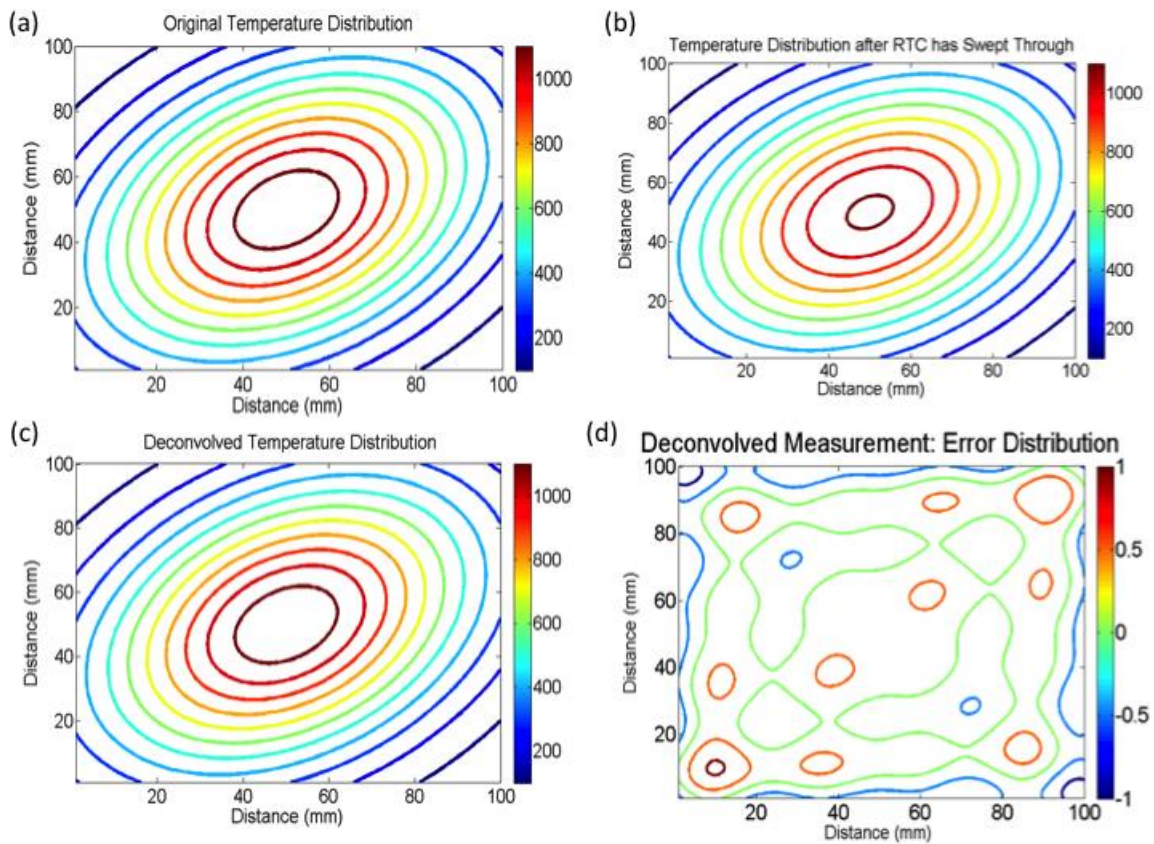
Figure 12. Results of deconvolution simulation. (a) Original temperature distribution, (b) measured temperature   distribution after RTC as swept through, (c) Deconvolved temperature distribution, (d) distribution of error after deconvolution operation.
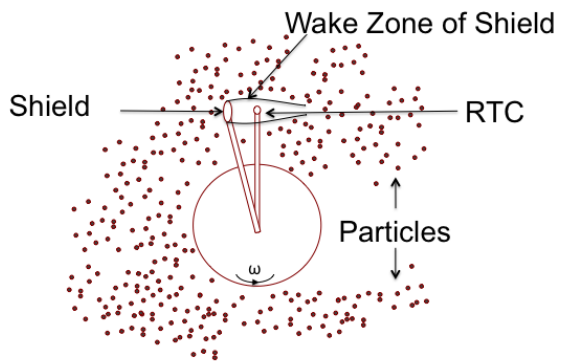
Figure 13. Front view of RTC illustrating future concept for shield protect RTC from particles.

TABLES

Table 1: Radiation-corrected gas temperatures and gas temperatures predicted with RTC

Φ	Tg	Tg,RTC
	Calculated from radiation correction (°C)	Yielded by curve-fit (°C)
1.0	1347	1340
0.85	1301	1284
0.70	1234	1235

Table 2. Calculated Relative magnitude of RTC time constant and rotational speed

Bead Diameter (mm)	Time Constant, τ_b at 5,000 rpm (seconds)	Number of circles swept in one time constant at 5,000 rpm	Time constant, τ_b, at 10,000 rpm (seconds)	Number of circles swept in one time constant at 10,000 rpm
0.30	0.46	38	0.36	60
0.20	0.24	20	0.19	32
0.13	0.11	9	0.09	15

Table 4: Summary of advantages and disadvantages of various thermocouple measurements of flame temperature

	Fine-Wire Thermocouple	Suction Pyrometer	High-Speed Rotational Thermocouple (RTC)
Accuracy	**High** Fine-wire minimizes radiation losses, though they may still be present.	**Moderate** Inaccuracies of hundreds of degrees Celsius can persist even with high-speed aspiration.	**Very high** Can fit data to theory to get true gas temperature.
Spatial Resolution	**Very high** Limit of resolution is surface area of fine-wire thermocouple, on the order of $10^{-9}m^2$.	**Poor** Can be on the order of $1m^2$; significant tradeoff between increased accuracy and spatial resolution.	**High** Can deconvolve measurements to achieve spatial resolution approaching that of stationary thermocouple. No tradeoff between accuracy and spatial resolution.
Temporal Resolution	**Extremely high** Owing to small mass of thermocouple; Time constant on the order of 50-100ms.	**Very poor** Due to presence of shields; Time constant on the order of minutes.	**High** Time constant is higher than that of a fine wire thermocouple, but RTC also averages over space and time, so temporal resolution is not as high as that of fine-wire thermocouple.

Mechanical Integrity	Very poor	Very high	Moderate to high
	Extremely fragile.	Due to presence of shields.	Thermocouple wire diameter is larger than that of a fine-wire thermocouple, and can be shielded, but not completely enclosed like suction pyrometer.
Time to Take Measurement	Very low	Very high	Very low
		Due to presence of shield.	
Maintenance	Very High	Very High	Anticipated to be low
	Fragility causes frequent breakage, particularly in particle-laden flows.	Due to clogging	

REFERENCES

[1] U.S.E.I. Administration, Annual Energy Review, 2012.

[2] S. Turns, An introduction to combustion : concepts and applications, WCB/McGraw-Hill2000.

[3] C.K. Law, Combustion physics, Cambridge University Press2006.

[4] R.W. Bilger, REACTION-RATES IN DIFFUSION FLAMES, Combustion and Flame 30 (1977) 277-284.

[5] R.S. Barlow, J.H. Frank, A.N. Karpetis, J.Y. Chen, Piloted methane/air jet flames: Transport effects and aspects of scalar structure, Combustion and Flame 143 (2005) 433-449.

[6] R.W. Bilger, S.H. Stårner, R.J. Kee, On reduced mechanisms for methane air combustion in nonpremixed flames, Combustion and Flame 80 (1990) 135-149.

[7] J.C. Biordi, C.P. Lazzara, J.F. Papp, Flame Structure Studies of Cf3br-Inhibited Methane Flames .3. Effect of 1-Percent Cf3br on Composition, Rate Constants, and Net Reaction-Rates, J Phys Chem-Us 81 (1977) 1139-1145.

[8] J.D. Bittner, A molecular beam mass spectrometer study of fuel-rich and sooting benzene-oxygen flames, Massachusetts Institute of Technology, 1981, pp. 3 v. (960 i.e. 961 leaves).

[9] R.J. Cattolica, OH radical nonequilibrium in methane air flat flames, Combustion and Flame 44 (1982) 43-59.

[10] R.E. Teets, J.H. Bechtel, Sensitivity analysis of a model for the radical recombination region of hydrocarbon-air flames, Symposium (International) on Combustion 18 (1981) 425-432.

[11] J.R. Bulau, W.E. Kaskan, Radical Overshoots and Dissociation in Methane-Air Flames, J Chem Phys 62 (1975) 3605-3608.

[12] S.R. Smith, A.S. Gordon, Studies Of Diffusion Flames. I. The Methane Diffusion Flame, The Journal of Physical Chemistry 60 (1956) 759-763.

[13] R.E. Mitchell, A.F. Sarofim, L.A. Clomburg, PARTIAL EQUILIBRIUM IN THE REACTION ZONE OF METHANE-AIR DIFFUSION FLAMES, Combustion and Flame 37 (1980) 201-206.

[14] R.E. Mitchell, A.F. Sarofim, L.A. Clomburg, EXPERIMENTAL AND NUMERICAL INVESTIGATION OF CONFINED LAMINAR DIFFUSION FLAMES, Combustion and Flame 37 (1980) 227-244.

[15] K.C. Smyth, J.H. Miller, R.C. Dorfman, W.G. Mallard, R.J. Santoro, Soot Inception in a Methane Air Diffusion Flame as Characterized by Detailed Species Profiles, Combustion and Flame 62 (1985) 157-181.

[16] K.C. Smyth, P.J.H. Tjossem, A. Hamins, J.H. Miller, Concentration measurements of OH· and equilibrium analysis in a laminar methane-air diffusion flame, Combustion and Flame 79 (1990) 366-380.

[17] J. Warnatz, STRUCTURE OF FREELY PROPAGATING AND BURNER-STABILIZED FLAMES IN THE H2-CO-O2 SYSTEM, Ber. Bunsen-Ges. Phys. Chem. Chem. Phys. 83 (1979) 950-957.

[18] M.C. Drake, R.J. Blint, STRUCTURE OF LAMINAR OPPOSED-FLOW DIFFUSION FLAMES WITH CO/H-2/N-2 FUEL, Combust. Sci. Technol. 61 (1988) 187-224.

[19] K.C. Smyth, P.J.H. Tjossem, RADICAL CONCENTRATION MEASUREMENTS IN HYDROCARBON DIFFUSION FLAMES, Applied Physics B-Photophysics and Laser Chemistry 50 (1990) 499-511.

[20] K.C. Smyth, P.J.H. Tjossem, A. Hamins, J.H. Miller, CONCENTRATION MEASUREMENTS OF OH. AND EQUILIBRIUM-ANALYSIS IN A LAMINAR METHANE AIR DIFFUSION FLAME, Combust. Flame 79 (1990) 366-380.
[21] S.H. Chung, F.A. Williams, ASYMPTOTIC STRUCTURE AND EXTINCTION OF CO-H2 DIFFUSION FLAMES WITH REDUCED KINETIC MECHANISMS, Combust. Flame 82 (1990) 389-410.
[22] R.S. Barlow, G.J. Fiechtner, C.D. Carter, J.Y. Chen, Experiments on the scalar structure of turbulent CO/H2N2 jet flames, Combustion and Flame 120 (2000) 549-569.
[23] H.Y. Shih, J.R. Hsu, A computational study of combustion and extinction of opposed-jet syngas diffusion flames, Int. J. Hydrog. Energy 36 (2011) 15868-15879.
[24] R.S. Barlow, Unexpected Effects Of Preferential Transport In Turbulent Premixed Flames, JOINT MEETING- US SECTIONS OF THE COMBUSTION INSTITUTE 2 (2011).
[25] R.S. Barlow, R.W. Dibble, J.Y. Chen, R.P. Lucht, Effect of Damköhler number on superequilibrium OH concentration in turbulent nonpremixed jet flames, Combustion and Flame 82 (1990) 235-251.
[26] R.S. Barlow, A.N. Karpetis, J.H. Frank, J.Y. Chen, Scalar profiles and NO formation in laminar opposed-flow partially premixed methane/air flames, Combustion and Flame 127 (2001) 2102-2118.
[27] A.N. Karpetis, R.S. Barlow, Measurements of scalar dissipation in a turbulent piloted methane/air jet flame, Proceedings of the Combustion Institute 29 (2002) 1929-1936.
[28] F. Fuest, G. Magnotti, R.S. Barlow, J.A. Sutton, Scalar structure of turbulent partially-premixed dimethyl ether/air jet flames, Proceedings of the Combustion Institute 35 (2015) 1235-1242.
[29] F. Fuest, R.S. Barlow, G. Magnotti, A. Dreizler, I.W. Ekoto, J.A. Sutton, Quantitative acetylene measurements in laminar and turbulent flames using 1D Raman/Rayleigh scattering, Combustion and Flame 162 (2015) 2248-2255.
[30] V. Narayanaswamy, R. Burns, N.T. Clemens, Kr-PLIF for scalar imaging in supersonic flows, Optics Letters 36 (2011) 4185-4187.
[31] A.G. Hsu, V. Narayanaswamy, N.T. Clemens, J.H. Frank, Mixture fraction imaging in turbulent non-premixed flames with two-photon LIF of krypton, Proceedings of the Combustion Institute 33 (2011) 759-766.
[32] R.L. Axelbaum, C.K. Law, W.L. Flower, Preferential diffusion and concentration modification in sooting counterflow diffusion flames, Symposium (International) on Combustion 22 (1989) 379-386.
[33] A. Michalakou, P. Stavropoulos, S. Couris, Laser-induced breakdown spectroscopy in reactive flows of hydrocarbon-air mixtures, Applied Physics Letters 92 (2008).
[34] K. Johannes, L. Zhongshan, A. Marcus, Laser-induced breakdown spectroscopy in a partially premixed turbulent jet flame, Measurement Science and Technology 24 (2013) 075205.
[35] S. Joshi, D.B. Olsen, C. Dumitrescu, P.V. Puzinauskas, A.P. Yalin, Laser-Induced Breakdown Spectroscopy for In-Cylinder Equivalence Ratio Measurements in Laser-Ignited Natural Gas Engines, Appl. Spectrosc. 63 (2009) 549-554.
[36] J. Kiefer, J.W. Tröger, Z.S. Li, M. Aldén, Laser-induced plasma in methane and dimethyl ether for flame ignition and combustion diagnostics, Applied Physics B 103 (2011) 229-236.
[37] J. Kiefer, J.W. Tröger, T. Seeger, A. Leipertz, B. Li, Z.S. Li, M. Aldén, Laser-induced breakdown spectroscopy in gases using ungated detection in combination with polarization

filtering and online background correction, Measurement Science and Technology 21 (2010) 065303.

[38] M.S. Mansour, H. Imam, K.A. Elsayed, W. Abbass, Local equivalence ratio measurements in turbulent partially premixed flames using laser-induced breakdown spectroscopy, Spectrochimica Acta Part B: Atomic Spectroscopy 64 (2009) 1079-1084.

[39] V. Sturm, R. Noll, Laser-Induced Breakdown Spectroscopy of Gas Mixtures of Air, CO2, N2, and C3H8 for Simultaneous C, H, O, and N Measurement, Applied Optics 42 (2003) 6221-6225.

[40] S. Zhang, X. Yu, F. Li, G. Kang, L. Chen, X. Zhang, Laser induced breakdown spectroscopy for local equivalence ratio measurement of kerosene/air mixture at elevated pressure, Optics and Lasers in Engineering 50 (2012) 877-882.

[41] M.M. Tripathi, K.K. Srinivasan, S.R. Krishnan, F.Y. Yueh, J.P. Singh, A comparison of multivariate LIBS and chemiluminescence-based local equivalence ratio measurements in premixed atmospheric methane-air flames, Fuel 106 (2013) 318-326.

[42] F. Ferioli, S.G. Buckley, Measurements of hydrocarbons using laser-induced breakdown spectroscopy, Combustion and Flame 144 (2006) 435-447.

[43] F. Ferioli, P.V. Puzinauskas, S.G. Buckley, Laser-induced breakdown spectroscopy for on-line engine equivalence ratio measurements, Applied Spectroscopy 57 (2003) 1183-1189.

[44] T.X. Phuoc, Laser-induced spark for simultaneous ignition and fuel-to-air ratio measurements, Optics and Lasers in Engineering 44 (2006) 520-534.

[45] T.X. Phuoc, F.P. White, Laser-induced spark for measurements of the fuel-to-air ratio of a combustible mixture, Fuel 81 (2002) 1761-1765.

[46] P. Stavropoulos, A. Michalakou, G. Skevis, S. Couris, Quantitative local equivalence ratio determination in laminar premixed methane-air flames by laser induced breakdown spectroscopy (LIBS), Chemical Physics Letters 404 (2005) 309-314.

[47] A.E. Majd, A.S. Arabanian, R. Massudi, M. Nazeri, Spatially Resolved Laser-Induced Breakdown Spectroscopy in Methane?Air Diffusion Flames, Applied Spectroscopy 65 (2011) 36-42.

[48] M. Kotzagianni, S. Couris, Femtosecond laser induced breakdown spectroscopy of air-methane mixtures, Chemical Physics Letters 561 (2013) 36-41.

[49] M. Mansour, H. Imam, K.A. Elsayed, A.M. Elbaz, W. Abbass, Quantitative mixture fraction measurements in combustion system via laser induced breakdown spectroscopy, Optics and Laser Technology 65 (2015) 43-49.

[50] D.X. Du, R.L. Axelbaum, C.K. Law, SOOT FORMATION IN STRAINED DIFFUSION FLAMES WITH GASEOUS ADDITIVES, Combustion and Flame 102 (1995) 11-20.

[51] S. Krishnan, B.M. Kumfer, W.D. Wu, J.C. Li, A. Nehorai, R.L. Axelbaum, An Approach to Thermocouple Measurements That Reduces Uncertainties in High-Temperature Environments, Energy & Fuels 29 (2015) 3446-3455.

[52] P.R.N. Childs, J.R. Greenwood, C.A. Long, Review of temperature measurement, Rev. Sci. Instrum. 71 (2000) 2959-2978.

[53] I.C.E. Turcu, M.C. Gower, P. Huntington, Measurement of KrF laser breakdown threshold in gases, Optics Communications 134 (1997) 66-68.

[54] J. Kiefer, J.W. Troger, Z.S. Li, T. Seeger, M. Alden, A. Leipertz, Laser-induced breakdown flame thermometry, Combustion and Flame 159 (2012) 3576-3582.

[55] A. Hrdlicka, L. Zaoralkova, M. Galiova, T. Ctvrtnickova, V. Kanicky, V. Otruba, K. Novotny, P. Krasensky, J. Kaiser, R. Malina, K. Palenikova, Correlation of acoustic and optical

emission signals produced at 1064 and 532 nm laser-induced breakdown spectroscopy (LIBS) of glazed wall tiles, Spectrochimica Acta Part B-Atomic Spectroscopy 64 (2009) 74-78.

[56] G.Y. Chen, E.S. Yeung, ACOUSTIC-SIGNAL AS AN INTERNAL STANDARD FOR QUANTITATION IN LASER-GENERATED PLUMES, Analytical Chemistry 60 (1988) 2258-2263.

[57] C. Chaleard, P. Mauchien, N. Andre, J. Uebbing, J.L. Lacour, C. Geertsen, Correction of matrix effects in quantitative elemental analysis with laser ablation optical emission spectrometry, Journal of Analytical Atomic Spectrometry 12 (1997) 183-188.

[58] M. Oksanen, J. Hietanen, PHOTOACOUSTIC BREAKDOWN SOUND SOURCE IN AIR, Ultrasonics 32 (1994) 327-331.

[59] Q. Qin, K. Attenborough, Characteristics and application of laser-generated acoustic shock waves in air, Applied Acoustics 65 (2004) 325-340.

[60] N. Hosoya, M. Nagata, I. Kajiwara, Acoustic testing in a very small space based on a point sound source generated by laser-induced breakdown: Stabilization of plasma formation, Journal of Sound and Vibration 332 (2013) 4572-4583.

[61] N. Hosoya, M. Nagata, I. Kajiwara, R. Umino, Nano-second Laser-induced Plasma Shock Wave in Air for Non-contact Vibration Tests, Experimental Mechanics 56 (2016) 1305-1311.

[62] D.A. Hutchins, Mechanisms of pulsed photoacoustic generation, Canadian Journal of Physics 64 (1986) 1247-1264.

[63] C. DeMichelis, Laser interaction with solids - A bibliographical review, IEEE Journal of Quantum Electronics 6 (1970) 630-641.

[64] S. Maurice, R.C. Wiens, M. Saccoccio, B. Barraclough, O. Gasnault, O. Forni, N. Mangold, D. Baratoux, S. Bender, G. Berger, J. Bernardin, M. Berthe, N. Bridges, D. Blaney, M. Bouye, P. Cais, B. Clark, S. Clegg, A. Cousin, D. Cremers, A. Cros, L. DeFlores, C. Derycke, B. Dingler, G. Dromart, B. Dubois, M. Dupieux, E. Durand, L. d'Uston, C. Fabre, B. Faure, A. Gaboriaud, T. Gharsa, K. Herkenhoff, E. Kan, L. Kirkland, D. Kouach, J.L. Lacour, Y. Langevin, J. Lasue, S. Le Mouelic, M. Lescure, E. Lewin, D. Limonadi, G. Manhes, P. Mauchien, C. McKay, P.Y. Meslin, Y. Michel, E. Miller, H.E. Newsom, G. Orttner, A. Paillet, L. Pares, Y. Parot, R. Perez, P. Pinet, F. Poitrasson, B. Quertier, B. Salle, C. Sotin, V. Sautter, H. Seran, J.J. Simmonds, J.B. Sirven, R. Stiglich, N. Striebig, J.J. Thocaven, M.J. Toplis, D. Vaniman, The ChemCam Instrument Suite on the Mars Science Laboratory (MSL) Rover: Science Objectives and Mast Unit Description, Space Science Reviews 170 (2012) 95-166.

[65] R.C. Wiens, S. Maurice, B. Barraclough, M. Saccoccio, W.C. Barkley, J.F. Bell, S. Bender, J. Bernardin, D. Blaney, J. Blank, M. Bouye, N. Bridges, N. Bultman, P. Cais, R.C. Clanton, B. Clark, S. Clegg, A. Cousin, D. Cremers, A. Cros, L. DeFlores, D. Delapp, R. Dingler, C. D'Uston, M.D. Dyar, T. Elliott, D. Enemark, C. Fabre, M. Flores, O. Forni, O. Gasnault, T. Hale, C. Hays, K. Herkenhoff, E. Kan, L. Kirkland, D. Kouach, D. Landis, Y. Langevin, N. Lanza, F. LaRocca, J. Lasue, J. Latino, D. Limonadi, C. Lindensmith, C. Little, N. Mangold, G. Manhes, P. Mauchien, C. McKay, E. Miller, J. Mooney, R.V. Morris, L. Morrison, T. Nelson, H. Newsom, A. Ollila, M. Ott, L. Pares, R. Perez, F. Poitrasson, C. Provost, J.W. Reiter, T. Roberts, F. Romero, V. Sautter, S. Salazar, J.J. Simmonds, R. Stiglich, S. Storms, N. Striebig, J.J. Thocaven, T. Trujillo, M. Ulibarri, D. Vaniman, N. Warner, R. Waterbury, R. Whitaker, J. Witt, B. Wong-Swanson, The ChemCam Instrument Suite on the Mars Science Laboratory (MSL) Rover: Body Unit and Combined System Tests, Space Science Reviews 170 (2012) 167-227.

[66] J. Appel, H. Bockhorn, M. Frenklach, Kinetic modeling of soot formation with detailed chemistry and physics: Laminar premixed flames of C-2 hydrocarbons, Combustion and Flame 121 (2000) 122-136.
[67] H. Wang, M. Frenklach, A detailed kinetic modeling study of aromatics formation in laminar premixed acetylene and ethylene flames, Combustion and Flame 110 (1997) 173-221.
[68] R. Noll, Laser-Induced Breakdown Spectroscopy: Fundamentals and Applications, Springer2012.
[69] J.P. Singh, S.N. Thakur, Laser-Induced Breakdown Spectroscopy, Elsevier Science2007.
[70] A.P.M. Michel, A.D. Chave, Analysis of laser-induced breakdown spectroscopy spectra: The case for extreme value statistics, Spectrochimica Acta Part B-Atomic Spectroscopy 62 (2007) 1370-1378.
[71] F. Xia, R.L. Axelbaum, Simplifying the complexity of diffusion flames through interpretation in C/O ratio space, Computers & Mathematics with Applications 65 (2013) 1625-1632.
[72] F. Xia, G.S. Yablonsky, R.L. Axelbaum, Numerical study of flame structure and soot inception interpreted in carbon-to-oxygen atom ratio space, Proceedings of the Combustion Institute 34 (2013) 1085-1091.
[73] M.V. Heitor, Moreira, A.L.N, Thermocouples and sample probes for combustion studies, Energy Combustion Science 19 (1993) 259-278.
[74] H. Sato. A., K., Hasatani, M.., Sugaiyama, S., Kimura, J., , A correctional calculation method for thermocouple measurements of temperatures in flames, Combustion and Flame 24 (1975) 35-41.
[75] M.P.M. R. Viskanta, Radiation heat transfer in combustion systems, Progress in Energy and Combustion Science 13 (1987) 97-160.
[76] P.P.a.J.C.L. A Sbaibi, Frequency response of fine wires under simultaneous radiative-convective heat transfer, Journal of Physics E: Scientific Instruments 22 (1989).
[77] A.D. J C Lecordier, P Gajan and P Paranthoen, Correction of temperature fluctuation measurements using cold wires, Journal of Physics E: Scientific Instruments 17 (1984).
[78] H.A.M. F.C Lockwood, Fluctuating temperature measurements in turbulent jet diffusion flame, Combustion and Flame 47 (1982) 291-314.
[79] K.J.M. D. Bradley, Measurement of High Gas Temperatures with Fine Wire Thermocouples, Journal of Mechanical Engineering Science 10 (1968).
[80] W.M.P. L.G Blevins, Modeling of bare and aspirated thermocouples in compartment fires, Fire Safety Journal 33 (1999) 239-259.
[81] A.H. S.C Kim, On the Temperature Measurement Bias and Time Response of an Aspirated Thermocouple in Fire Environment, Journal of Fire Sciences 26 (2008).
[82] C.D. S. Brohez, G. Marlair, A two-thermocouples probe for radiation corrections of measured temperatures in compartment fires, Fire Safety Journal 39 (2004) 399-411.
[83] Y.O. M. Tagawa, Two-thermocouple probe for fluctuating temperature measurement in combustion—Rational estimation of mean and fluctuating time constants Combustion and Flame 109 (1997) 549-560.
[84] Y.M. M. Katuski, Yasushi Matsumoto, An improved thermocouple technique for measurement of fluctuating temperatures in flames, Combustion and Flame 67 (1987) 27-36.
[85] G.I. P.C Hung, R. Kee, S. McLoone, Difference equation approach to two-thermocouple sensor characterization in constant velocity flow environments, Review of Scientific Instruments 76 (2005).

[86] A.K.C.L. D. Bradley, M. Missaghi Response of Compensated Thermocouples to Fluctuating Temperatures: Computer Simulation, Experimental Results and Mathematical Modelling, Combustion Science and Technology 64 (1989).

[87] P.A.C. J.S Newman, Simple Aspirated Thermocouple for Use in Fires, Journal of Fire and Flammability 10 (1979) 326-336.

[88] H.F. A. Z'Graggen, A. Steinfeld, Gas temperature measurement in thermal radiating environments using a suction thermocouple apparatus, Measurement Science and Technology 18 (2007).

[89] E.B. W.M. Pitts, R.D Peacock, R.D Mitler, H.E Johnsson, E.L Reneke, L.G Blevins Temperature Uncertainties for Bare-Bead and Aspirated Thermocouple Measurements in Fire Environments NIST, West Conshohocken, Pennsylvania 2002.

[90] IFRF, in: IFRF (Ed.), Livorno, Italy, 2009.

[91] J.T. Nakos, Uncertainty Analysis of Thermocouple Measurements Used in Normal and Abnormal Thermal Environment Experiments Sandia's Radiant Heat Facility and Lurance Canyon Burn Site, Sandia National Laboratories Alburquerque, NM, 2004.

[92] S.W.C.a.M. Bernstein, A Correlating Equation for Forced Convection From Gases and Liquids to a Circular Cylinder in Crossflow, Journal of Heat Transfer 99 (1977) 300-306.

[93] D. Incropera, Bergman and Lavine, Fundamentals of Heat and Mass Transfer, John Wiley and Sons2007.

[94] A.L. G. Sutton, G. Edwards, D. Greenhalgh, A combustion temperature and species standard for the calibration of laser diagnostic techniques, Combustion and Flame 147 (2006) 39-48.

[95] A.D. M.A Gregor, A quasi-adiabatic laminar flat flame burner for high temperature calibration, Measurement Science and Technology 20 (2009).

[96] S.D.I. F. Migliorini, F. Cignoli, G. Zizak How "flat" is the rich premixed flame produced by your McKenna burner?, Combustion and Flame 153 (2008) 384-393.

[97] R.E.W. R.C Gonzalez, S.L Eddins, Digital Image Processing Using Matlab, Pearson Prentice Hall, Upper Saddle River, N.J 2004.